Imperial College of London
Department of Earth Science and Engineering

Numerical modelling of local scour with computational methods

Juan Mauricio Nunez Rattia

Submitted in part fulfilment of the requirements for the degree of:
Doctor of Philosophy in Computational Physics of the Imperial College
London and the Diploma of Imperial College London.
November 2018

Abstract

Evaluating bed morphological evolution (specifically the scoured bed level) accurately using computational modelling is critical for analyses of the stability of many marine and coastal structures, such as piers, groynes, breakwaters, submarine pipelines and even telecommunication cables.

This thesis considers the coupled hydrodynamic and morphodynamic modelling of the local scour around hydraulic structures, such as near a vertical pile or near a horizontal pipe. The focus in this study is on applying a fluid-structure interaction (FSI) approach to simulate the morphodynamical behaviour of the bed deformation, replacing the structural (i.e. solid mechanics) equation by the sediment continuity equation or Exner equation. Specifically, this works presents a novel method of mesh movement with anisotropic mesh adaptivity based on optimization for simulating local scour near structures with discontinuous Garlerkin (DG) discretisation methods for solving the flow field. Amongst the other goals of this work is the validation of the proposed procedure with previously performed laboratory as well as two- and three-dimensional numerical experiments.

Additionally, performance is considered using an implementation of the methodology within Fluidity (`http://fluidityproject.github.io/`), an open-source, multi-physics, computational fluid dynamics (CFD) code, capable of handling arbitrary multi-scale unstructured tetrahedral meshes and including algorithms to perform dynamic anisotropic mesh adaptivity and mesh movement. The flexibility over mesh structure and resolution that these optimisation capabilities provide makes it potentially highly suitable for accounting the extreme bed morphological evolution close to a fixed solid structure under the action of hydrodynamics. Galerkin-based finite element methods have been used for the hydrodynamics (including discontinuous Galerkin discretisations) and morphological calculations, and automatic mesh deformation has been utilised to account for bed evolution changes while preserving the validity and quality of the mesh.

Finally, the work extends the scope in regards of computational methods and considers scour modelling with pure Lagrangian and meshless methods such as smoothed particle hydrodynamics (SPH), which have also become of interest in the analysis and modelling of coastal sediment transport, particularly in scour-related processes. The SPH modelling is considered in a two-phase, flow-sediment fully Lagrangian scour simulation where the discrete-particle interaction forces between phases are resolved at the interface and continuous changes in the bed profile are obtained naturally.

Declaration and statement of originality

I hereby certify that the work presented in this thesis is the result of my own investigations during the research project. Text and results obtained from other sources are referenced and properly acknowledged.

Following details of collaboration and publications related to this thesis:

- Nunez Rattia J.M., Percival J.R., Neethling S.J., Piggott M.D., Modelling local scour near structures with combined mesh movement and mesh optimisation, J. Comput. Phys. (2018), `https://doi.org/10.1016/j.jcp.2018.09.026`.
- Nunez Rattia J.M., Percival J.R., Yeager B., Neethling S.J., Piggott M.D., Proceedings of the 8th International Conference on Scour and Erosion (Oxford, UK, 12-15 September 2016), Numerical simulation of scour below pipelines using flexible mesh methods, Pages: 101-108. `http://dx.doi.org/10.1201/9781315375045-13`.

To my wife

Acknowledgements

I would like to express my gratitude to:

- Prof. Matthew Piggott for giving me this great opportunity to continue my education with my PhD despite my atypical situation. I would like to say special thanks to him for his thoughtful advice, guidance and his patience. The skills and experience I gained during my PhD will be highly beneficial to me for the rest of my career.

- Prof. Stephen Neethling for his valuable time and constructive comments. Also for the financial support.

- Dr. James Percival for providing his time and knowledge transfer which improved the quality of my current work significantly.

- Dr. Tim Greaves for providing excellent support with the Research Computing Services.

- Imperial College Bursary for providing its financial help.

Contents

List of Tables

List of Figures

Chapter 1

Introduction

Contents

1.1 Motivation and objectives

In marine environments scouring is a type of erosion, which generally involves the removal of granular material or sediment from the surroundings of a hydraulic structure (e.g. pipeline, pier, abutment, groyne) by hydrodynamics forces (e.g. currents, waves, jet flow). Scour represents a threat for coastal structures as it impacts on their long-term stability and survivability. Scour onsets when hydrodynamic bottom shear stresses are higher than sediment critical shear stresses [96]. There are a whole range of hydrodynamic conditions (e.g. accelerated flow due to constrictions, reflected waves, pressure gradients, boundary layer separation, vortices, etc.) which by themselves or by acting in combination result in common scour problems. Significant analytical, numerical and experimental research has been conducted over the last three decades to understand and analyse local scour adjacent to hydraulic structures in coastal zones [65, 95, 103]. There are two commonly used modelling approaches to recreate scouring profiles and sediment fluxes [109]. The first is based on analytic theory, which produces empirical formulae and rules of thumb for prediction of scour depth based on flow around simple two-dimensional objects, such as vertically or horizontally-oriented cylindrical structures, while the second approach involves the numerical solution of potential or turbulent flow models which when coupled with sediment transport equations are able to resolve the scour profile. The latter is more advantageous as when done properly its results are more realistic when considering complex turbulent processes [49, 96].

One particular type of localised, constricted scour pattern due to jet flow which surprisingly little is know about is the phenomenon of *strudel* scour, which occurs mostly during summer times in the Arctic regions when rivers flow at flood capacity as a result of melting ice and snow affecting the near shore bottom topography along the Arctic coast. The melted water quickly inundates the fast ice zones located along the river deltas, radially covering the sheet ice. The added overburden of fresh water is extra-weight to the buoyant ice mass causing the ice to sink in certain weak points. The fresh water then drains down through these cracks and flaws in the ice as well as through seal breathing holes, creating a free vortex or whirlpool (in German, strudel) action as per the draining in a bathtub. The ice buoyancy also provides the fresh water cover with a head for free vortex drainage. The water drains down through the ice with enough velocity to create a vortex action and thus a water jet force on the seabed results in the scouring of bottom sediment. This scour hole normally resembles a circular crater and can vary in size from a few metres up to twenty metres in diameter and as deep as four metres [87]. Research on strudel scour has been done largely based on field observations through multi-beam sonar for bathymetric data collection in shallow waters (see figure 1.1) and compilations of strudel scour occurrences [13].

A variety of mathematical and computational numerical models of scour around hydraulic structures, such as offshore pipelines or wind turbine foundations, have been developed over recent years. These seek to describe the coupling between the hydrodynamic and morphological components of the scouring process. Accurate modelling of scour is im-

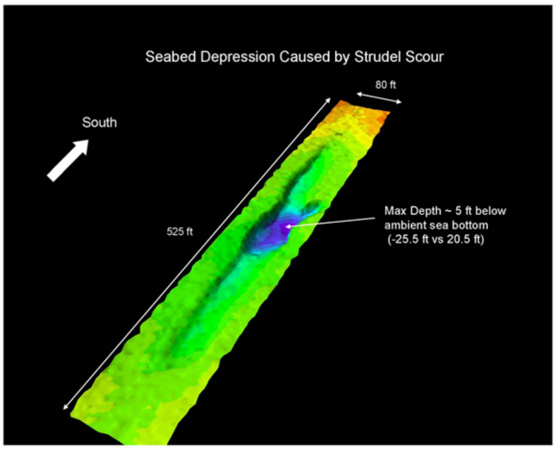

Figure 1.1: Bathymetry of Strudel Scour.
source by: `http://www.coastalfrontiers.com`

portant since this can lead to the damage and failure of hydraulic and marine structures. Large sums of money are spent in the repair of marine structures as a result of scouring [95]. Hence, significant investment is also made in scour protection (e.g. rock fill methods, protective mattresses), guided by predictions of the potential failure mechanisms. Complex numerical models can be used to simulate the (usually turbulent) flow around the structure, ideally with fully coupled two-way interactions with the morphology of the erodible bed. Seabed morphological models involve a sediment transport description to calculate erosion/accretion processes. An important element of the sediment transport description are formulae for the bedload and suspended transport. A summary of the range of models used is provided in section 1.2.

The aim of this research project is to develop efficient simulation methods for sediment transport and scour around hydraulic structures using Imperial College London's, in-house developed geophysical fluid dynamics (GFD), Fluidity code as well as to confirm the applicability of smoothed particle hydrodynamics (SPH) methods (via a SPH simulator code) to further expand their range of multi-physics applications into scour problems which will be capable of predicting complex localised scour induced by different hydrodynamics around different shaped structures. In order to achieve this, the following general objectives were devised for this research project:

1. First, examine background literature thoroughly into different physics and numerical aspects of the scour problem. Information related to the multiple physical processes important to the problem such as sediment dynamics, turbulent hydrodynamics and also information connected to the various approaches used in numerical modelling to resolve scour problems around offshore structures.

2. Develop the corresponding computational modules to account the physics into the codes mentioned above.

3. Perform simulations to understand the benefits and/or shortcomings of the various computational methods for modelling scour processes.

1.2 Local scour modelling

As shown in figure 1.2, the numerical modelling of local scour around offshore structures often comprises and has started its development with single-phase models where the evolution of the scour hole is treated as a two-way coupling phenomenon between the boundary deformation and the flow field. In these models the flow field is firstly simulated with an initial bed morphology using a hydrodynamic model, the shear stresses at the bed boundary are calculated from the flow field and by use of a sediment transportation model where the rate of bed erosion, sediment suspension and bed accretion are estimated and the bed morphology is further updated. At the early stages of research in this area several, authors have developed potential-flow models for the flow inducing scouring below pipelines [49]. Clearly, potential-flow cannot handle wake flow or rotational velocity field; therefore cannot handle the lee-wake erosion, an important stage in the scour process where the vortex shedding convected downstream of the passing structure and controls the rate of scour depth until the process finally reaches a steady state (i.e. equilibrium stage). Because of the aforementioned, advanced models have been implemented, solving the Navier-Stokes equations numerically [8, 43] and thanks to the increasing capacity of modern day computer power it is conceivable to couple the numerical treatment of the continuity and momentum equations with turbulence models such as Reynolds averaged Navier-Stokes (RANS) modelling (e.g. $k - \epsilon$) or large eddy simulations (LES), as well as applying other forms of the Navier-Stokes equations (e.g. stream-function and vorticity) or discrete-vortex methods [96]. Another alternative for local scour modelling is through the use of a two-phase (i.e. flow and sediment) approach discussed below in 1.2.2.

1.2.1 Single phase models

One of the earliest studies to present a holistic dynamic description of the local scour process at submarine pipelines, taking into account both sediment transport contributions (i.e. bedload and suspended transport),

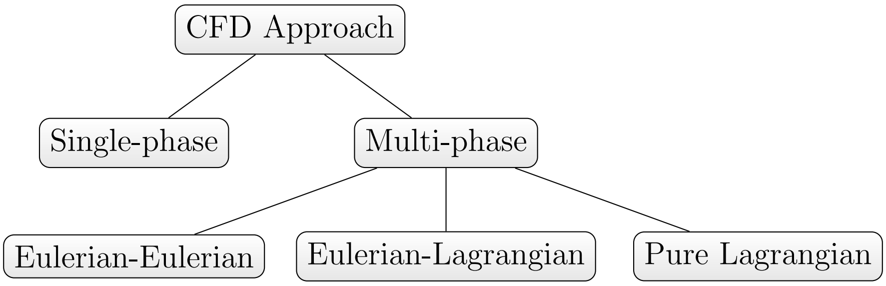

Figure 1.2: Approaches for CFD-based scour modelling.

was performed by Brørs [8]. In that approach the computational mesh evolved in time in order to represent the moving bed location due to scour under a single pipeline. A structured computational grid was utilised with each node in the domain moved vertically, maintaining a relative spacing. But this type of method can lead to problems with resolution and mesh characteristics (e.g. orthogonality and skewness), especially in the case of large bed deformations and where the grid is additionally constrained by the presence of the structure [51, 8, 48].

With the wider development of unstructured grid-based methods in computational fluid dynamics (CFD), a broad range of techniques for arbitrary resolution specification and updating of the computational mesh (i.e. mesh adaptivity) are available. The main motivation for these is to impart both resolution and geometric flexibility as well as to optimise computational efficiency: minimising computational cost for a required accuracy, or maximising accuracy for a given cost. Here a further goal is targeted: the use of this range of techniques to maintain an optimal mesh when subjected to external boundary deformation.

Techniques for optimising the resolution of the mesh include those which perform local topological operations (e.g. sub-dividing elements, or changing mesh connectivity through the swapping of element faces and edges) to change the size, and potentially the shape, of mesh elements. These techniques are variously termed adaptive mesh refinement (AMR), h-adaptivity and mesh optimisation depending on the specifics of the algorithm [28, 83, 84].

A common issue for the single-phase models is that for a reasonably prediction of the bed level change, many assumptions (e.g. critical stress for incipient motion of sediment) and a variety of empirical sediment transport formulae have to be included into the numerical modelling. Also, in order to compute the seabed profile formed by scouring a strategy needs to be included to locally adjust the boundary in an iterative manner and predict the boundary movement allowing a smooth transition of the interior mesh. Computational fluid dynamics (CFD) approaches for moving boundaries tend to fall into two categories: fixed-mesh and moving-mesh. In fixed-mesh methods the fluid containing fraction of each cell must be specified or computed. In the context of free-surface flows, popular techniques include the volume-of-fluid (VOF) method [41] where an equation is solved for the void fraction (between void fractions 0 and 1), and the marker-and-cell (MAC) method [38] where the free surface is tracked by following the motion of particles on the interface. The second practice (i.e. moving-mesh methods), which is explored and adopted by the present work is that of dynamically adapting the mesh in such a way that it is always surface-conforming, i.e. mesh cells always contain fluid (in contrast to VOF) whilst impermeable solid walls and free surfaces coincide with cell faces.

In the past two decades, moving mesh methods (also known as r-adaptive methods) are among several adaptive strategies which have been used for CFD problems [9]. r-adaptivity consists in the r-elocation or r-epositioning of grid points in a mesh having constant connectivity (fixed number of nodes) in such a way that the nodes remain concentrated in regions of rapid variation of the solution fields. Moving mesh methods can be considered in terms of a mapping from a regular domain in a computational or parameter space Ω_C to an irregularly shaped domain in physical space Ω_P [98]. By connecting points in the physical space corresponding to discrete points in the parameter space, the physical domain can be covered with a computational mesh suitable for the solution of finite difference/element/volume equations.

1.2.2 Multiple phase models

Another modelling alternative for scour simulations makes use of multiphase approaches which are gaining popularity due to its capabilities to better represent the flow-sediment interaction. Multiphase models are generally categorised into three approaches:

- Eulerian-Eulerian models, where both the fluid phase and the solid (e.g. soil or sediment layers) phase are treated as continua capable of exchanging properties such as mass and momentum, and the Navier-Stokes equations are solved in an Eulerian frame. The particulate phase is typically consider to be a continuous fluid (approximating the constitutive model for the phase normally as a highly viscous fluid) inter-penetrating and interacting with the fluid phase.

Eulerian models are typically based on cell-averaged quantities and they often struggle with complex interface deformations [112].

- Eulerian-Lagrangian models, in the approach of the coupled Eulerian-Lagrangian (CEL) description where commonly the fluid flow is treated with Eulerian formulation while the sediment particles are described with Lagrangian formulation and both regions continuously interact with each other through a coupling module in which computational information is exchanged either by mapping or by special interface treatments between these two sets of grids [62]. Groups of particles are clustered together interacting with the fluid as parcels and the particle motion (i.e. positions) is calculated by Newton's Laws of Motion, in which friction, collision and gravity are considered. It has been found that using these parcels to represent the particle phase reduces the computational cost significantly instead of an individual particle approach. However, this capability is futile when there is a need to handle dense particulate flows in challenging simulations such as soil liquefaction, for which a pure Lagrangian approach or using Arbitrary Lagrangian-Eulerian methods could be more accurate given that the mesh rezoning approach could offer an better interface resolution in comparison to CEL [3].

- Pure Lagrangian models, explored in the present work in chapter 6, treat both the flow and the particles in a Lagrangian frame of reference. These models typically use mesh-free particle (Lagrangian) methods and have the capability to simulate boundary-interface deformation and fragmentations extremely well [54], hence representing the inherent discrete-particle properties of sediments. One example of particle-based methods includes the smoothed particle hydrodynamics (SPH) for which successful implementations of scour simulations have been promising and further development been promoted [93]. However, these models are particularly demanding in computational resource and another major challenge is that sophisticated (in terms of stability and consistency) turbulence models are still lacking.

In the context of exploring adaptive modelling techniques with this research, a logical extension was to investigate the implicit flexibility of using meshless methods such as SPH compared to mesh-based methods with adaptive mesh refinement (AMR) algorithms.

1.3 Summary of contributions

Amongst the main contributions of this work are the following:

- A fully functioning *hr*-adaptive grid-based capability has been developed for applications with evolving external boundaries, such as local scour near structures, where two-way dynamic coupling between domain geometry (e.g. scour hole in the vicinity of the structure) and resulting fluid dynamics requires the maintenance of overall mesh quality.
- Coupling of the full Navier-Stokes model with the bed evolution model through direct linking of the bed friction velocity to the

tangential wall shear stress at the boundary of the computational domain.

- These novel capabilities have been demonstrated and for some test cases validated using in two- and three-dimensional geometrical configurations.
- Demonstration of the SPH modelling capabilities for scour simulations.

1.4 Thesis structure

The remainder of this thesis is organized as follows. Chapter 2, reviews the governing mathematical equations which are relevant for the physics of local scour and turbulent flows and background theory in the computational methods towards the modelling of this phenomenon.

Chapter 3, elaborates on the hydrodynamic module of the model. The special treatment for wall boundaries is also discussed. A preliminary test case is introduced to test the performance of the turbulence closure components of the hydrodynamic module.

Chapter 4, presents a grid-based numerical discretisation procedure for solving coupled computational fluid dynamics with sediment conservation laws. Also it describes the adaptivity algorithms employes, including mesh movement and optimisation-based anisotropic mesh adaptivity. Numerical experiments for local scour scenarios are carried out in chapters 4 and 5, where validation and benchmarking against physical and numerical experiments are considered with an emphasis on two/three-dimensional (2/3D) applications respectively.

Chapter 6, starts with a brief description of the formulations, mathematical background for the SPH application with geomaterials and afterwards crucial implementation aspects of SPH are noted such as: time integration and instabilities in SPH method, initial and boundary conditions, SPH neighbour search algorithm, and implementation of other numerical aspects to finally analyse the same benchmark problem, already presented in chapter 4.

Finally, chapter 7, discusses the most relevant conclusions of this research and some possible directions for further research.

Chapter 2

Background theory

Contents

2.1 Introduction

Morphodynamics modelling is a broad subject whose fundamentals can be found in various references [74, 33, 109, 96]. Most of these principles have been traditionally used in the modelling of general (coastal or river scale) and local (structural scale) scour problems. The difficulty has been always in the coupling of the sediment modes of transport (normally bedload and suspended load) with the hydrodynamic model (currents and/or waves). The bed changes over time in response to variations of the transport of sediment which is normally referred to as the total volumetric sediment discharge flux, $\mathbf{q_t}$, and can be partitioned as $\mathbf{q_t} = \mathbf{q_b} + \mathbf{q_s}$, where $\mathbf{q_b}$ accounts for contributions of the bedload transport and $\mathbf{q_s}$ for the suspended load transport.

The development of practical engineering coastal morphodynamic modelling tools (e.g. Delft3D by Deltares, Telemac by EDF and Mike by DHI) commonly uses a finite element or volume mesh-based method to discretise the hydrodynamic part comprising either the depth-averaged (two-dimensional) shallow water equations (SWE) or in three-dimensional models, the Navier-Stokes equations on an extruded two-dimensional mesh with multiple layers. For morphodynamics applications this is further coupled with the sediment transport model (described in section 2.2.3); and the bed evolution model via the Exner equation (described in section 2.2.4).

Two-dimensional large-scale morphodynamic models are commonly based on a depth-integration of the incompressible shallow water equations coupled with the sediment transport discharge equation or Exner equation.

This SWE-Exner scheme has proven to be able to offer satisfactory results, specially in the modelling of general scour which depends primarily on the sediment movement over relatively large horizontal scales, irrespective of the presence of the structure. However, in the three-dimensional modelling of localised scour around structures, the physics of the flow are considerably altered due to: flow separation, formations of lee-wake vortices, horseshoe vortices, producing streamline contraction and local accelerations and this requires the use of a more complete model for the fluid flow simulation, rather than a two-dimensional shallow water model. As presented in figure 2.1, commercial packages [73, 39] for morphodynamics are able to model local scour around structures through a simple extrusion along the vertical direction, but their capabilities are limited when the modelling of more complex structures is considered such as per the scour near a horizontal pipe.

The bed shear stress around the structure bottom is the most important factor that directly controls the pattern of scouring. Ideas of excess shear stress-based empirical formulae have been considered for years but still there are debates about how to express the bed shear velocity given that the local fluid velocities are difficult to measure directly, and a depth-averaged flow speed is often used instead. The bed shear stress can be obtained from the flow field solution of the governing equations in several ways, one of the simplest for example, is a linear relationship with the square of the mean flow speed. More advanced formulations take into

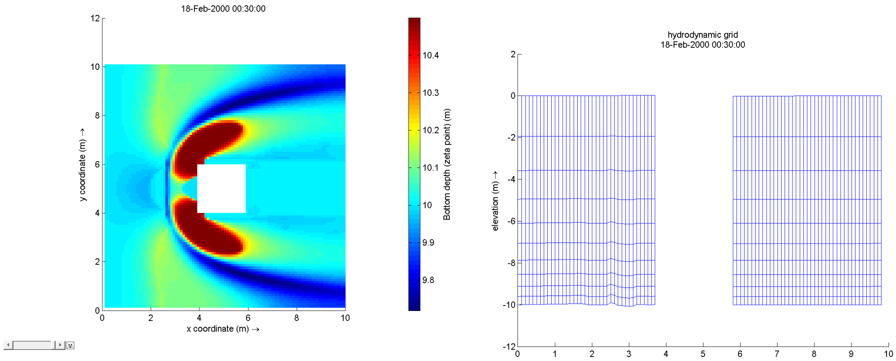

(a) Bottom scour depth (m) - Delft3D.

(b) Elevation profile (m) - Delft3D.

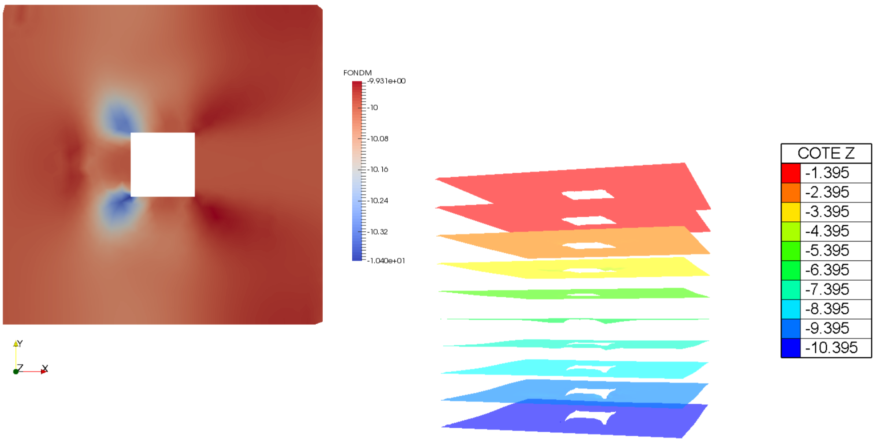

(c) Bottom scour depth (m) - Telemac.

(d) Elevation profile (m) - Telemac.

Figure 2.1: Example of local scour around a square abutment under a constant current, simulated in Delft3D and Telemac (with its sediment transport module, Sisyphe).

account theoretical assumptions about the structure of the turbulence which provide a local measure of the shear stress (i.e. at the bottom). This study make use of a wall function formulation to determine the local shear stress connected to the near wall tangential velocity which is considered an extension of the commonly used formulation from Engelund & Fredsøe [22] to obtain the bedload contribution in the mean transport direction.

Amongst the objectives of this work is to propose a flexible modelling approach to simulate the scour process with a complete flow model based on the Navier-Stokes equations coupled with the Exner equation in any two- or three-dimensional scenario, but also considering any kind of embedded geometries using a finite element mesh. This work also presents an alternative way (to the commonly used quadratic stress law bed shear stress formulation) to accurately model the coupling of the full Navier-Stokes model with the bed sediment transport, linking the bottom friction velocity to the tangential wall shear stress at the boundary of the computational domain in a near-wall modelling for turbulent flows, as shown in chapter 3.

The next section presents the mathematical formulations for the turbulent flow field model, the sediment transport and bed evolution model and lastly, a description of the smooth particle hydrodynamics approach for the modelling of fluid flow is included.

2.2 Mathematical equations

2.2.1 Flow model

The approach taken here for the simulation of hydrodynamics in the single-phase modelling approach is to consider the solution of the incompressible Navier-Stokes equations, where the density of the fluid does not change with pressure, i.e. $\rho_f = constant$, and the energy equation decouples from the rest of the system resulting in the fluid flow modelled by partial differential equations (PDEs) describing the conservation of mass and momentum. These fundamental equations are based in conservation laws of the flow variables considering a fixed control volume (Ω). The rate of change in the control volume can be expressed as

$$\frac{d}{dt}\int_{\Omega} \Phi d\Omega = \int_{\Omega} \frac{\partial \Phi}{\partial t} d\Omega + \int_{\Gamma} \Phi \mathbf{u} \cdot \mathbf{n} d\Gamma = \int_{\Omega} S d\Omega, \tag{2.1}$$

for some quantity Φ, where Ω is the domain occupied by the control volume, Γ is the surface boundary for Ω, $\mathbf{n}$ is the boundary surface outward unit normal, S represents a source or sink term acting on the domain and $\mathbf{u} = (u, v, w)^T$ is the velocity field in Cartesian coordinates. This is commonly known as the Reynolds transport theorem. Using the general form of a conservation equation (2.1), the conservation of mass (in integral form) can be written

$$\frac{\partial}{\partial t}\int_{\Omega} \rho d\Omega + \int_{\Gamma} \rho \mathbf{u} \cdot \mathbf{n} d\Gamma = 0, \tag{2.2}$$

noting that the density is the one corresponding to the fluid and sediment mixture ρ but the fluid density, ρ_f is constant (incompressibility condition) in this work resulting in a continuity equation (for the fluid only) with a non-divergent velocity field

$$\nabla \cdot \mathbf{u} = 0. \tag{2.3}$$

The momentum equation in the fluid is given by $\rho\mathbf{u}$ and the density ρ can be expressed in terms of sediment concentration, c by using an equation of state, $\rho = \rho_f + \left(\rho_s - \rho_f\right) c$, where ρ_s is the sediment particle density, $\rho_f = 10^3\ kg/m^3$ is a reference water density (assumed for this work) and finally ρ represents the density of the fluid and sediment mixture (note that in the applications considered here the density variations due to suspended sediment concentration dominate all other state variables dependencies and they are assumed to have a linear dependence on the sediment concentration in the equation of state)

$$\frac{\partial}{\partial t} \int_{\Omega} \rho \mathbf{u} d\Omega + \int_{\Gamma} \rho \left(\mathbf{u} \otimes \mathbf{u}\right) \cdot \mathbf{n} d\Gamma = \sum f_{\rho\mathbf{u}}, \tag{2.4}$$

where $\mathbf{u} \otimes \mathbf{u}$ is a rank-2 tensor with entries $u_i u_j$ (throughout this work summation over repeated indices is implied). The right-hand side, $f_{\rho\mathbf{u}}$, is based on Newton's second law of motion and it represent the forces acting on the whole domain, split into body forces acting in the interior volume, such as the gravity force $\mathbf{g} = (0, 0, -g)^T$ pointing in the negative vertical direction and surface forces decomposed into the pressure force

$-p\mathcal{I}$ and the viscous force $\boldsymbol{\tau} \cdot \mathbf{n}$, where $\boldsymbol{\tau}$ is the Cauchy stress tensor:

$$\sum f_{\rho \mathbf{u}} = \int_{\Omega} \rho \mathbf{g} d\Omega - \int_{\Gamma} p \mathbf{n} d\Gamma + \int_{\Gamma} \boldsymbol{\tau} \cdot \mathbf{n} d\Gamma. \tag{2.5}$$

It is further assumed that the viscous stress tensor is linearly related to the strain rate (i.e. Newtonian fluids assumed)

$$\boldsymbol{\tau} = \mu \left(\nabla \mathbf{u} + (\nabla \mathbf{u})^T \right) - \frac{2}{3} \mu \left(\nabla \cdot \mathbf{u} \right) \mathcal{I}, \tag{2.6}$$

where $\mathcal{I}$ is the identity matrix and μ is the molecular, or dynamic viscosity. Applying the divergence theorem

$$\int_{\Omega} \nabla \cdot f\left(\mathbf{x}\right) d\Omega = \oint_{\Gamma} f\left(\mathbf{x}\right) d\Gamma, \tag{2.7}$$

to the integral form of the momentum equation (2.4) together with the incompressibility condition mentioned in equation (2.3), the momentum equation can be simplified further to

$$\frac{\partial \rho \mathbf{u}}{\partial t} + \rho \mathbf{u} \cdot \nabla \mathbf{u} = -\nabla p + \nabla \cdot \left(\mu \left(\nabla \mathbf{u} + (\nabla \mathbf{u})^T \right) \right) + \rho \mathbf{g}. \tag{2.8}$$

For small density variations (i.e. here relatively diluted sediment concentrations), the density ρ can be treated as a constant and replaced by ρ_f in all terms of the momentum equation, except where the density is multiplied by gravity (i.e. buoyancy term). This condition, $|\rho - \rho_f| \ll \rho_f$ is known as the Boussinesq buoyancy approximation and the resulting form of the momentum equation is then

$$\frac{\partial \mathbf{u}}{\partial t} + \mathbf{u} \cdot \nabla \mathbf{u} = -\nabla \left(\frac{p}{\rho_f} \right) + \nabla \cdot \left(\nu_0 \left(\nabla \mathbf{u} + (\nabla \mathbf{u})^T \right) \right) + \frac{\rho}{\rho_f} \mathbf{g}, \tag{2.9}$$

where $\nu_0 = \mu \rho_f^{-1}$ is a reference fluid kinematic viscosity, assumed to be $\nu_0 = 10^{-6}\, m^2/s$ for water in this work. The formulation in (2.9) is given in a non-conservative form and the stress divergence is expressed in its partial stress form which is the preferred form of the viscous term for incompressible flow with spatially varying viscosity.

Equations (2.3) and (2.9), need to be solved with appropriate initial and boundary conditions which will be considered later with the domain simulations from chapters 4 and 5.

The solution procedure for velocity $\mathbf{u}$ and pressure p, presents a mathematical difficulty for the determination of the pressure (since it does not involve a time derivative) which involves the use of a projection scheme which decouples the $\mathbf{u}$ and p problems, and separates the advection-diffusion part of the momentum equation from incompressibility. The scheme projects an intermediate velocity, $\mathbf{u}_*$ onto the subspace of solenoidal (divergence-free) functions resulting in a Poisson pressure equation (derived from a pressure-correction step with an initial guess pressure) and obtain a pressure correction Δp to correct $\mathbf{u}_*$ and finally obtain the new velocity and update the pressure. Further details may be found in [1].

2.2.2 Turbulence model and closure

The formulae developed for morphological calculations (e.g. bedload sediment transport) were obtained for steady-state turbulent flows (high Reynolds number) where the boundary layer conditions are under fully developed turbulence [95]. In order to account for the turbulence within the flow, a turbulence model needs to be integrated into the solution of the Navier-Stokes equations. Describing the turbulence in the flow corresponds to the use of a model capable of approximating the effect of the small scales (in space and time) of motion in the flow. Through direct numerical simulation (DNS) all the scales (time and space) of turbulence can be resolved without the need to average or to filter but, this requires extremely fine grids and timesteps and so this approach is generally limited to small Reynolds numbers. In regards to turbulence modelling approximating spatial scales another alternative is the popular large eddy simulation (LES) technique which is based on the assumption that the large scale motions are normally more energetic than small scale so, only large scales are resolved numerically (as per DNS) and small scales are modelled by using a subgrid-scale model (SGS). This technique is an active area of research and is preferred over DNS for high Reynolds number simulations or complex geometries. LES is computationally less costly than DNS but it is probably still too demanding for many engineering applications.

The most common turbulence modelling used in many real-life flows at moderate to high Reynolds number is the approach called Reynolds-averaged Navier-Stokes (RANS) which is a simplification of the turbulence process assuming that the separate fluctuations of the flow are not required and mean flow fields are enough. Only time averages are considered,

$$\bar{\mathbf{u}}\left(x,t\right)=\frac{1}{\delta}\int_{t}^{t+\delta}\mathbf{u}\left(x,\tau\right)d\tau. \tag{2.10}$$

After averaging in the Navier-Stokes equations (2.3) and (2.9), the RANS momentum equation results in

$$\frac{\partial\mathbf{u}}{\partial t}+\mathbf{u}\cdot\nabla\mathbf{u}=-\nabla\left(\frac{p}{\rho_f}\right)+\nabla\cdot\left(\nu\left(\nabla\mathbf{u}+\left(\nabla\mathbf{u}\right)^T\right)\right)+\frac{\rho}{\rho_f}\mathbf{g}, \tag{2.11}$$

where $\nu=\nu_0+\nu_t$ represents the sum of the constant background kinematic viscosity plus the spatially varying turbulent eddy viscosity. Also note that $\mathbf{u}$ is the averaged velocity, $\bar{\mathbf{u}}$ calculated by (2.10) but for simplicity the overbar notation has been dropped. RANS equations are developed from the unsteady, three-dimensional Navier-Stokes equations considering just the time-averaged values and condensing the unsteady structures of small sizes in space and time into an error by omission accounted for through the so-called Reynolds stress term (i.e. $-\overline{\mathbf{u'}\otimes\mathbf{u'}}$) which contains the fluctuations $\mathbf{u'}$, and this effect needs to be modelled. These turbulent stresses have to be interpreted in terms of some known variables in order to close the system of equations (this is the well-know turbulence closure problem). In this work, the closure problem is tackle with the use of linear eddy-viscosity models, where the main idea is to represent the Reynolds stress tensor as a linear relationship with the mean strain rate:

$$-\overline{\mathbf{u}' \otimes \mathbf{u}'} = -\frac{2}{3}k\mathcal{I} + \nu_t \left(\nabla \bar{\mathbf{u}} + (\nabla \bar{\mathbf{u}})^T \right), \tag{2.12}$$

where $k = \overline{(\mathbf{u}' \cdot \mathbf{u}')}/2$ is the mean turbulent kinetic energy and ν_t is the kinematic eddy viscosity. There are many subcategories of eddy-viscosity models, depending on the number of transport equations required to computed the eddy viscosity coefficient. The standard RANS, two-equation, $k-\epsilon$ turbulence model is used in this study (following the benchmarking analysis shown in chapter 4) to parametrise unresolved mixing length scales through a turbulent or eddy viscosity, ν_t. Two coupled scalar advection-diffusion-reaction equations are solved to determine the magnitude of the turbulent eddy viscosity, defined as

$$\nu_t = C_\mu \frac{k^2}{\epsilon}, \tag{2.13}$$

where $C_\mu = 0.09$ is an empirically chosen constant, k is the turbulent kinetic energy (TKE) and ϵ is the TKE dissipation rate. The two additional prognostic equations, which are also coupled to the momentum equation (2.11), take the form

$$\frac{\partial k}{\partial t} + \nabla \cdot \left(k\mathbf{u} - \left(\nu_0 + \frac{\nu_t}{\sigma_k} \right) \nabla k \right) = P_k - \epsilon, \tag{2.14}$$

$$\frac{\partial \epsilon}{\partial t} + \nabla \cdot \left(\epsilon\mathbf{u} - \left(\nu_0 + \frac{\nu_t}{\sigma_\epsilon} \right) \nabla \epsilon \right) = \frac{\epsilon}{k} \left(C_1 P_k - C_2 \epsilon \right), \tag{2.15}$$

where $P_k = \frac{\nu_t}{2}\left(\left\|\nabla\mathbf{u} + (\nabla\mathbf{u})^T\right\|^2\right)$ and ϵ account for the production and dissipation of turbulent kinetic energy, respectively. The values of $\sigma_k = 1.0$, $\sigma_\epsilon = 1.3$, $C_1 = 1.44$ and $C_2 = 1.92$ are further empirically chosen constants.

For the applications of this work (i.e. channel flow), the turbulence model is divided into two regions: (i) the outer or core flow turbulent zone and (ii) the wall or near-wall layer. Near the wall, the gradients of the properties of the fluid are much higher compared to the core region of the flow, which requires the use of wall functions to avoid the need to use a very fine mesh. Equations (2.14) and (2.15), need to be solved with appropriate initial and boundary conditions which will be further develop in chapter 3 and later considered with the domain simulations from chapters 4 and 5.

2.2.3 Sediment transport model

Sediment transport simulations are based on the global mass conservation of flux (i.e. flow, Q_f and sediment rate, Q_s) principle as shown in figure 2.2.

Simulations of sediment transport coupled with boundary (i.e. bed) evolution obey a fundamental mass balance conservation law (the Exner equation) and they are commonly performed under the discretisation of a particular form of the general bed level change equation [80]

$$\frac{\partial \eta}{\partial t} = -\frac{1}{1-n}\left[\nabla\cdot(\mathbf{q_b} + \mathbf{q_s}) + \frac{\partial}{\partial t}\int_{\eta}^{\eta+H} c\,dz\right], \tag{2.16}$$

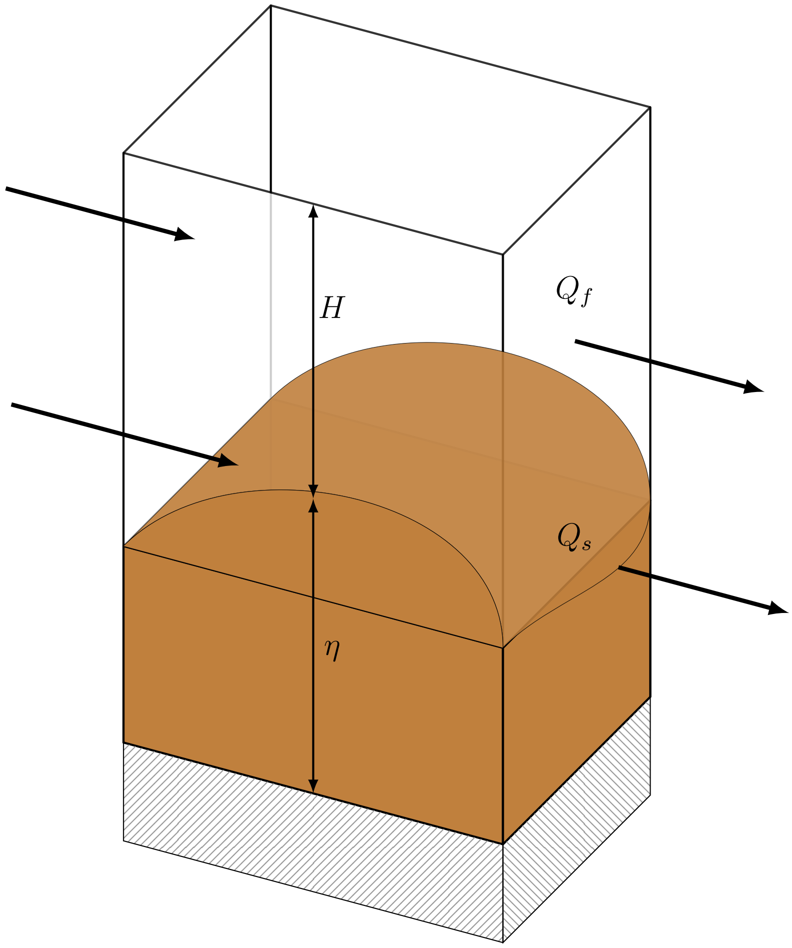

Figure 2.2: Schematic of the two-layer flow/sediment transport system where Q_f and Q_s represents the flow and sediment fluxes respectively.

where, $\eta(x, y, t)$ represents the bed level, n is the porosity of the bed, and $\mathbf{q_b}$ and $\mathbf{q_s}$ are the bedload rate and suspended rate vectors, respectively. The final term on the right-hand side represents the temporal change in the volume of sediment in the water column of height H, where c denotes sediment concentration. The total sediment transport is handled by splitting it into bedload and suspended load contributions. The approaches for these two types of sediment transport are detailed below. The sediment transport formulations in this work are limited to compacted (i.e. no void space, $n = 0$) well-graded sands.

2.2.4 Bed evolution model

Morphological changes to a given bathymetry occur when there is an inequilibrium between deposited and eroded material in a localised region. If the amount of deposited material exceeds the amount of eroded material, it leads to an increase in bed level and vice versa. This mechanism is described by the Exner equation (2.16) for sediment transport in a simpler form [27]:

$$\frac{\partial \eta}{\partial t} = -\frac{1}{1-n}\left(\nabla_{\text{surf}} \cdot \mathbf{q_b} + (E - D)\right) \tag{2.17}$$

where, the morphological change is split into contributions from the surface divergence,

$$\nabla_{\text{surf}} \cdot = \left(\frac{\partial}{\partial x}, \frac{\partial}{\partial y}, 0\right) \cdot, \tag{2.18}$$

of the bedload transport and the suspended sediment transport, where E and D represent erosion and deposition respectively.

It is worth noting that the rate of bed change as expressed in (2.17) depends on scalar quantities (i.e. D and E), which results in a major simplification for the suspended sediment transport given that the numerical integration of the storage term over the vertical direction (last term in (2.16)) is replaced by evaluating the suspended sediment deposition and entrainment rates.

2.2.4.1 Bedload transport

Bedload transport is the part of the sediment transport load taking place at the bed surface resulting in the motion of particles due to rolling, sliding or travelling in small jumps (saltation) along the bed. Many aspects of sediment morphodynamics are governed predominantly by the bedload transport rate, including river erosion, bed form evolution, and potentially the scour around structures such as pipelines or bridge abutments.

Numerous bedload transport formulations appear in the literature and generally consist of semi-empirical relations derived from flume-based experimental data. The bedload transport rate is then calculated as a function of the magnitude of bed/wall shear stress, $\|\boldsymbol{\tau_w}\|$, above its critical value, $\boldsymbol{\tau_c}$. Dimensional analysis then leads to the dimensionless relationships (expressed with a superscript $*$) for the bedload sediment transport rate, $\mathbf{q}^* = f\left(\tau^*, d^*, R^*, Re_p^*\right)$, where,

$$
\begin{aligned}
\mathbf{q}^* &= \frac{\mathbf{q_b}}{\sqrt{R^* g d_{50}^3}}, && \text{(Einstein number)}\\
\tau^* &= \frac{\|\boldsymbol{\tau_w}\|}{\rho R^* g d_{50}}, && \text{(Shields number)}\\
d^* &= d_{50}\left[\frac{R^* g}{\nu_0^2}\right]^{1/3}, && \text{(Dimensionless particle diameter)}\\
R^* &= \frac{(\rho_s - \rho_0)}{\rho_0}, && \text{(Submerged specific gravity)}\\
Re_p^* &= \frac{\sqrt{R^* g d_{50}^3}}{\nu_0}. && \text{(Particle Reynolds number)}
\end{aligned}
$$

Generally, granular bed-material will remain still in the bed until the flow initiates incipient motion. This is termed the threshold of motion, with the bed shear stress that induced it, referred as the critical stress, $\boldsymbol{\tau_c}$. One fitting to experimental data for this critical stress is given by Soulsby [92] in the following equation

$$\tau_c^* = \frac{0.30}{1+1.2d^*} + 0.055\left[1 - e^{-0.020d^*}\right]. \tag{2.19}$$

Amongst the many bedload transport formulae proposed in the literature with an applicability range for relatively small particle diameters $190\,\mu m < d_{50} < 930\,\mu m$ (where d_{50} is the median particle diameter), the following list in table 2.1 presents some of the most commonly used bedload formulation options implemented in Fluidity [1]. By any means, this does not represent a comprehensive compilation of all transport formulas, for further reading consult the work by Garcia [29],

Authors	Transport Rate, $\mathbf{q}^*$	Derivation
Meyer-Peter & Müller [1948]	$8\left(\tau^* - \tau_c^*\right)^{3/2}$	Experimental
Engelund & Fredsøe [1976]	$18.74\left(\tau^* - \tau_c^*\right)\left(\sqrt{\tau^*} - 0.7\sqrt{\tau_c^*}\right)$	Theoretical
Van Rijn [1984]	$\frac{0.053}{d^*}^{0.3}\left(\frac{\tau^*}{\tau_c^*} - 1\right)^{2.1}$	Experimental
Nielsen [1992]	$12\left(\tau^* - \tau_c^*\right)\sqrt{\tau^*}$	Experimental

Table 2.1: Commonly used formulas to describe bedload transport in a turbulent flow.

2.2.4.2 Bed slope control

Most bedload sediment transport formulae are derived and calibrated for rivers with shallow slopes [33]. In excess shear stress scour conditions where a local obstruction (e.g. pipeline or bridge pier) is present, the localised increase in shear stress during the development of scour holes may lead to areas in a model where the local face slope exceeds the angle of repose, ϕ, which is a geotechnical parameter to measure the stability of sediment particles (somewhere between $30° < \phi < 35°$ for loose sands). Numerical algorithms have been proposed to overcome these difficulties in modelling the over-steepening of the bed slope and allow the bed-material to slide down through the adjustment of the bedload flux of sediment in a conservative fashion.

Aspley et al. [2], described a flux based algorithm which prescribes an additional *avalanche flux* which is added to the bedload flux, based on the angle of the actual slope, α, and the direction of steepest slope, $\mathbf{b} = \nabla\eta / \|\nabla\eta\|$. This takes the form,

$$\mathbf{q}_{\text{aval}} = \begin{cases} (1-n)\,\frac{L^2\big(\tan(\alpha)-\tan(\phi)\big)}{2\cos(\alpha)\Delta t}\mathbf{b}, & \tan(\alpha) > \tan(\phi)\,, \\ 0, & \text{otherwise}, \end{cases} \tag{2.20}$$

where L (related to the cell length) and Δt (current timestep) are dimensional values arising from the problem being modelled.

This avalanche flux based approach was used in this work. Other algorithms for sand sliding follow a more geometric approach. For example, Liang et al. [51], described a one-dimensional method which lowers the slope of a cell's facet to yield a new stable slope, but this approach leaves an open issue regarding mass conservation. Another similar idea in Niemann et al. [76] is proposed by setting the new positions of the vertices constituting the sliding face, derived from a function that behaves like the avalanche flux and raises/lowers the bed level according to the mass balance of sediment (i.e. area distribution). This addresses the issue of conservation but it is a method geometrically designed just for one-dimensional slope control.

Interesting corrections to the critical Shields parameter have been considered to account for slope effects [2]. In the case of sandy areas, $\boldsymbol{\tau_c}$ can be neglected and the use of simpler models [92] which do not take the incipient motion theory into account can be satisfying. For that reason, in this study no local slope correction was added into the bed shear stress calculation to account for the critical shear stress reduction at incipient motion on a sloping bed.

2.2.4.3 Suspended load transport

Suspended sediment transport involves the particulate material that is carried within the water column. These particles are kept in suspension due to turbulent mixing causing an upward flux which competes with the inherent downward particle settling velocity, u_{si}, obtained by balancing buoyancy effect with the Stokes drag.

The sediment concentration, c, is the volume of sediment per total volume of material (fluid and sediment). The suspended sediment concentration can be determined by solving an advection-diffusion equation, with an additional convective term to represent the gravitational effect of the settling velocity:

$$\frac{\partial c}{\partial t} + \nabla \cdot \left[c \left(\mathbf{u} - u_{si}\mathbf{k} \right) \right] = \nabla \cdot \left(\kappa \nabla c \right), \qquad \text{where} \qquad \kappa = \kappa_0 + \frac{\nu_t}{S_c^*}. \quad (2.21)$$

The magnitude of the particle concentration eddy diffusivity κ, is inversely proportional to the Schmidt number, S_c^*, which represents a ratio of the momentum diffusivity (total viscosity) and mass diffusivity (sediment concentration) and is generally chosen to be in the range 0.7 – 1.0. In the rest of this work $S_c^* = 1$ is assumed.

The settling velocity is obtained from the formula for unhindered sand particles (valid for diameters $d_{50} > 100\,\mu m$) in clear-water [92]:

$$u_{so} = \frac{\nu_0}{d_{50}} \left[\left(10.36^2 + 1.049 d^{*3} \right)^{1/2} - 10.36 \right]. \tag{2.22}$$

As the sediment concentration rises the settling velocity usually drops, which is essential to account for in the actual suspended sediment concentration effect [88], resulting in the correction $u_{si} = u_{so}\left(1 - c\right)^{2.39}$.

The terms of the suspended sediment load can be expressed using empirically-derived relations which describe changes in the volume of sediment in the water column together with the suspended sediment load vector (i.e. $\mathbf{q_s}$). The deposition rate, $D = u_{si} c_0$, is calculated from the settling velocity of the sediment particles, denoted u_{si}, multiplied by the near-the-bed concentration (c_0). The erosion or entrainment rate,

$$E = -\kappa \frac{\partial c}{\partial z}, \tag{2.23}$$

can be expressed in terms of the local turbulent eddy diffusivity (κ) and the vertical concentration gradient, or equivalently the *turbulent* flux of particles up from the bed. Many empirical formulations are available in the literature for estimating the re-entrainment rate of suspended sediment. Some studies [30, 102] have performed detailed comparison of formulae and validated these against laboratory results. In this work the model of van Rijn [102] is selected (following the benchmarking analysis shown in chapter 4) where the entrainment rate can be written in dimensionless form as

$$E^* = \frac{E}{u_{si}} = 0.015\frac{d_{50}\Psi^{1.5}}{Z_b {d_*}^{0.3}}, \qquad \text{where} \qquad \Psi = \frac{\boldsymbol{\tau}^*}{\boldsymbol{\tau}_c^*} - 1, \tag{2.24}$$

d_{50} is the median particle diameter and Z_b represents a reference level very near the bed close in value to the sand roughness. The reference level assumed was $Z_b = 3d_{90}$, where d_{90} represents the grain diameter of the 90th percentile (90% of sediment is finer).

2.2.5 Smooth particle hydrodynamics modelling

Smoothed Particle Hydrodynamics (SPH) method is a particle method which pioneered the mesh free idea dating back from the seventies [31, 61]. It is a pure Lagrangian particle method which uses a smoothing function to find continuous interpolations of the fluid properties between discrete particles. The particles carry all the quantities and no grid is needed. The general conservation laws (for mass and momentum) for fluid motion described in 2.2.1 can be combined with SPH approximations to derive and solve the full Navier-Stokes equations. The basis of its approach are in kernel estimates method [67] which produces a SPH approximation function, to any variable (scalar or vector field) ϕ defined on the spatial coordinates $\mathbf{r}$,

$$\phi(\mathbf{r}) \approx \sum_{b}^{N} m_b \frac{\phi_b}{\rho_b} W_{ab}, \tag{2.25}$$

where, $W_{ab} = W\left(\|\mathbf{r_a} - \mathbf{r_b}\|, h\right)$ represents a smoothing or kernel function with smoothing length, h. This approximation (in discrete notation) refers to the quantity (i.e. ϕ_b) being evaluated at the position of particle b. The mass and density are denoted by m_b and ρ_b respectively.

Similar approximations can be derived for the gradients of the function,

$$\nabla\phi(\mathbf{r}) \approx \sum_{b}^{N} m_b \frac{\phi_b}{\rho_b} \nabla_a W_{ab}, \tag{2.26}$$

where it is assumed that the gradient is evaluated at another particle a. Also for the Laplacian operations,

$$\nabla^2\phi(\mathbf{r}) \approx \sum_{b}^{N} m_b \frac{\phi_b}{\rho_b} \nabla_a^2 W_{ab}. \tag{2.27}$$

The smoothing kernel, W is a key component on the performance of the SPH method. Amongst its properties, it has a compact support domain which value decreases monotonically as the distance between particles increases. Its radius is defined by the smoothing length, h and they are normalised and need to satisfy the requirement that in the limit case, when h goes to zero, the smoothing function tends to the delta or Dirac function. The development of kernels is an active research area [106] in one, two and three dimensions but the simplest kernel is the Gaussian,

$$W\left(\|\mathbf{r}\|, h\right) = \alpha_d e^{-q^2}, \tag{2.28}$$

where, $q = \|\mathbf{r}_{ab}\| h^{-1}$ is the non-dimensional distance between particles, $\|\mathbf{r}_{ab}\| = \|\mathbf{r_a} - \mathbf{r_b}\|$ and $\alpha_d = \left[1/\sqrt{\pi}h, 1/\pi h^2, 1/\left(\pi\sqrt{\pi}\right)h^3\right]$ in [1,2,3] dimensions is an scaling factor. Unfortunately, the Gaussian kernel does not possess a compact support, given that the interpolation spans the entire spatial domain. Kernels similar to the Gaussian shape but also with compact support which are commonly use in SPH practice are [54]: (i) quadratic, (ii) cubic spline, (iii) quintic.

In order to approximate the conservations laws for fluid flow, the SPH interpolation relations (2.25), (2.26) and (2.27), are used as an extension from the work by Monaghan [68]. For the conservation of mass given by the continuity equation (2.2) in general quasi-incompressible form, the density (i.e. the quantity, ϕ) takes the form

$$\rho_a = \sum_b^N m_b W_{ab}, \tag{2.29}$$

and taking the (Lagrangian) time derivative, it is obtained,

$$\frac{D\rho_a}{Dt} = \sum_b^N m_b \left(\mathbf{u_a} - \mathbf{u_b}\right) \cdot W_{ab}. \tag{2.30}$$

As suggested before, this SPH model implies a slightly compressible fluid. In order to calculated the pressure for the momentum equation an equation of state linked to the density is used and in that way an implicit

Poisson equation for the pressure is no longer necessary. The often used Tait equation of state is

$$p_a = p_0 + B\left[\left(\frac{\rho_a}{\rho_0}\right)^{\gamma} - 1\right], \tag{2.31}$$

where, $\gamma = 7$, $B = c_0^2\rho_0/\gamma$ is a problem dependant parameter, $\rho_0 = 10^3\, kg/m^3$ is a reference (e.g. water) density, p_0 is the reference pressure and c_0 is the fluid speed of sound at the reference density.

The momentum conservation equation derived from (2.4) in its Lagrangian form for an incompressible Newtonian fluid is

$$\rho\frac{D\mathbf{u}}{Dt} = -\nabla p + \mu\nabla^2\mathbf{u} + f_{\rho\mathbf{u}}, \tag{2.32}$$

noting that the material derivative notation of velocity is used as a result of that in smoothed particle hydrodynamics, quantities are stored in the Lagrangian perspective making the convective term from the Eulerian perspective effectively automatic as the moving particles travel with the flow field. Further, following a derivation of the diffusive terms using an artificial viscosity, the particle approximation of the Navier-Stokes equations, inclusive viscous terms and with a symmetric pressure gradient becomes

$$\frac{D\mathbf{u_a}}{Dt} = -\sum_{b}^{N} m_b\left(\frac{p_a}{\rho_a^2} + \frac{p_b}{\rho_b^2} + \Pi_{ab}\right)\nabla_a W_{ab} + f_a, \tag{2.33}$$

where, f_a is the acceleration due to a body force (e.g. gravity) acting on particle a with respect to another particle b. The term, Π_{ab} is an artificial viscosity modelled

$$\Pi_{ab} = \begin{cases} -\frac{\alpha h \overline{c_{ab}}}{\overline{\rho_{ab}}} \frac{\mathbf{u}_{ab} \cdot \mathbf{r}_{ab}}{\|\mathbf{r}_{ab}\|^2 + 0.01h^2}, & \mathbf{u}_{ab} \cdot \mathbf{r}_{ab} < 0, \\ 0, & \mathbf{u}_{ab} \cdot \mathbf{r}_{ab} \geq 0, \end{cases} \tag{2.34}$$

where, $\overline{\rho_{ab}} = (\rho_a + \rho_b)/2$ is the average density, $\overline{c_{ab}} = (c_a + c_b)/2$ is the average speed of sound in the fluid and α is a free constant chosen normally $0.01 < \alpha < 1$. There exist others formulations for the viscous terms, $\nu \nabla^2 \mathbf{u}$ in (2.32) for example, considering a laminar stress viscosity [56] and resulting in a momentum conservation equation like

$$\frac{D\mathbf{u_a}}{Dt} = -\sum_{b}^{N} m_b \left[\left(\frac{p_a}{\rho_a^2} + \frac{p_b}{\rho_b^2} \right) \nabla_a W_{ab} + \left(\frac{4\nu_0 \mathbf{r}_{ab} \nabla_a W_{ab}}{(\rho_a + \rho_b) \|\mathbf{r}_{ab}\|^2} \right) \mathbf{u}_{ab} \right] + f_a, \tag{2.35}$$

where, ν_0 is a reference kinematic viscosity of laminar flow (e.g. $\nu_0 = 10^{-6}\, m^2/s$ for water).

In chapter 6, SPH capabilities to model soil deformations as a viscoplastic fluid or as a elastoplastic solid material with a yield failure criteria will be discussed together with more details about its implementations.

Chapter 3

Turbulence modelling

Contents

3.1 Introduction

As discussed at the end of section 2.2.2 from chapter 2, in regards to the treatment of the near wall layer region, the turbulence properties close to the wall are generally much higher compared to the core region of the flow. Within a RANS framework, two discretisation approaches are typically utilised to allow for suitable representation of the near wall flow. The first, is a low-Reynolds number model in which boundary conditions are selected for both k and ϵ at all solid boundaries and the effects of the molecular viscosity are included via damping factors in the eddy viscosity and the dissipation equation [82]. Low-Reynolds $k-\epsilon$ modelling requires very fine resolution to capture the distance to the closest solid boundary [17] and for true environmental flows (i.e. high Reynolds numbers) with rough surface boundaries this level of resolution adds a non-desirable computational cost. The other option is a high-Reynolds number model where a wall function is prescribed analytically at the bed to avoid the need for very fine mesh. The near wall discretisation in this work is based on a wall function formulation which will be described below in more detail.

Both of these boundary discretisation models aim to ensure that the boundary layer is well resolved, and in connection to sediment transport modelling it should be emphasised that, the boundary layer is the most important part of the flow which influences the modes of transport of the particulate material mainly as a function of the shear stresses it induces at the bed [74].

3.2 Boundary conditions for high-Reynolds number model

In near-wall modelling using the two-equation $k-\epsilon$ model for turbulent flows there is an alternative approach where *Law of the Wall* functions are considered, this is currently a working area in the industrial turbulence computation.

In wall-attached boundary layers, the normal gradients of the flow variables become large as the wall distance decreases. Significantly close to the wall the turbulent fluctuations are suppressed and eventually viscous effects become important in a region that is known as the viscous sub-layer. In order to overcome the invalidity of the standard RANS turbulence models in the viscous sub-layer the idea of the so-called high Reynolds number models is to incorporate an advanced boundary condition model. In these models, the near-wall region is not explicitly resolved with the numerical turbulent model, but is bridged using the so-called wall functions.

Near-wall modelling is clearly critical for this application and hence boundary conditions need to be treated carefully. In line with the implementation described in [47], a thin boundary region of fluid of width y is conceptually excluded from the computational domain, with boundary conditions on the velocity, tangential stress and for k and ϵ applied at the interface of the excluded region. In this work, the normal component of the fluid velocity, $\mathbf{u} \cdot \mathbf{n}$ is set to match that of the moving boundary mesh velocity, $\boldsymbol{V}$, i.e. there is no penetration.

It is further assumed that the tangential component of the stress on the boundary satisfies the relation

$$\mathbf{n}\cdot\boldsymbol{\tau_w} = -\rho_f u_\tau^2 \frac{\mathbf{u}}{\|\mathbf{u}\|} = -\rho_f \frac{u_\tau}{\nu_t}\frac{\mathbf{u}}{y_+}, \qquad \text{where} \qquad u_\tau = \max\left\{C_\mu^{0.25}\sqrt{k}, \frac{\|\mathbf{u}\|}{y_+}\right\}. \tag{3.1}$$

Here $\boldsymbol{\tau_w} = \rho_f \nu \left[\nabla\mathbf{u} + (\nabla\mathbf{u})^T\right]_{z=\eta}$ is the wall shear stress, u_τ is a friction velocity and

$$y_+ = \frac{u_\tau y}{\nu_0}, \tag{3.2}$$

is a non-dimensional wall distance. The applicability of u_τ in (3.1) depends on the criterion that y is chosen at the interface between the viscous sublayer, in which the velocity is assumed to increase linearly away from the wall:

$$\frac{\|\mathbf{u}\|}{u_\tau} = y_+, \tag{3.3}$$

and the logarithmic turbulent boundary layer, in which it is assumed that

$$\frac{\|\mathbf{u}\|}{u_\tau} = \frac{1}{\kappa}\log y_+ + \beta. \tag{3.4}$$

Here $\kappa = 0.41$ is the von Kármán constant and $\beta = 5.2$ is another constant for the case of smooth walls. This criterion is enforced by the ansatz that $y_+ = 11.06$, at the bottom of the logarithmic layer range, $11.06 \le y_+ \le 300$.

Functionally, the constant y_+ implementation of (3.1) acts as a constant coefficient quadratic drag boundary condition applied to the velocity derived from the momentum equation (2.11). The empirically determined law of the wall boundary conditions for k and ϵ at the edge of the computational domain are implemented in a weak form as the Neumann boundary conditions:

$$\mathbf{n} \cdot \nabla k = 0 \qquad \text{and} \qquad \mathbf{n} \cdot \nabla \epsilon = \frac{u_\tau^5}{\sigma_\epsilon \nu_t y_+}. \tag{3.5}$$

3.3 OpenFOAM overview

In order to help in the model verification of the (turbulence modelling) implementation in Fluidity, a benchmark problem has been studied and compared with an independent open-source software package, OpenFOAM [35]. This CFD package achieves the spatial discretisation by using a conventional (cell-centred) Finite Volume Method (FVM) on arbitrary polyhedral meshes (or cells). The temporal discretisation is obtained (from the many available techniques) with a Crank-Nicolson time stepping scheme. The flow solver chosen for the pressure and momentum equations decoupling is the pisoFOAM option which is a transient solver for incompressible flow (but can also be used for steady-state problems) using the PISO algorithm. The pressure-implicit with splitting operators (PISO) is a scheme to simulate the flow in time with a predictor-corrector (i.e. one predictor and two corrector steps) procedure for the pressure calculation on a staggered grid arrangement. To initiate the calculation process a pressure field is taken from the old time level to later get corrected and used to predict the velocity components in the current time level. These velocity components are further used to second-correct the pressure field and final velocity field [105]. The PISO algorithm can be seen as an extension of the semi-implicit method for pressure-linked equations (SIMPLE) solver algorithm with the advantage of allowing faster convergence over SIMPLE, more flexibility (in terms of stability) for irregular cells and no requirement of under-relaxation [42].

In OpenFOAM the wall functions implementation provides a range of Dirichlet or Neummann boundary conditions for the different turbulent quantities involved. The standard types of wall functions used in this benchmarking for high-Reynolds conditions are chosen as:

- `kqRWallFunction` for the turbulent kinetic energy k,
- `epsilonWallFunction` for the turbulent dissipation ϵ, and
- `nutkWallFunction` for the turbulent viscosity ν_t, derived from k depending of the distance of the first cell centre to the wall (i.e. non-dimensional y_+). If the cell centre lies in the viscous sublayer, the results from wall functions approach are very inaccurate [53].

3.4 Benchmark results and discussion

The benchmark geometry is based upon the numerical study performed by Liang et al. [50] and the corresponding two-dimensional (2D) mesh is represented in figure 3.1 with a gap big enough to not completely suppress the vortex shedding behind the circular cylinder (of idealised infinite width). A similar geometry with the only difference being that virtually no separation exists between the bottom of the idealised pipeline (i.e. circular cylinder) and the bed is used in chapter 4 to analyse the effects of scour. The computational mesh is made up of 40000 cells (used here for the hydrodynamic studies), concentrates the mesh density towards the cylinder (with diameter of 0.1 m) surface with a grid size of 0.003. In both numerical models (Fluidity and OpenFOAM) with the same mesh, a uniform boundary layer flow with logarithmic profile inlet velocity in the vertical direction is applied. The flow has a free-stream velocity u_0 resulting in a Reynolds number $Re > 50000$ for the flow parameters used in the numerical experiments (with $\tau^* = 0.098$) in section 4.4 in chapter 4. The side walls (for the extruded OpenFOAM model only), and top surfaces are all set to free slip with a low Froude number to avoid free surface effects, also a zero pressure boundary condition applied at the outlet and a wall function boundary condition is applied in the bottom surface since only the near bed velocity is examined at a small distance above the bottom. At the cylinder surface, the choice of boundary conditions can be specified either as a no-slip or employing a wall function on the surface. It was observed through experimentation that the effect of a no-slip boundary condition underestimates the velocity fluctuations generated by the vortex shedding downstream the cylinder. Therefore, the boundary condition selected for the cylinder surface is also based upon a wall function.

In the benchmark calculations, the surface forces around the circular cylinder are considered as one comparison criterion, these are calculated

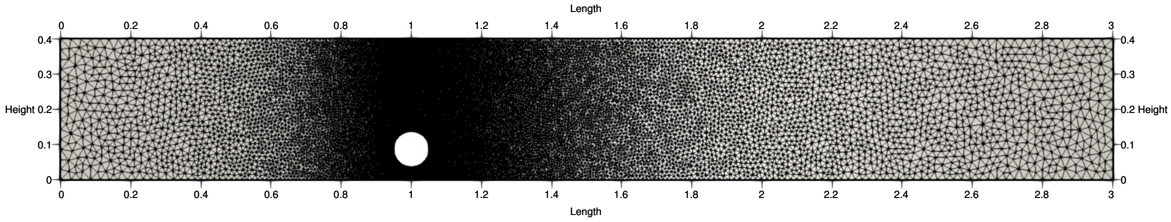

(a) Overall view of the flow domain mesh.

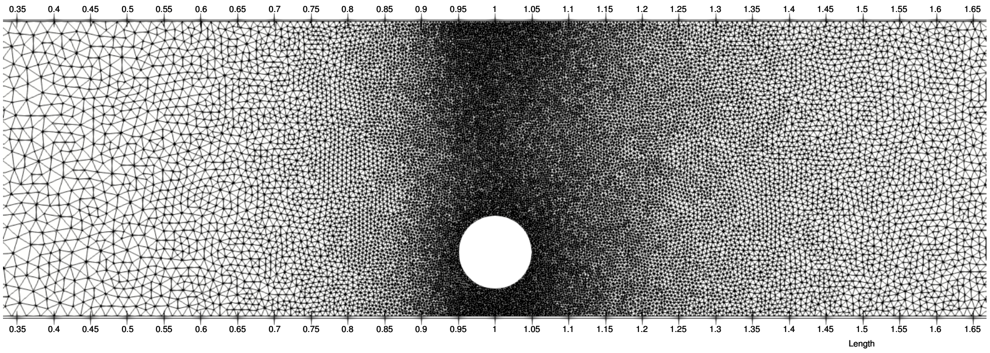

(b) Zoomed mesh into the circular cylinder area.

Figure 3.1: View of the unstructured triangular/tetrahedral mesh employed in the numerical simulation of flow past a circular cylinder used in both Fluidity and OpenFOAM with the circular object positioned at a gap from the bottom boundary.

from the pressure and viscous forces according to,

$$F_D = \int \left(\rho_f \nu \frac{\partial(\mathbf{u} \cdot \mathbf{t})}{\partial \mathbf{n}} \mathbf{n}_y - p\mathbf{n}_x \right) dS, \tag{3.6}$$

and,

$$F_L = -\int \left(\rho_f \nu \frac{\partial(\mathbf{u} \cdot \mathbf{t})}{\partial \mathbf{n}} \mathbf{n}_x - p\mathbf{n}_y \right) dS, \tag{3.7}$$

with the following notations: surface of cylinder S, normal vector x and y components, $\mathbf{n}_x$ and $\mathbf{n}_y$, and tangential velocity, $\mathbf{u} \cdot \mathbf{t}$ on S, where $\mathbf{t} = (\mathbf{n}_y, -\mathbf{n}_x, 0)$.

It is observed from figure 3.2 that the Fluidity model well describes the existence of the wake downstream of the circular cylinder, while the OpenFOAM model underestimates the velocity profile particularly at the upper part of the generated wake. It is also observed more evidently at the inlet region that the effect of the boundary layer formation close to the bed surface is underpredicted as inferred from the velocity magnitude. A plausible explanation for this, coming from the implementation details, may be the use of the wall function boundary conditions on the cylinder and bed surfaces. The k wall function is in both models provided as a Neumann boundary but the ϵ boundary condition in OpenFOAM calculates the actual quantity (i.e. turbulent dissipation rate) as the sum of the value on each face f based on the weights – related to the number

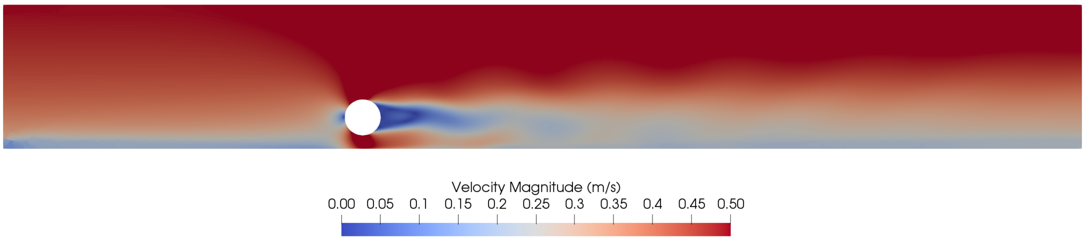

(a) Velocity field in the domain resulting from Fluidity.

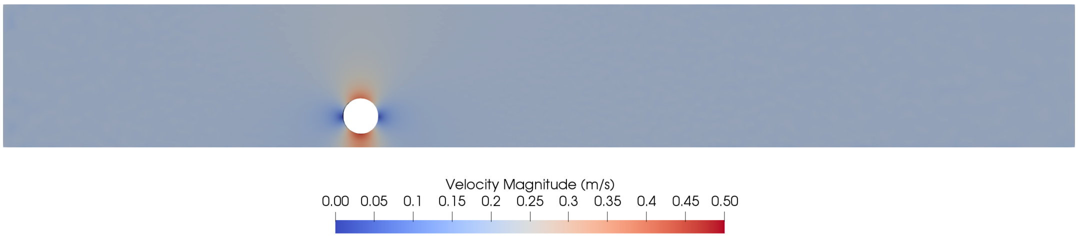

(b) Velocity field in the domain resulting from OpenFOAM.

Figure 3.2: Visualisation of the velocity field magnitude (m/s) after 10 seconds of simulation in Fluidity and OpenFOAM.

of faces,

$$\epsilon = \frac{1}{W} \sum_{f_i}^{W} \left(\frac{C_\mu^{3/4} k^{3/2}}{k y_i} \right), \tag{3.8}$$

where W is the weight of the cell and k is based in the value at the cell center. There is explicitly a requirement that the first cell distance must be calculated and this is connected to a sensitivity of the grid resolution. Therefore, the model using the dissipation rate quantity itself would be grid-dependent.

From figure 3.3, different variations in the velocity profiles over the channel's height (i.e. $y = 0.4m$) are observed at different vertical points along the channel and it is firstly noticed in frames (a) and (b) how the inlet profiles differs between the models (in the OpenFOAM model the effects of the boundary layer near the bedwall are less noticeable). By the time the flow passed the circular cylinder the profiles seem to share more similarities in shape between the models (in frames (c) and (d) just across the cylinder at $x = 1m$ and in frames (e) and (f) further downstream at $x = 1.2m$) but still there is a clear underestimation of the velocity values with the OpenFOAM simulation initialised from the upstream profile.

Also, from figure 3.4, in frames (a) and (b), differences in the bed shear stress magnitude along the channel can be clearly noted. The turbulent quantities (TKE and ϵ) comparisons show a difference of an order of magnitude between models (with lower values for the OpenFOAM results) plus an erratic profile in both quantities with the OpenFOAM simulation.

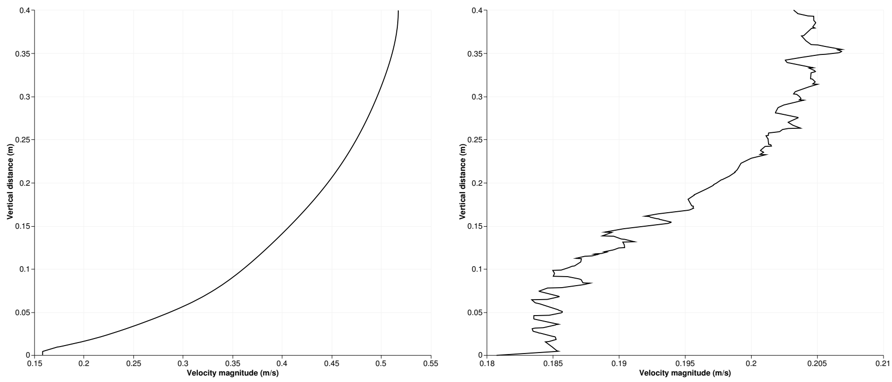

(a) Velocity profile with Fluidity at a distance $x = 0.8m$ along the channel.

(b) Velocity profile with OpenFOAM at a distance $x = 0.8m$ along the channel.

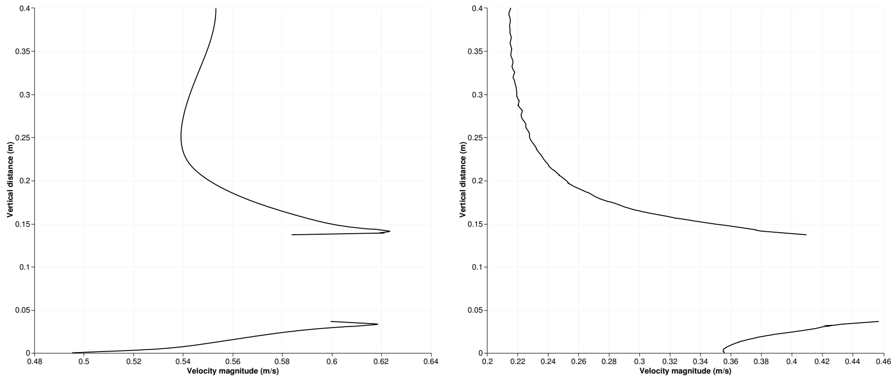

(c) Velocity profile with Fluidity at a distance $x = 1m$ along the channel.

(d) Velocity profile with OpenFOAM at a distance $x = 1m$ along the channel.

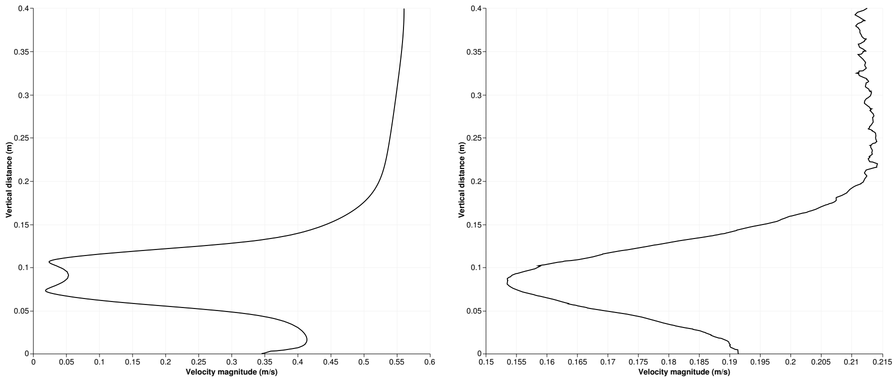

(e) Velocity profile with Fluidity at a distance $x = 1.2m$ along the channel.

(f) Velocity profile with OpenFOAM at a distance $x = 1.2m$ along the channel.

Figure 3.3: Velocity profiles in the numerical simulation of a two-dimensional flow past a circular cylinder.

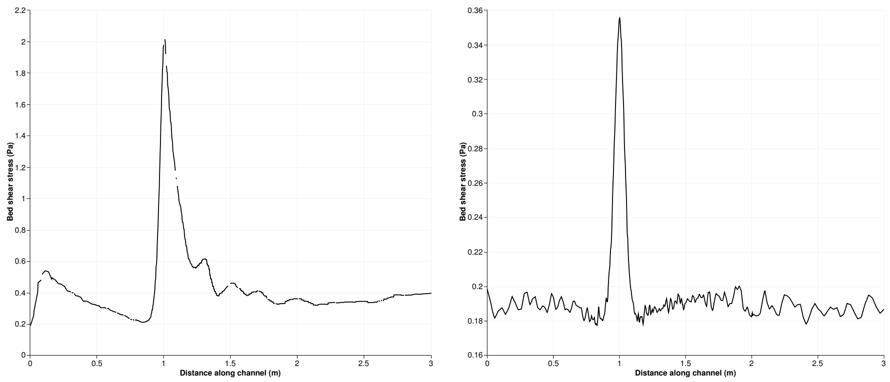

(a) Bed shear stress with Fluidity along the channel.

(b) Bed shear stress with OpenFOAM along the channel.

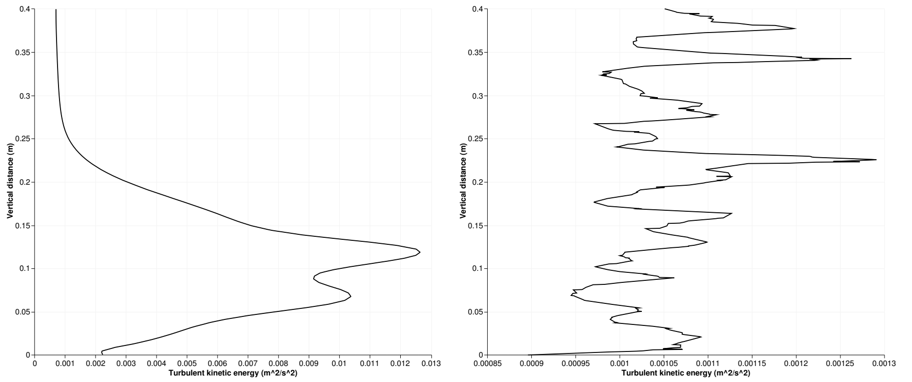

(c) TKE profile with Fluidity at a distance $x = 1.2m$ along the channel.

(d) TKE profile with OpenFOAM at a distance $x = 1.2m$ along the channel.

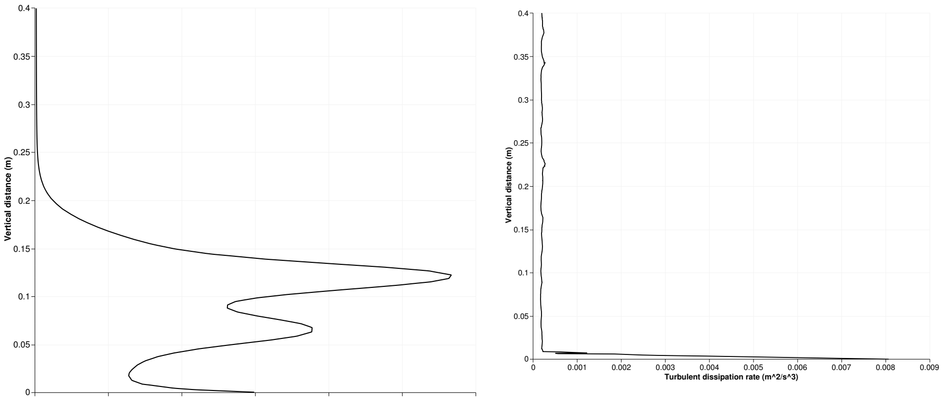

(e) ϵ profile with Fluidity at a distance $x = 1.2m$ along the channel.

(f) ϵ profile with OpenFOAM at a distance $x = 1.2m$ along the channel.

Figure 3.4: Bed shear stresses and turbulent quantities in the numerical simulation of a two-dimensional flow past a circular cylinder.

From figure 3.5, specifically in frame (*c*) it can noted that in regards to the frequency of the oscillations produced in the lift force, although the results from the previous experiments [50] were conducted with a $Re \approx 7000$, intuitively the cycles within a period of non-dimensional time of 10 are very similar to the ones observed in figure 12 from the studies carried out by Liang et al. [50]. This agreement provides confidence that the Fluidity's hydrodynamics model lies in the adequate accuracy range to carry on the intended model verification with the posterior study [51] also used as a benchmark result for the scour results considered in the next chapter 4.

The comparison of the drag and lift forces suggests that OpenFOAM is mishandling the swirling flows in the downstream wake and as a consequence underpredicting the wall shear stresses at the bottom wall/bed surface. The alternative wall function implementation within Fluidity with a (conceptually) excluded (y_+) distance to wall from the computational domain seems to produce favourable results in spite of the level of refinement near the bottom wall and/or the cylinder surface and possibly a mesh dependence issue that the $k - \epsilon$ turbulence modelling may have.

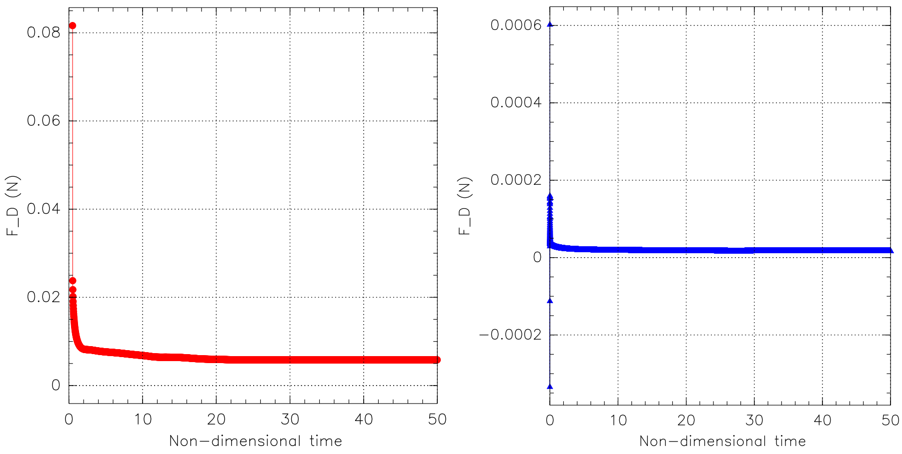

(a) Drag force on the circle versus dimensionless time $t\frac{u_0}{D}$.

(b) Drag force on the circle versus dimensionless time $t\frac{u_0}{D}$.

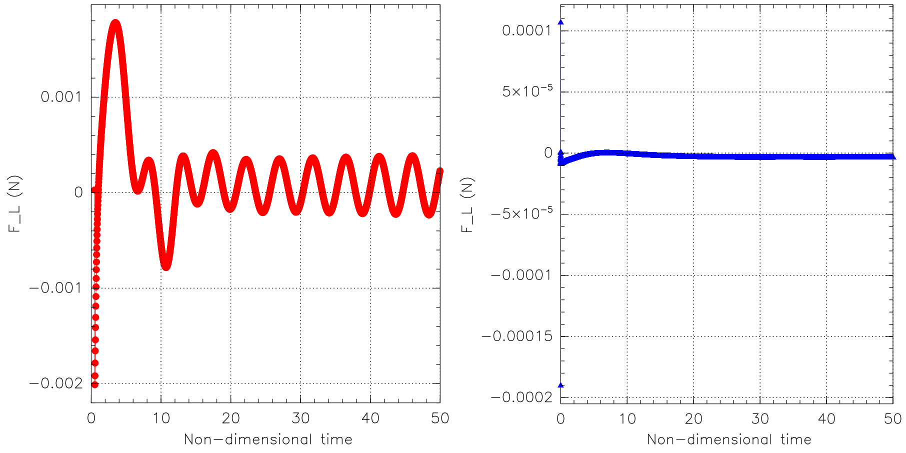

(c) Lift force on the circle versus dimensionless time $t\frac{u_0}{D}$.

(d) Lift force on the circle versus dimensionless time $t\frac{u_0}{D}$.

Figure 3.5: Drag and lift forces on the circle in the numerical simulation of a two-dimensional flow past a circular cylinder using Fluidity (●) and OpenFOAM (▲).

Chapter 4

Local scour around a horizontal pipeline

Contents

This chapter is derived and expanded from the work by J. M Nunez Rattia et al. [77].

4.1 Introduction

In the context of modelling scour around structures using single phase models based in finite volume/element discretisations using unstructured meshes, a full numerical model is proposed coupling the sediment transport module with the turbulent hydrodynamics. The model has been validated by computing the bed changes of the results of the work by Liang et al. [51] in the modelling of scour below pipelines in currents. Amongst the main challenges in the development of this numerical model, is that the evolution of the boundary mesh location in response to bed morphodynamics also requires changes to the internal computational mesh. If this is not done, or is not done well, this can lead to poor quality meshes which compromise simulation stability and accuracy. A widely adopted approach to this problem is to use mesh movement methods to propagate the boundary mesh movement into the domain, in an attempt to maintain mesh quality throughout [51, 111]. However, in the case of extreme bed movement and/or where this movement is close to a fixed structure in the domain (which inevitably constrains the mesh and its ideal movement to some degree), it is very difficult to maintain mesh quality with mesh movement algorithms alone.

With unstructured computational grids, it is relatively straightforward to use variable resolution within the domain, but due to arbitrary connectivity and cell shape it is also arguably more complicated to move the mesh nodes on the bed and in the domain interior. Although the development of moving grid techniques has been generally less well studied than other adaptive mesh techniques, there have been a lot of progress in the past decades, such as partial differential equations (PDE)-based and spring-based analogy methods [9]. From the moving mesh PDE-based approaches, the relatively simple Laplacian smoothing has been a common choice to tackle mesh deformation in response to local sediment scour due to its robustness and ease of implementation with an unstructured grid in a complex domain [55]. As it will be argued in this chapter (4), movement of nodes alone may not be sufficient to maintain an adequate mesh resolution and/or structure, especially for cases with extreme bed deformation.

In this work it is presented a new mesh optimisation/movement (or *hr*-adaptive) framework for computational morphodynamics. This includes the use of relatively sophisticated mesh movement algorithms to account for the bed evolution, while utilising mesh optimisation methods in order to: (i) maintain mesh quality under extreme and complex scenarios; (ii) vary the total degrees of freedom count as the problem complexity evolves; and (iii) help track solution features in the wider domain. The framework will be demonstrated on a complex scour problem with a hydraulic structure (i.e. pipeline) close to the bed; the closeness being particularly challenging due to the constraints the structure imposes on the mesh movement, and the significant difference in degree of freedom count ideally required in the gap between structure and bed as the scour progresses at different times into the simulation. Results are benchmarked against laboratory data and prior numerical studies which also considered the same test case. The work in this chapter represents a significant extension and improvement over a previous paper [78] which reported on the initial steps in this work resulting in a completed publication in a peer-reviewed journal [77].

4.2 Discretisation and numerical solution procedure

This section concentrates on the numerical modelling of the physical processes taking place in the scour area, where the key elements to capture are:

(i) An accurate modelling of the fluid flow taking account the effect of turbulence via a RANS eddy-viscosity two-equation model ($k - \epsilon$).

(ii) The combination of turbulence generation-dissipation action in the wall linked to the bed shear stress and initiating both bedload and suspended sediment transport, hence these processes need to be modelled as well.

(iii) Finally, the resulting mass conservation of sediment, induces a bed profile evolution which needs to be modelled through the incorporation of a mesh movement module plus additional benefits from a mesh adaptivity algorithm.

The discretisation of the equations described in the previous chapter 2 are performed here within the control volume/element-based model, Fluidity [1], upon unstructured two-dimensional (2D) triangular or three-dimensional (3D) tetrahedral computational meshes.

4.2.1 Flow model discretisation

Equation (2.11) has been spatially discretised using a P1$_{DG}$P2 (see figure 4.1) finite element pair in which the velocity field varies linearly over elements (e_i), and may be discontinuous between elements, while pressure has a quadratic variation within and is continuous between elements [19]. In a discontinuous Galerkin (DG) discretisation the shape functions can be selected so that the field variables (and derivatives) are free to be discontinuous between element boundaries [18]. A field that is discretised using a discontinuous function space will have multiple nodal values at element nodes and thus will have more degrees of freedom than a continuous function of the same polynomial order on the same mesh, since these elements do not have repeated nodes. DG methods are locally conservative so they are a popular choice of discretisation for advection-dominated problems as opposed to some continuous Galerkin options such as Petrov-Galerkin-based methods which can lead to excessive numerical diffusion to maintain stability. Also, thanks to their flux representation they perform well on arbitrary meshes and have the convenient properties of producing a block-diagonal mass matrix that can be easily inverted locally for each element, so it does not have to be lumped, thereby resulting in a very efficient computational time.

The use of DG methods for the velocity discretisation requires the choice of flux schemes for both the advective (e.g. an upwind DG formulation is used here) and diffusive (e.g. the Bassi-Rebay scheme in the local discontinuous Galerkin framework [5] is used here) terms. A mathematical description of the discretised momentum equation is given

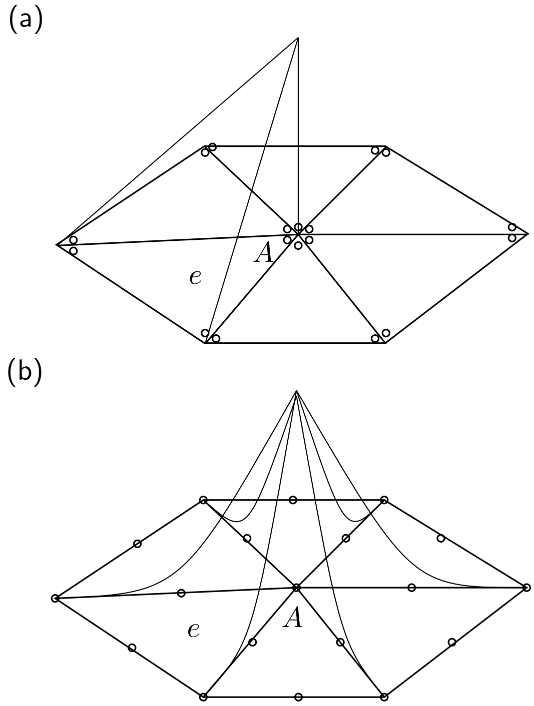

Figure 4.1: Two-dimensional schematics of: (a) piecewise linear discontinuous shape functions and (b) piecewise quadratic continuous shape functions.

in section 4.3.2, where a moving reference frame is assumed. In a discontinuous Galerkin method of degree $p > 0$, it is expected potential numerical oscillations for the advective part of the discretisation. For $\mathrm{P}1_{DG}$ elements, the over and undershoots in the slopes, derived after the spatial reconstruction of the inter-element fluxes, $\hat{u}|_{\Gamma_e}$ (where $\hat{u}$ is the convective flux of a scalar quantity transported by a velocity field through the boundary element, Γ_e) can be controlled in order to make the solution bounded with a slope limiting method (e.g. the vertex-based slope limiter [46] is used here) with the goal of not increasing the total variation of the solution, $TV\left(u\right) = \int \|\nabla u\| d\Gamma_e$ and thus aiding stability and robustness. In the vertex-based limiter, the idea is to bound the admissible slope using the maximum and minimum element values, u_i at each vertex $\mathbf{x}_i$ to be within the bounds of the average value, u_c of each element Ω_e,

$$u_i^{max} = \max\left\{u_c, u_i^{max}\right\}, \quad u_i^{min} = \min\left\{u_c, u_i^{min}\right\}, \tag{4.1}$$

and obtained a constrained solution,

$$u_i\left(\mathbf{x}\right) = u_c + \alpha_e\left(\nabla u\right)_c\left(\mathbf{x}_i - \mathbf{x}_c\right), \tag{4.2}$$

where, $\left(\nabla u\right)_c$ is the local gradient within the element, Ω_e before the slope limiting is applied and α_e is the element-wise correction factor,

$$\min_i = \begin{cases} \min\left\{1, \frac{u_i^{max}-u_c}{u_i-u_c}\right\}, & \text{if} \quad u_i - u_c > 0, \\ 1, & \text{if} \quad u_i - u_c = 0, \\ \min\left\{1, \frac{u_i^{min}-u_c}{u_i-u_c}\right\}, & \text{if} \quad u_i - u_c < 0. \end{cases} \tag{4.3}$$

In solving the incompressible Navier-Stokes equations, the mixed finite element formulation P1$_{DG}$P2 has the desirable property of satisfying the LBB (Ladyzenskaja-Babuska-Brezzi) stability condition and therefore, no need for stabilisation of the pressure field offering at the same time a higher-order accuracy in the pressure solution.

The discretisation of the Navier-Stokes equations in non-conservative form as shown in equations (2.3) and (2.11), assuming a partial stress form which is the preferred form of the viscous term for incompressible flow with spatially varying viscosity. They can be written in matrix form as,

$$-\mathcal{C}^{\mathcal{T}}\mathbf{u}^{n+1} = 0, \tag{4.4}$$

and for the momentum equation,

$$\mathcal{M}\frac{\mathbf{u}^{n+1} - \mathbf{u}^{n}}{\Delta t} + \mathcal{A}\left(\mathbf{u}^{n+\theta_{nl}}\right)\mathbf{u}^{n+\theta} + \mathcal{K}\mathbf{u}^{n+\theta} + \mathcal{C}p^{n+\frac{1}{2}} = \mathcal{B}, \tag{4.5}$$

with matrices,

$-\mathcal{C}^{\mathcal{T}}$,	(Divergence matrix)
$\mathcal{M}$,	(Mass lumped matrix)
$\mathcal{A}$,	(Advection matrix)
$\mathcal{K}$,	(Viscosity matrix)
$\mathcal{C}$,	(Gradient matrix)
$\mathcal{B}$.	(Boussinesq-term matrix)

The procedure used here for solving the discretised matrix system of equations is a pressure correction-based approach,

$$\mathcal{M}\frac{\mathbf{u}_{*} - \mathbf{u}^{n}}{\Delta t} + \mathcal{A}\left(\mathbf{u}^{n+\theta_{nl}}\right){\mathbf{u}_{*}}^{n+\theta} + \mathcal{K}{\mathbf{u}_{*}}^{n+\theta} + \mathcal{C}p_{*} = \mathcal{B}, \tag{4.6}$$

where, p_{*} is the best available guess for pressure and $\mathbf{u}_{*}$ is an intermediate velocity which will hold until the pressure correction is done. This velocity solution does not satisfy the continuity equation (4.4) and thus a second pressure correction step is invoked to update the velocity to be solenoidal (divergence-free) and finally the corrected velocity and updated pressure are obtained [36]. Combining the continuity equation (4.4) with the difference between the systems (4.5) and (4.6), the system is reformulated into a Poisson equation for $\Delta p = p^{n+\frac{1}{2}} - p_*$

$$\mathcal{C}^T \mathcal{M}^{-1} \mathcal{C} \Delta p = \frac{\mathcal{C}^T \mathbf{u}_* - \mathcal{M}_{bc}}{\Delta t}, \tag{4.7}$$

where, $\mathcal{M}_{bc}$ accounts for the boundary conditions prescribed for the velocity. Finally, after satisfying the continuity equation, the pressure, $p^{n+\frac{1}{2}}$ after correction can be updated,

$$p^{n+\frac{1}{2}} = p_* + \Delta p, \tag{4.8}$$

and for the velocity,

$$\mathbf{u}^{n+1} = \mathbf{u}_* - \Delta t \mathcal{M}^{-1} \mathcal{C} \Delta p. \tag{4.9}$$

The nonlinear advection term in the momentum equation (2.11) is dealt with using two Picard iterations to ensure that only linear matrix systems need to be solved. In each iteration, first the momentum equation is linearised with a nonlinear relaxation parameter, $\theta_{nl} = [0, 1]$ such as $\mathbf{u}^{n+\theta_{nl}} = \theta_{nl} \bar{\mathbf{u}}^{n+1} + (1 - \theta_{nl}) \mathbf{u}^n$, where $\bar{\mathbf{u}}^{n+1}$ is the current best guess of $\mathbf{u}^{n+1}$ possibly after calculating the pressure correction.

In regards to the temporal discretisation, the θ-scheme, time marching algorithm employed here for the momentum equations takes an operator-splitting approach in which the diffusive term is solved using an implicit, second-order accurate in time, Crank-Nicolson scheme with an adaptive timestep chosen automatically such that the maximum Courant number over the mesh is always below a user defined value (in this work a value 2 is used), while the advective term is solved using an explicit forward Euler scheme with a subcycled timestep chosen such that the maximum Courant number for the subcycling is below another user defined value (tighter that the rest of the model, here 0.2 is used).

4.2.2 Turbulence model discretisation

Equations (2.14) and (2.15) are spatially discretised using a flux-limited, control volume-based method [1, 83] with a characteristic element topology as represented in figure 4.2. A vertex-centred approach on the finite element mesh is employed, with the control volumes around each vertex defined by the dual mesh. This dual tessellation alternative can be used to define a volume or dual element around each vertex which can be constructed by joining the midpoints of element edges with the centroids of the neighbouring elements, in two dimensions while the face centroids are introduced in three dimensions. As mentioned with DG discretisations, the choice of flux schemes across volume facets is necessary for the control volume method. For the discretisation of the advective part of the $\kappa - \epsilon$ transport equations, a finite element interpolation of the basis functions on the parent mesh into the dual mesh is used which normally is unstable (in the sense of boundedness) and requires limiting. To ensure boundedness and affectively suppress spurious oscillation while maintaining high-order approximations of the solution, a Sweby limiter

[97] (mostly popular slope limiting technique for finite difference/volume methods) is used to limit the face values of the fluxes across control volume boundaries in each element. The control volume diffusion is also performed with the finite element interpolation calculating the gradient of the field constructed using the basis functions of the parent finite element mesh to form the divergence.

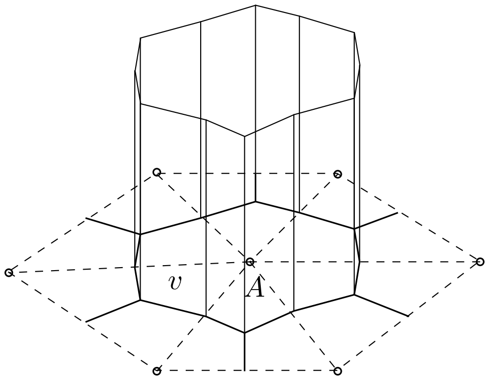

Figure 4.2: Two-dimensional schematic of piecewise constant control volume shape functions (has value 1 at node A descending to 0 at the control volume boundaries) and dual mesh based on parent linear finite element mesh.

The $\kappa - \epsilon$ equations are resolved by firstly decoupling and linearising each equation. Two discretisations are used for κ and ϵ and the linear matrix system is solved using the best available values from previous nonlinear Picard iterations (generally two iterations are found to be a good compromise between accuracy and efficiency) similarly to the nonlinear relaxation for the velocity value, with a parameter $\theta_{\kappa\epsilon} = [0, 1]$.

For control volume temporal discretisations, an advection subcycling based upon an requested Courant number (i.e. 2, selected in this work) is also available, although in this case the θ-scheme value (i.e. 1 for a fully implicit) is applied globally without advection/diffusion splitting.

4.2.3 Sediment transport model discretisation

The numerical treatment of the sediment transport model involves a two-step approach in which the results of the suspended sediment (concentration) equation (2.21) are precomputed in the domain and served as an input for the Exner equation (2.17) describing the boundary deformation over an $(N-1)$-dimensional space corresponding to the boundary of the N-dimensional space the flow is computed over. The following notation Ω_{surf} for this $(N-1)$-dimensional space, formed by projecting out the vertical dimension, and Γ_{surf} for its boundary is used. The discretisation procedure used for the sediment volume fraction advection-diffusion equation (2.21) in this work is very similar to that (i.e. control volume discretisation) already described for the two scalar transport equations in the turbulence model in the previous section 4.2.2. This matrix equations takes the form

$$\mathcal{M}\frac{c^{n+1}-c^{n}}{\Delta t}+\mathcal{A}_s\left(\mathbf{u}^{n+\theta_{nl}},u_{si}\right)c^{n+\theta}+\mathcal{K}_s c^{n+\theta}=0, \tag{4.10}$$

where, $\mathcal{A}_s\left(\mathbf{u}^{n+\theta_{nl}},u_{si}\right)$ is the sediment advection matrix, which is a function of the velocity and the particle settling velocity and $\mathcal{K}_s$ is the sediment diffusion matrix. For more details of a practical application (e.g. turbidity currents) of the discretised mathematical model for suspended sediment refer to [81].

As defined by (2.17), the bed level update is dependent on $\nabla_{\text{surf}}\cdot\mathbf{q_b}$, the surface divergence of the bedload flux, and the erosion and deposition of sediment at the bed boundary. For uniform, steady-state flow and sediment particles of moderate diameter, the variation of $\eta(x, y, t)$ is governed partially by the sediment exchange with the bed-material, but mainly through the divergence of the bedload transport. Considering the contributions of the bedload transport only and assuming $n = 0$, the relevant portion of the sediment mass balance or Exner equation (2.17) can be written in the form

$$\frac{\partial \eta}{\partial t} + \nabla_{\text{surf}} \cdot \mathbf{q_b} = 0. \tag{4.11}$$

This equation provides the rate of bed level change, with the implementation here utilising a Galerkin finite element-based discretisation over the bed surface domain, Ω_{surf} with a bed surface boundary, Γ_{surf} and using linear trial basis functions equal to test functions and denoted by Ψ_i, for every degree of freedom indexed by i. The weak formulation of this problem then takes the form,

$$\begin{gathered} M_{ij}\frac{\partial \eta_j}{\partial t} = \int_{\Omega_{\text{surf}}} \Psi_i \Psi_j \, \frac{\partial \eta_j}{\partial t} \, d\Omega_{\text{surf}} = \\ -\left[\int_{\Omega_{\text{surf}}} \mathbf{q_b} \cdot \nabla \Psi_i \, d\Omega_{\text{surf}} + \int_{\Sigma_{\text{surf}}} \mathbf{q_b} \Psi_i \cdot \mathbf{n} \, d\Gamma_{\text{surf}} \right]. \end{gathered} \tag{4.12}$$

The literature shows that unrealistic bed profiles can be generated due to numerical instabilities arising from the nonlinear coupling of the flow field and the bed level update (e.g. [2, 8, 51]). Some studies [44] have also illustrated stability issues with the Exner equation due to its intrinsic nonlinear hyperbolic nature as shown in equation (4.11) and concluded that measures need to be taken to avoid numerical instabilities which often manifest at the grid scale through surface wiggles or sawtooth patterns as the surface boundary moves or deforms. One approach to deal with this issue is to add a regularisation term in the matrix-based finite element construction, acting as a diffusion-like filter with a length parameter that can be related to the grid size. This results in the slightly modified *mass matrix*

$$M_{ij} = \int_{\Omega_{\mathrm{surf}}} \Big[\big(\Psi_i \Psi_j\big) + \lambda^2 \left(\nabla_{\mathrm{surf}} \Psi_i \cdot \nabla_{\mathrm{surf}} \Psi_j\right) \Big] \, d\Omega_{\mathrm{surf}}, \tag{4.13}$$

where λ is a smoothing length scale, in this work chosen to be twice the length of a typical line segment on the bed boundary. This implementation effectively smooths the bedload transport source term in the Exner equation. This is in contrast to other filtering approaches which explicitly smooth the bed coordinate η itself, introducing a spurious restoring force and potentially mass conservation issues.

The moving boundary (here the bed) is computed by updating the vertical position of the vertices making up the bottom boundary at each timestep. First, the flow field model is calculated by solving the Navier-Stokes equations with the turbulence model. Then the obtained flow parameters, including the bed/wall shear stress, are employed to solve the bedload and suspended load models allowing a derivation of the boundary displacement or mesh velocity, $\boldsymbol{V}$ at the water-sediment interface,

$$\boldsymbol{V} = \left(0, 0, \frac{\partial \eta}{\partial t}\right), \qquad \text{on} \qquad z = \eta. \tag{4.14}$$

This in turn triggers a mesh movement algorithm which is applied at every timestep and hence acts continuously, combined with a mesh optimisation step invoked every user-defined number of timesteps (here 15 is used). Both of these mesh update algorithms are described in the following section 4.3. A summary of a full time loop is included in figure 4.3.

The diagnostic algorithms for the calculation of the bedload divergence, $div(\mathbf{q_b})$ and the net suspended load, $(E - D)$ fluxes required to access the mesh velocity are condensed in the pseudo-code procedure presented in Algorithm 1.

Due to the difference in time scales governing the hydrodynamics and bed changes, it is standard practice in computational morphodynamics to use a morphological acceleration factor to reduce computational costs. This can be thought of as defining a morphodynamic timestep which is much longer than the flow timestep (often by a factor of 10 to 1000) [51, 55]. A morphological acceleration factor (obtained through trial and error in order to control the morphology computation) of 10 is generally used in the early stages of the simulations performed here where bed changes are more rapid, and up to 60 at later stages where changes are more gradual.

4.3 Mesh adaptivity and parallelisation

4.3.1 Mesh optimisation/h-adaptivity

The primary objective motivating the use of anisotropic mesh optimisation in this study is to maintain optimal spatial resolution (by which

Algorithm 1 Mesh velocity algorithm

```
procedure GridVelocity
    $bss \leftarrow$ bed shear stress computed from the hydrodynamics.
    $nodes \leftarrow$ node count of N-dimensional mesh.
    $surfnodes \leftarrow$ node count of (N-1)-dimensional mesh.
    $faces \leftarrow$ face count of (N-1)-dimensional mesh.
    $i, j \leftarrow$ count of array.
$div(\mathbf{q_b})$:
    if $(N-1) \in N$ then:
        for $j \leftarrow surfnodes$ do
            $\mathbf{q_b} \leftarrow \mathbf{q_b}(bss.node\_val(j))$.
            for $i \leftarrow faces$ do
                $div(\mathbf{q_b}) \leftarrow \mathbf{q_b}\Psi_i.face\_val\_at\_quad(i)$.
            end for
            $div(\mathbf{q_b}) \leftarrow \mathbf{q_b}\nabla\Psi_j.node\_val(j)$.
        end for
    end if
$(E-D)$:
    for $j \leftarrow nodes$ do
        $c_j^{n+1} \leftarrow$ derived from equation (4.10).
    end for
    if $(N-1) \in N$ then:
        for $j \leftarrow surfnodes$ do
            for $i \leftarrow faces$ do
                $D \leftarrow D(c_i.face\_val\_at\_quad(i))$.
                $E \leftarrow E(c_i.face\_val\_at\_quad(i))$.
            end for
        end for
    end if
$loop$:
    for $j \leftarrow nodes$ do
        $div(\mathbf{q_b}) \leftarrow div(\mathbf{q_b}).node\_val(j)$.
        $(E-D) \leftarrow (E-D).node\_val(j)$.
        $\boldsymbol{V} \leftarrow [0, 0, -(div(\mathbf{q_b}) + (E-D))]$.
    end for
end procedure
```

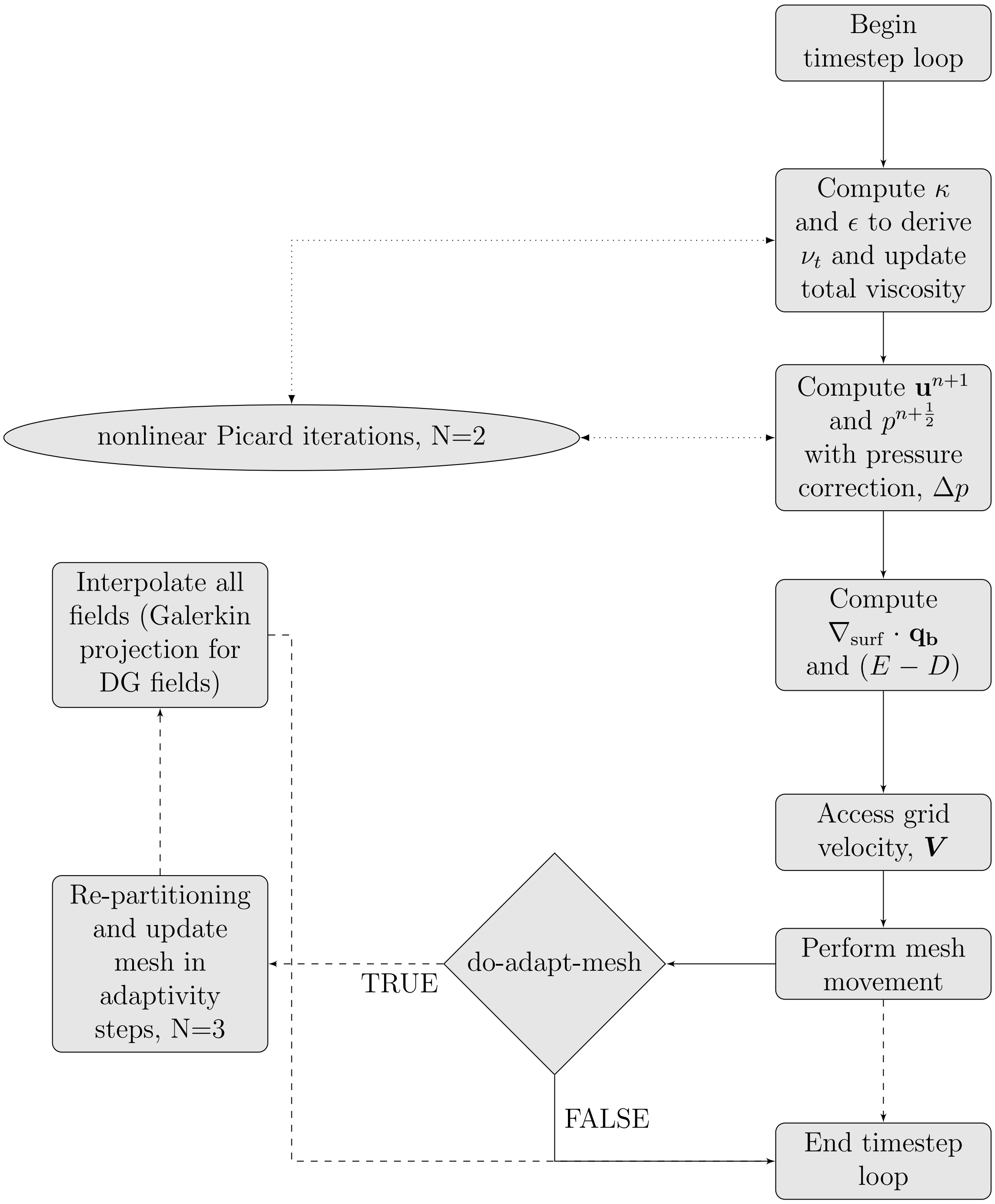

Figure 4.3: A flowchart of the high-level procedures involved in the hydrodynamics and sediment morphodynamic internal coupling.

is meant both the shape and size of elements) under external boundary deformation and the associated internal mesh movement with time, so optimal elements in physical space (K) comply with equilateral elements in an isotropic computational space ($\hat{K}$) under a coordinate transform mapping, $T_K : \hat{K} \rightarrow K$ [84]. Finite element adaptivity can be in element size, h, element position, r, or in the polynomial order of the representation, p. This last (i.e. p) adaptivity is not implemented here. Probably the most widely used form of mesh adaptivity is the approach referred to as h-adaptivity or mesh optimisation. This involves choosing a coarse starting mesh and estimating the error over each of the simplices. Those elements for which the estimated error is unacceptably large are subdivided into smaller ones and the process is then repeated using a new error estimate on this new anisotropic mesh. For example, in two dimensions it is conventional to subdivide each triangle that is being refine into at least two children inserting a node at the center of an edge creating new surrounding elements (i.e. edge splitting, amongst other operations). An application of mesh optimisation is relatively costly (perhaps equivalent to several timesteps of the underlying solver, and being dependent on choices over interpolation scheme etc.) and so is generally applied perhaps only every 10–20 timesteps. This is perfectly acceptable here since mesh movement is used every timestep and thus is continuously seeking to maintain a good quality mesh in response to boundary deformation.

Ignoring load balancing and parallelisation which will be discussed later, the application of mesh optimisation can be divided into three steps. The first is to decide what mesh is desired via the generation and use of an appropriate error metric; the second is to actually generate the newly adapted mesh through a series of topological operations applied to the current mesh; and the third is to transfer (or interpolate) all necessary data from the previous mesh to the newly adapted one in order to continue the simulation.

In the first step, to drive mesh optimisation, Fluidity makes use of an explicit Hessian-based approach motivated by interpolation error theory [28]. This gradient-based adaptation approach utilises local error estimates based on the second gradient, or Hessian $\mathcal{H}$, of one or more scalar flow variables at some points within the flow domain to drive the adaptation process. For finite element methods (with piecewise linear discretisations) the computational error is bounded by the local interpolation error which can be bounded with the second derivative of the variable u at any point of an element (i.e. linear simplexes) K [14],

$$\|u - \Pi_h u\| \leq C \max_{\mathbf{v} \in E_K} \left\{ \mathbf{v}^T |\mathcal{H}_u| \mathbf{v} \right\}, \tag{4.15}$$

where, Π_h is the $P1$ interpolation operator, $\| \cdot \|$ is a norm acceptable for error control (e.g. L^∞ norm), $\mathbf{v}$ is a vector of edges, E_K is the set of edges of K and C is an $\mathcal{O}(1)$ constant independent of the current mesh and related to the space dimension ($\mathbb{R}^2$ or $\mathbb{R}^3$). $\mathcal{H}_u$ is the Hessian of the scalar field u, and the notation $|\mathcal{H}_u|$ indicates that the absolute values of its eigenvalues have been taken (as we are simply interested in the magnitude of errors here). This previous expression (4.15) reflects that the estimation of the error can be interpreted as the length of the vector measured by the Hessian and this controls the error over a mesh edge v_i

(part of the vector of edges $\mathbf{v}$).

Hessian-based anisotropic adaptation aims to produce simplex meshes with arbitrarily-oriented shapes following a metric-based stretching. The metric tensor is derived from the Hessian by considering its absolute value and decomposition, $|\mathcal{H}_u| = \mathcal{R}^T|\Lambda|\mathcal{R}$, where $\mathcal{R}$ are the eigenvectors (giving the direction of the stretching) of the Hessian and $|\Lambda|$ is the matrix composed by the absolute values of the eigenvalues (giving the magnitude of the stretching) of $\mathcal{H}_u$. Several methods are proposed in the literature to compute the Hessian of discrete scalar variables [12]. In Fluidity, a Galerkin projection procedure [79] is used to obtain the Hessian by recovering the gradient of the solution first and then repeat it with second variational gradient recovery, making use of lumping mass matrices. These projections come from standard finite element computation following the identity,

$$\int_\Omega \Phi_i \mathcal{H}_{ij} d\Omega = \int_\Omega \nabla\Phi_i \nabla u_h d\Omega \quad \forall i. \tag{4.16}$$

The metric tensor formed from the recovered Hessian is, in the simplest way, obtained by taking the absolute value of the Hessian as described above, that is,

$$\mathcal{M} = \frac{C}{\epsilon}|\mathcal{H}_u| = \frac{C}{\epsilon}\mathcal{R}^T|\Lambda|\mathcal{R} \tag{4.17}$$

with $|\Lambda| = \begin{pmatrix} |\lambda_1| & 0 & 0 \\ 0 & |\lambda_2| & 0 \\ 0 & 0 & |\lambda_3| \end{pmatrix}$ in $\mathbb{R}^3$.

This decomposition is unique and provides an explicit bound for the interpolation error [58]. Other authors have proposed different metric tensor (for anisotropic mesh generation) formulations where the optimal mesh error is controlled by another norm, e.g. L^p norm [59]

$$\mathcal{M}_{L^p} = \frac{1}{\epsilon_u} \det\left(|\mathcal{H}_u|\right)^{\frac{-1}{2p+n}} |\mathcal{H}_u|, \tag{4.18}$$

where, n is is the spatial dimension of the current mesh. The inclusion of the determinant of the Hessian as an extra scaling factor results in smaller spatial scales being given more weight in the metric and as a result are better resolved [60]. The use of a $p = 2$ norm in this work was found to show effective results in boundary layer simulations. In regards to the already known interpolation error bound, ϵ it is prescribed as a user-defined weight which controls how strongly the mesh adaptivity is guided by an individual field (variable) – a smaller value leading to a stronger weighting and overall a finer mesh. Also, the metric tensor can be calculated for separate fields, f_i, to be adapted to,

$$\mathcal{M}_i = \frac{C}{\epsilon_{f_i}} |\mathcal{H}\left(f_i\right)|. \tag{4.19}$$

For example, for two metrics derived from two variables, $\mathcal{M}_1$ and $\mathcal{M}_2$, an intersection $\mathcal{M}_1 \cap \mathcal{M}_2$ can be defined such that the maximum interpolation error is minimised for all variables [14, 79]. In this work, the velocity components only are chosen to represent the physics (boundary layers near wall surfaces) that will drive the adaptation.

Once the metric formed from the solution fields is constructed, it can be useful to apply additional constraints to the mesh elements such as imposing minimum ($h_{\min}$) and maximum ($h_{\max}$) edge lengths in order to avoid uncontrolled mesh behaviour (e.g. limiting the production of elements larger than the solution domain or smaller than a certain problem scale). This is represented by a modification of the eigenvalues as,

$$\lambda_i = \min\left(\max\left(|\lambda_i|, \frac{1}{h_{max}^2}\right)\frac{1}{h_{min}^2}\right). \tag{4.20}$$

Other bounds such as maximum allowable element aspect ratios, maximum number of elements and gradation over the rate of element size variation can also be introduced [1].

Once the final error metric tensor has been computed it can be used to measure the edge lengths of the elements in the mesh, $\mathbf{v}$, with respect to the metric field via:

$$\|\mathbf{v}\|_{\mathcal{M}} = \left(\mathbf{v}^T\mathcal{M}\mathbf{v}\right)^{1/2}. \tag{4.21}$$

Mesh metric-based adaptation seeks to equidistribute errors such that local mesh modifications (described in the second step below) are performed aiming at creating a unit mesh, $\|\mathbf{v}\|_{\mathcal{M}} = 1$ for all edges, i.e. all elements in metric space are equilateral and of unit size therefore, anisotropic meshes might be seen as isotropic with respect to a different metric. Since the metric tensor is originally formulated from the Hessian matrices of individual fields, achieving this goal has the effect of generating (anisotropic) elements in physical space which have small edge lengths in directions and locations where the second derivative of the field is large, and are large in directions and locations where the field is near linear [84].

The second step involves achieving the goal of constructing a near equilateral and unit sized mesh in metric space (derived from the previous step) using a Delaunay-type mesh generator [86]. The mesh generation procedure will iteratively compute the lengths of the mesh edge based on the specified discrete metric tensor at each mesh vertex of the current mesh considering that they were defined to satisfied that the adapted mesh is then a unit mesh.

Additionally, a mesh quality objective functional is commonly formed (accounting for both, shape and size functions of the elements) and based on how well the elements of the mesh satisfy $\|\mathbf{v}\|_{\mathcal{M}} = 1$ for all their edges which can be seen an a criterion to decide which of the mesh optimisation operations (described below) should be used to improve the quality of the mesh. In this work, a two-dimensional functional is used [83],

$$Q_{\mathcal{M}} = 12\sqrt{3}\frac{|\Delta|_{\mathcal{M}}}{|\partial\Delta|^2_{\mathcal{M}}} F\left(\frac{|\partial\Delta|_{\mathcal{M}}}{3}\right), \quad \text{with}, \tag{4.22}$$

$$F(x) = \left[\min\left(x, \frac{1}{x}\right)\left(2 - \min\left(x, \frac{1}{x}\right)\right)\right]^3,$$

where, $|\Delta|$ represents the area of the element Δ and $|\partial\Delta|$ its perimeter, both measured in the metric $\mathcal{M}$. A series of topological operations are then applied to the current mesh to minimise this mesh quality functional based on different techniques and algorithms for construction of an adapted conformal triangulation, $\mathcal{T}^h_{k+1}$. The overall mesh optimisation algorithm constructs a sequence of meshes through local element modification, $\mathcal{T}^h_0, \dots \mathcal{T}^h_{k+l}, \dots \mathcal{T}^h_{k+1}$, where l are the number of local modifications, so that the quality functional is minimised throughout the whole mesh, $Q_{\mathcal{T}} = \min \{Q_K, K \in \mathcal{T}\}$. In this work, the two-dimensional library ani2d [104] (`http://ani2d.sourceforge.net/`) is used to formulate the mesh quality functional and perform the mesh operations. These operations include: (i) node creation or edge splitting, (ii) node deletion or edge collapsing, (iii) diagonal swapping common edges between two elements. Note that in three dimensions more operations are possible (e.g. edge to edge, edge to face, and face to edge swapping) [85].

The third and final step involves transferring field data from the old mesh to the new mesh in an interpolation process. The simplest option to transfer data is called consistent interpolation which simply involves evaluating the finite element solution (by basis functions) on the old mesh at the nodal locations defining the fields on the new (adapted) mesh. This is is a trivial way for any finite element method to regenerate data on the new mesh, but it is non-conservative and is unsuited to discontinuous function spaces such as is used here to represent the velocity field. These issues may be overcomed using a conservative Galerkin projection interpolation scheme to map solution fields between meshes. Solving the finite element discretisation of the optimal interpolant in the L^2 norm between finite element spaces equation must satisfy the orthogonality condition, $\langle \boldsymbol{u} - \boldsymbol{u}^P, \Psi_i \rangle = 0$, where, $\boldsymbol{u}$ is the approximated solution in the parent finite-dimensional space and $\boldsymbol{u}^P$, is the orthogonal projection of $\boldsymbol{u}$ onto the target finite-dimensional space. Solving this equation requires the computing of the integrals of the inner products of the basis functions of the two meshes, parent, $\mathcal{T}^{\Phi}$ and target, $\mathcal{T}^{\Psi}$. To efficiently compute this integral associated equation in an exact manner, a supermeshing algorithm (constructed from the union of the nodes of the elements from the old/parent/donor – $K \in \mathcal{T}^{\Phi}$ mesh and the new/adapted/target mesh – $\hat{K} \in \mathcal{T}^{\Psi}$) is used in Fluidity [26, 25]. This algorithm makes uses of a constrained Delauney triangulation (CDT) procedure plus other intersection algorithms for the construction of an extra mesh, $K \cup \hat{K}$ in which for the intersection, $K \cap \hat{K}$ where if two elements do intersect, then the inner product of the basis function in particular, the mixed product $\Phi_{K_j}\Psi_{\hat{K}_i}$ must only be non-zero over the region of intersection and subsequently added to the computation of the projection matrix P, $M\boldsymbol{u}^P = P\boldsymbol{u}$, where, M is the mass matrix commonly appearing in finite element methods. Additional advantage of this interpolation scheme is that it could be parallelised.

4.3.2 Mesh movement/r-adaptivity

In a fundamentally different manner to mesh optimisation, mesh movement or r-adaptivity methods locally redistribute the physical locations of vertices of the mesh while maintaining its structural connectivity. In this work this is performed continuously over the course of every timestep and thus the underlying discretisation is formulated within an arbitrary lagrangian-eulerian (ALE) framework [21]. This process is purely geometrical, keeping a regularised computational mesh during the whole calculation, avoiding excessive distortions and resisting mesh elements becoming squeezed or entangled. These methods locally improve the quality of patches of elements rather than constructing of an optimal mesh in a transformed space such that the adapted mesh equidistributes a measure of error as with mesh optimisation procedures, such as h-adaptivity.

In the Fluidity implementation of mesh movement, this requires that for each simulation timestep, $t^n \rightarrow t^{n+1}$, a continuous, piecewise linear vector field, or mesh velocity, $\boldsymbol{V}$, is specified whose action defines the rate of change of the vertices of the elements such that the physical coordinate, $\boldsymbol{x}_i$, of the ith mesh vertex varies as $\boldsymbol{x}_i(t) = \boldsymbol{x}_i(t^n) + (t - t^n)\boldsymbol{V}_i$, with the physical motion of the rest of the mesh following via linearity of the coordinate field. The mesh velocity modifies the convective fluxes in the moving reference frame for the continuity, momentum and sediment concentration equations as per the ALE formulation. This implicitly defines a (fixed) mesh coordinate, $\boldsymbol{\chi} = \boldsymbol{x}(t^{n+\theta})$, on which the finite element equations are constructed. The time derivative in the inertial terms in the PDEs describing the evolution of the prognostic variables then transform as

$$\left.\frac{\partial a}{\partial t}\right|_{\boldsymbol{\chi}} = \left.\frac{\partial a}{\partial t}\right|_{\boldsymbol{x}} + \sum_i \left.\frac{dx_i}{dt}\right|_{\boldsymbol{\chi}} \frac{\partial a}{\partial x_i} = \left.\frac{\partial a}{\partial t}\right|_{\boldsymbol{x}} + \boldsymbol{V} \cdot \nabla_{\boldsymbol{x}} a. \tag{4.23}$$

For the momentum equation, application of integration by parts, the Crank–Nicolson timestepping, the Bassi–Rebay diffusion operator and choice of an upwinded numerical flux gives a weak form in Ω being a bounded open domain with boundary Γ representing the general Dirichlet (Γ_D)–Neumann (Γ_N) problem; using tests functions $\boldsymbol{w}$ and $\boldsymbol{\tau}$, respectively, integrating over an element e,

$$
\begin{aligned}
\sum_e \int_{\Omega^{(e)}} \boldsymbol{w} \cdot \frac{\mathbf{u}^{n+1} - \mathbf{u}^n}{\Delta t} - \nabla_{\boldsymbol{x}} \cdot (\mathbf{u}_* \boldsymbol{w}) \cdot \left(\frac{1}{2}\mathbf{u}^{n+1} + \frac{1}{2}\mathbf{u}^n - \boldsymbol{V} \right) dV_{\boldsymbol{\chi}} \\
+ \int_{\Omega^{(e)}} \nabla_{\boldsymbol{x}} \boldsymbol{w} : \underline{\boldsymbol{\sigma}}^{n+\frac{1}{2}} + \nabla_{\boldsymbol{x}} \cdot \boldsymbol{w} p^{n+\frac{1}{2}} \, dV_{\boldsymbol{\chi}} \\
+ \oint_{\Gamma_I^e} \boldsymbol{w} \cdot \left\{ \left\{ \frac{\mathbf{u}^{n+1} + \mathbf{u}^n}{2} \right\} \right\} \mathbf{u}_* \cdot \mathcal{J}^{-1} \cdot \boldsymbol{n}_{\boldsymbol{x}} + \overline{\boldsymbol{w}} \cdot \overline{\underline{\boldsymbol{\sigma}} \cdot \mathcal{J}^{-1}} \cdot \boldsymbol{n}_{\boldsymbol{x}} + dS_{\boldsymbol{\chi}} \\
+ \oint_{\Gamma_D^e} \mathbf{u}_D \cdot \boldsymbol{w} \mathbf{u}_D \cdot \mathcal{J}^{-1} \cdot \boldsymbol{n}_{\boldsymbol{x}} dS_{\boldsymbol{\chi}} - \oint_{\Gamma_N^e} \mathbf{u} \cdot \boldsymbol{w} \mathbf{u}_* \cdot \mathcal{J}^{-1} \cdot \boldsymbol{n}_{\boldsymbol{x}} + \boldsymbol{w} \cdot \underline{\boldsymbol{\sigma}} dS_{\boldsymbol{\chi}} = 0,
\end{aligned}
\tag{4.24}
$$

where $\mathbf{u}_*$ is the advective velocity guess from the Picard iteration, projected onto a continuous P1 space, and $\underline{\boldsymbol{\sigma}}$ is the P1$_{DG}$ Bassi–Rebay auxiliary stress term satisfying a local finite element equation

$$
\begin{aligned}
\int_{\Omega^e} \boldsymbol{\tau} : \underline{\boldsymbol{\sigma}} dV_{\boldsymbol{\chi}} = \oint (\nu + \nu_t) \, \boldsymbol{\tau} : (\overline{\mathbf{u}} \boldsymbol{n} + \boldsymbol{n} \overline{\mathbf{u}}) \, dS_{\boldsymbol{\chi}} \\
- \int (\nu + \nu_t) \, \mathbf{u} \nabla \cdot \boldsymbol{\tau} + (\nu + \nu_t) \, (\nabla \cdot \boldsymbol{\tau})^T \, \mathbf{u} dV_{\boldsymbol{\chi}}.
\end{aligned}
\tag{4.25}
$$

Interfacial averaging and upwinding operators in the interior faces subset Γ_I, are defined as

$$
\overline{\boldsymbol{a}} = \frac{1}{2}\left(\boldsymbol{a}^- + \boldsymbol{a}^+\right), \quad \{\{\boldsymbol{a}\}\} = \frac{1}{2}\left(\boldsymbol{a}^- + \boldsymbol{a}^+\right) - \frac{\mathbf{u}_* \cdot \boldsymbol{n}}{2\|\mathbf{u}_* \cdot \boldsymbol{n}\|}\left(\boldsymbol{a}^- - \boldsymbol{a}^+\right),
$$

where a^+ is the value of a variable in the eth element and a^- is the value from the element across the interface. Finally, $\mathcal{J}_{ij} = \frac{\partial x_i}{\partial \chi_j}$ is the Jacobian matrix of the moving mesh transformation at the time level the gradient operator applies.

This mesh velocity may be explicitly chosen by the user, or as is the case here determined algorithmically. In this study the mesh velocity of the moving boundary is obtained from the rate of bed level change arising from the Exner equation (2.17) and propagated into the interior of the mesh, under a specified smoothness criterion, and with the other boundaries held fixed. In this way, the moving mesh method is used to continuously adjust interior node locations in response to bed deformation, while seeking to keep the mesh of high quality and resisting the tangling of elements.

Since the mesh velocity is chosen explicitly, it is possible to choose the mesh coordinate as $\boldsymbol{\chi} = \boldsymbol{x}\left(t^0\right) + \frac{1}{2}\Delta t \boldsymbol{V}$, i.e. the physical coordinate at the time level of the right hand side of the PDE. This allows the substitutions $\nabla_{\boldsymbol{x}} = \nabla_{\boldsymbol{\chi}}$, $\mathcal{J} = \mathcal{I}$ in the weak form above, so that the DG method takes essentially the same form as for fixed-mesh problems. A similar method is applied for the control volume discretisation of the tracer quantities (sediment, turbulent kinetic energy and turbulent dissipation). In practice, since the timestepping operator is split and advection solved using an explicit method, this introduces a small discrepancy, of equal order to the use of an explicit timestepping method. Since the bed movement is slow relative to the fluid velocity, we neglect the advection sub-cycling in the wall boundary conditions for the turbulence model.

Some implementations were considered and tested in order to achieved a high enough measure of mesh quality. The Laplacian smoothing is achieved through the solution of an elliptic PDE. For example a two-dimensinal computational domain with coordinate vector (ξ, η) and map it to the time-evolving physical domain with coordinate vector (x, y) where the underlying physical solutions (i.e. pressure and velocities) are computed. The mapping $T : (\xi, \eta) \to (x, y)$ is defined as the solution of the system of PDEs,

$$\nabla^2 x = x_{\xi\xi} + x_{\eta\eta} = 0\,; \tag{4.26}$$

$$\nabla^2 y = y_{\xi\xi} + y_{\eta\eta} = 0\,; \tag{4.27}$$

where the Laplacian operator ∇^2 is applied in the computational domain and with boundary conditions given by the current position of the physical domain boundaries. Applying this to the mesh velocity itself will result in solving,

$$\nabla \cdot \gamma \nabla \boldsymbol{V} = \boldsymbol{0}, \tag{4.28}$$

with some mesh deformation parameter, γ. Solutions to this mapping are generally very smooth leading to equipotential contours where the interior grid points are relocated in response to boundary deformation. However, this technique has an important drawback, in a nonconvex domain, nodes may run outside it. For example, if an external boundary moves inwards too much and creates a nonconvex domain this smoother will most likely produce a tangled mesh.

Previous scour studies, e.g. [51, 111, 55], have typically applied an approach equivalent to a pure Laplacian smoothing criterion for the numerical modelling of local scour. This simple scheme is appropriate on vertically structured, quadrilateral-based meshes, or to small displacements in which tangling is a minor issue. In this work, the advantages of a lineal elasticity approach are demonstrated, specifically a torsional spring-based smoother [24]. This smoother is derived from a discrete analogy to the deformation of an elastic material kept in constant quasi-equilibrium acting over the whole mesh domain and driven by an externally applied boundary displacement. The individual vertex displacements (and thus the mesh velocity) are assumed to satisfy equations analogous to linear elasticity equations with a fictitious spring attached to each edge connecting two vertices i and j,

$$\mathcal{K}_{ij}\left[\boldsymbol{x}_j(t^{n+1}) - \boldsymbol{x}_j(t^n)\right] = (t^{n+1} - t^n)\mathcal{K}_{ij}\boldsymbol{V}_j = \mathbf{0}, \tag{4.29}$$

along with the boundary condition (4.14). The lineal torsional stiffness matrix, $\mathcal{K}$, may be partitioned as

$$\mathcal{K} = \sum_{\boldsymbol{k}\in\text{edges}} \mathcal{K}_{\boldsymbol{k}}^{\text{lineal}} + \mathcal{K}_{\boldsymbol{k}}^{\text{torsional}}. \tag{4.30}$$

Here the lineal term, $\mathcal{K}_{\boldsymbol{k}}^{\text{lineal}}$ applies equal and oppositely directed linear Hookean pseudo-forces at the two vertices sharing an edge, $\boldsymbol{k}$, with a spring constant inversely proportional to the edge length. This term thus resists possible displacements which collapse the edge and acts to equipartition changes in edge length across the whole mesh. Similarly the torsional term, $\mathcal{K}_{\boldsymbol{k}}^{\text{torsional}}$, applies an angular Hookean force on the third node of each of the two elements sharing an edge (assuming two-dimensional triangular elements), with a torsional spring force inversely proportional to the element area, thus resisting displacements which would cause the mesh to tangle by moving that vertex through the edge. The sparse matrix equation (4.29) for the $\boldsymbol{V}_i$ is solved using the same solvers as the discretised fluid model. This method provides a more robust smoother on unstructured meshes than the Laplacian smoother, at the cost of more expensive assembly.

4.3.3 Load balancing and parallelisation

In order to parallelise the model (both the discretisation as well as the application of mesh adaptivity), the first step is to divide the whole mesh into a number of sub-domains through a process referred to as domain decomposition; here this is a pre-processing step. After the initial decomposition of the mesh, each message passing interface (MPI) process then reads their local mesh and performs local finite element assembly to form global discretisation matrices which are solved using linear solvers and preconditioners available here through interfacing with the PETSc library (`http://www.mcs.anl.gov/petsc/`). Since the mesh optimisation step (described above) alters the local degrees of freedom count on each sub-domain, and consequently leads to each MPI process taking a different amount of time to complete impacting on overall solver efficiency, a dynamic load balancing step is a necessity. This involves exchanging elements (or migrating data) between sub-domains and here a parallel graph partitioner algorithm is utilised to achieve this via interfacing with the Zoltan library (`http://www.cs.sandia.gov/zoltan/`). The load balancing step is additionally used to parallelise a serial mesh optimisation algorithm. Each process optimises the mesh locally with halo regions between sub-domains locked, and hence the overall mesh contains unoptimised elements. Edge weighting is then applied at the graph partitioning step to encourage the load balancing to perturb updated halo regions away from previously locked elements. Local mesh optimisation, and load balancing, steps are then repeated several times resulting in a parallelised mesh adaptivity algorithm as well as a load-balanced mesh where all elements have been considered for optimisation [85, 32].

4.4 Numerical results and discussion

In order to demonstrate and validate the modelling approach developed in this work, a test case of current-induced scour around a circular object in 2D (which can be thought of as an infinitely long horizontally-lying pipe) is considered. This is an important problem since scour can affect the stability of pipelines, and serves as a simple yet representative example of further real-world problems which may involve more complex geometries. It is also a very challenging problem for two reasons: (i) the presence of the circular void representing the structure significantly constrains the mesh and its movement; and (ii) the initial thin clearance between the pipe and the bed leads to high stresses and strong scour, and thus the need for a high degree of mesh movement and also significant differences in the number of degrees of freedom required to accurately model the currents (and hence scouring processes) between the early and late stages of a simulation. This problem also benefits from the availability of experimental data [63] as well as prior modelling studies [51].

4.4.1 Simulation configuration

A two-dimensional initially rectangular flow domain is considered, as shown in figure 4.4. The domain is $L = 30D$ long and $H = 4D$ high, where D is the pipe diameter. The pipe centre was located $10D$ downstream of the inlet boundary. The height of the pipe was such that its bottom just touches the location of a flat bed.

When the pressure gradient in the bed-material between the upstream and downstream zones around a bottom-lying pipe reaches a critical value for seepage failure, tunnel erosion may initiate and the current velocity in the gap then increases rapidly [96]. As with similar modelling studies, e.g. [51], this onset phase was skipped here because the physics of the seepage flow within the porous soil underneath the pipeline is not accounted for in this modelling approach. The starting bottom boundary location/shape was therefore adjusted to yield a small initial clearance of size e between pipe and bed. Following the work from Liang et al. [51] the initial bed location was given an initial negative half cycle sinusoidal shaped small perturbation to yield a localised gap between the bottom of the pipe and the bed of amplitude $e = 0.1D$.

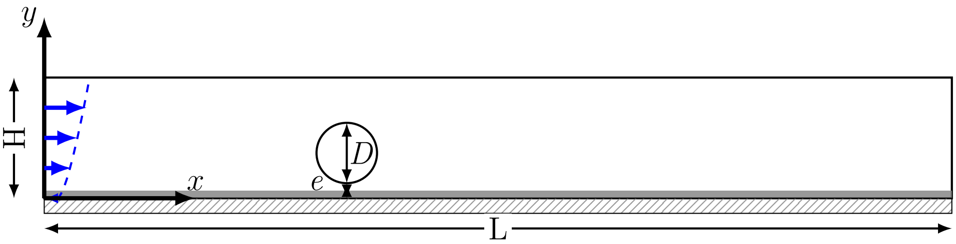

Figure 4.4: Schematic of the two-dimensional domain configuration. The grey area indicates a region of infinite sediment excluded from volume calculations. e is the gap between the pipe and the bottom erodible boundary.

In terms of initial and boundary conditions, the simulated flow is assumed to be a hydrostatic pressure-balanced rigid lid flow (i.e. no free surface is present in the model). At the inlet (left-hand side) boundary, a logarithmic velocity profile with a mean inlet velocity was applied (commonly developed in channel geometries) and the turbulent initial quantities were approximated from CFD formulae used for free-stream conditions and based on the turbulence intensity ($I = 5\%$) and the turbulent length scale l, estimated as a small percentage of the channel height (i.e. $l = 0.07H$). At the outlet boundary the pressure perturbation is set to zero. The bottom erodible boundary and the pipe surface are defined with a standard turbulence wall functions reproducing the behaviour of the boundary layer as described in chapter 3. For sediment concentration boundary conditions the flux of sediment through all surfaces, except the bottom, is set to zero while for the bottom boundary the suspended sediment flux is derived as the net upward normal flux such that $\mathbf{q_s} \cdot \mathbf{n} = E - D$. Within the bottom boundary, the sediment concentration is assumed to be uniform and the volume of sediment is infinitely available such that the bed is always erodible, i.e. the simulations here cannot hit bedrock.

4.4.2 Discussion

The numerical simulations were compared to the laboratory experimental results of Mao [63]. While the set-up of this problem is uniform in the cross-flume direction, some three-dimensional effects will of course still be present in reality. However, following the approach taken successfully by a number of authors studying this problem numerically, and the same two-dimensional approach was utilised. An overview of the system parameters is given in table 4.1. The simulations conducted here correspond to the experiments with conditions for a Shields parameter of $\tau^* = 0.048$ (low value close to clear-water scour regime) and a Shields parameter of $\tau^* = 0.098$ (in live-bed scour regime). With regards the numerical parameters for mesh adaptivity, the simulations were performed with an unstructured mesh of triangular elements with the parameters as given in table 4.2. All computations were conducted in parallel using 16 processor cores.

Parameter		Experiment $\tau^* = 0.048$	Experiment $\tau^* = 0.098$
Geometry and Flow			
Diameter	D	$0.1\,m$	$0.1\,m$
Maximum gap height	e	$10\,mm$	$10\,mm$
Mean inlet velocity	$\|\mathbf{u}\|$	$0.35\,m/s$	$0.5\,m/s$
Sediment Transport			
Angle of repose	ϕ	30°	30°
Submerged specific gravity	R^*	1.65	1.65
Particle median diameter	d_{50}	$360\,\mu m$	$360\,\mu m$
Particle diameter 90th percentile	d_{90}	$480\,\mu m$	$480\,\mu m$
Unhindered settling velocity	u_{so}	$0.055\,m/s$	$0.055\,m/s$

Table 4.1: Parameters used for simulations of the horizontal pipe scour test case. These parameters correspond to those used in Liang et al. [51].

Adaptivity Method	Options summary
h-adaptivity	The maximum and minimum edge lengths were specified with values of $0.04\,m$ (corresponding to the initial element characteristic length) and $1 \text{ x } 10^{-3}\,m$ respectively. The number of timesteps between optimisation of the mesh was chosen to be 15 as it was found (through experimentation) as the best compromise between cost and robustness. The weights for the error metric construction (e_{f_i} in section 4.3), chosen to provide good results in terms of overall mesh quality were: $\epsilon_{u1} = 0.035\,ms^{-1}$, $\epsilon_{u2} = 0.0035\,ms^{-1}$ for experiment $\tau^* = 0.048$ and $\epsilon_{\mathbf{u1}} = 0.05\,ms^{-1}$, $\epsilon_{\mathbf{u2}} = 0.005\,ms^{-1}$ for experiment $\tau^* = 0.098$ where $u1$ and $u2$ represent the velocity components.
r-adaptivity	A lineal-torsional-spring method was used driven entirely by bed deformation.

Table 4.2: Parameters used for mesh adaptivity in the horizontal pipe scour test case.

Based upon laboratory experiments, and corroborated by consistent numerical results, during the early stages of scour the erosion rate is very high (due to the tunnel erosion), so that the scour depth reached $\sim 4\,cm$ after 1.5 minutes for the $\tau^* = 0.098$ case and approximately 2.5 cm after 10 minutes for the $\tau^* = 0.048$ case. A higher Shields parameter means that the scour hole reaches an equilibrium state faster. The equilibrium stage for the $\tau^* = 0.098$ case began to develop at approximately 30 minutes of simulation time, with a maximum scour depth of $\sim$ 8 cm. Figures 4.5 and 4.6 illustrate experimental bed profiles around the pipe at different times, along with the numerical results of Liang et al. [51] (for their medium mesh k–ϵ based results which they found to represent a good compromise between accuracy and efficiency).

For the Fluidity results in figure 4.5, which corresponds to the case with $\tau^* = 0.048$, it is observed that at the very early stages of scour (frame (a) – profile I), the scour depth is slightly deeper than that observed experimentally. This could be a result of the assumptions made with regards to the initial bed profile employed to emulate the tunnel erosion stage (and also noting that the Liang et al. [51] results this set-up is based upon show something similar). The seepage flow phase early in the experimental setup would have led to a slight mismatch between the timings of the experimental and numerical results, with the experimental profiles potentially lagging the numerical ones which are effectively initiated at the end of the seepage phase. It should be noted that the omission of this (i.e. seepage process) could also be a result on an underprediction of sediment transport rates (at the lee side of the pipe) in this model.

(a) (10 min)

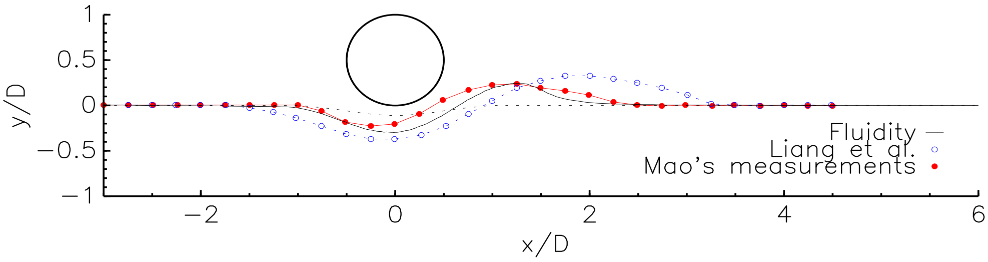

(b) (30 min)

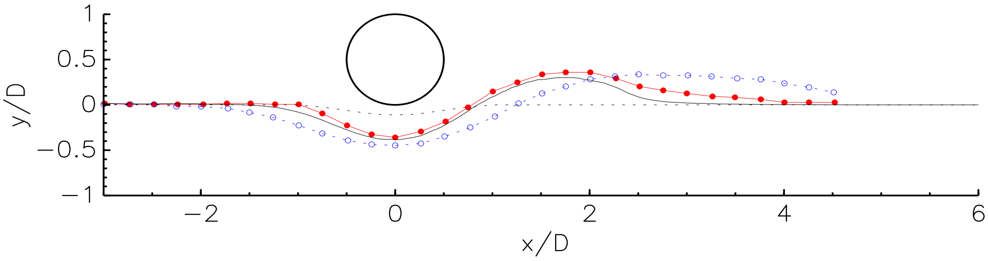

(c) (200 min)

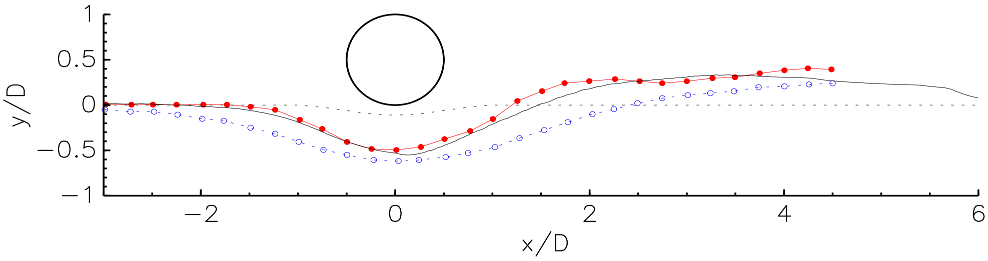

(d) (370 min)

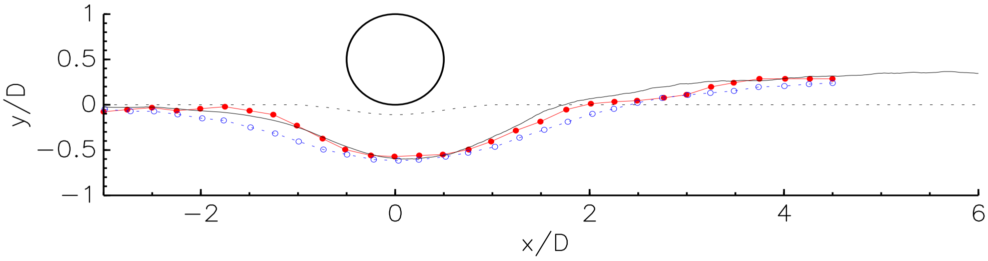

Figure 4.5: Bed evolution at different times for the Fluidity model using experimental data from case $\tau^* = 0.048$. Also shown are the corresponding experimental data from Mao [63] and numerical results from Liang et al. [51]. (*a*) Profile I at $t = 10$ min, (*b*) Profile II at $t = 30$ min, (*c*) Profile III at $t = 200$ min, (*d*) Profile IV at $t = 370$ min. The dashed line shows the initial bed profile.

In frame (*b*) – profile II, after the tunnel erosion has created a scour hole underneath the pipe, the scour rate decreases as the gap grows. This subsequent stage is referred to as lee-wake erosion, where vortex shedding from the pipe controls the scour. Experimentally, it was observed that during this phase more scour will occur on the upstream side. This model is able to predict a faster upstream erosion and also a characteristic bedform (dune-like) formation due to accretion of sediment in the downstream section.

In frame (*c*) – profile III, the scour hole has deepened and the flow below the pipe has slowed, and the vortices have weakened and finally vanished. A consequence of this is that the mean velocity in the gap and the bed shear stress reach a quasi-equilibrium and remain approximately constant; as a result, no major changes in the bed profiles are observed apart from a slow downstream migration of the dune. A good match is observed in the scour depth with respect to the other numerical model results and the experimental result, and this agreement is maintained until the end of the simulation. Frame (*d*) – profile IV shows both models agreeing very well with the experimental result both in terms of maximum scour depth below the pipe as well as the downstream profile.

For results with $\tau^* = 0.098$, shown in figure 4.6, it can be seen that most of the scour occurs rapidly in the earliest times of the experiment. This model results show fairly good agreement with the experimental results throughout the initial tunnel erosion phase and the subsequent lee-wake erosion phase, noted by a generally good profile match in frames (*a*) and (*b*). However, the downstream accretion seems to be over-predicted at the later simulation times. This is considered to be a consequence of the formation of bedforms, which shield the flow and encourage sediment deposition behind the pipe. At the final time (frame (*d*)) the Fluidity result shows a better scour depth agreement than the other numerical result, while there are similarities in the two models' disagreement with the downstream experimental profile.

Figure 4.7 shows the progression of the mesh as the bed profile evolves for the case with $\tau^* = 0.098$ (n.b. very similar images and discussion would be obtained for the $\tau^* = 0.048$ case in figure 4.9) in which changes in the adapted mesh due to the optimisation process are shown (frames (*a*), (*c*), (*e*) and (*f*)). Also displayed are some frames ((*b*) and (*d*)) showing the evolution of a coarse mesh undergoing mesh movement alone (i.e. no mesh optimisation and so fixed degree of freedom count and element connectivity). Mesh quality at the time of profile II at $t = 5$ minutes is compared in figure 4.8 with a zoomed view of the scour gap for the cases with and without mesh optimisation in frames (*a*) and (*b*) respectively. It can be observed that while the early time fixed mesh looks reasonable, the elements have become poorly shaped and sized by the time of frame (*b*). In can also be observed that the poor quality mesh (as coarser mesh resolution was initialised in the fixed mesh downstream of the pipe and this can not evolve as the simulation develops) is impacting on the numerical result in terms of the lack of the formation of appropriate downstream bedform profiles (e.g. downstream dune). The mesh quality measure plotted is the edge ratio (the ratio of the longest edge length to the shortest) and provides information similar to the element aspect ra-

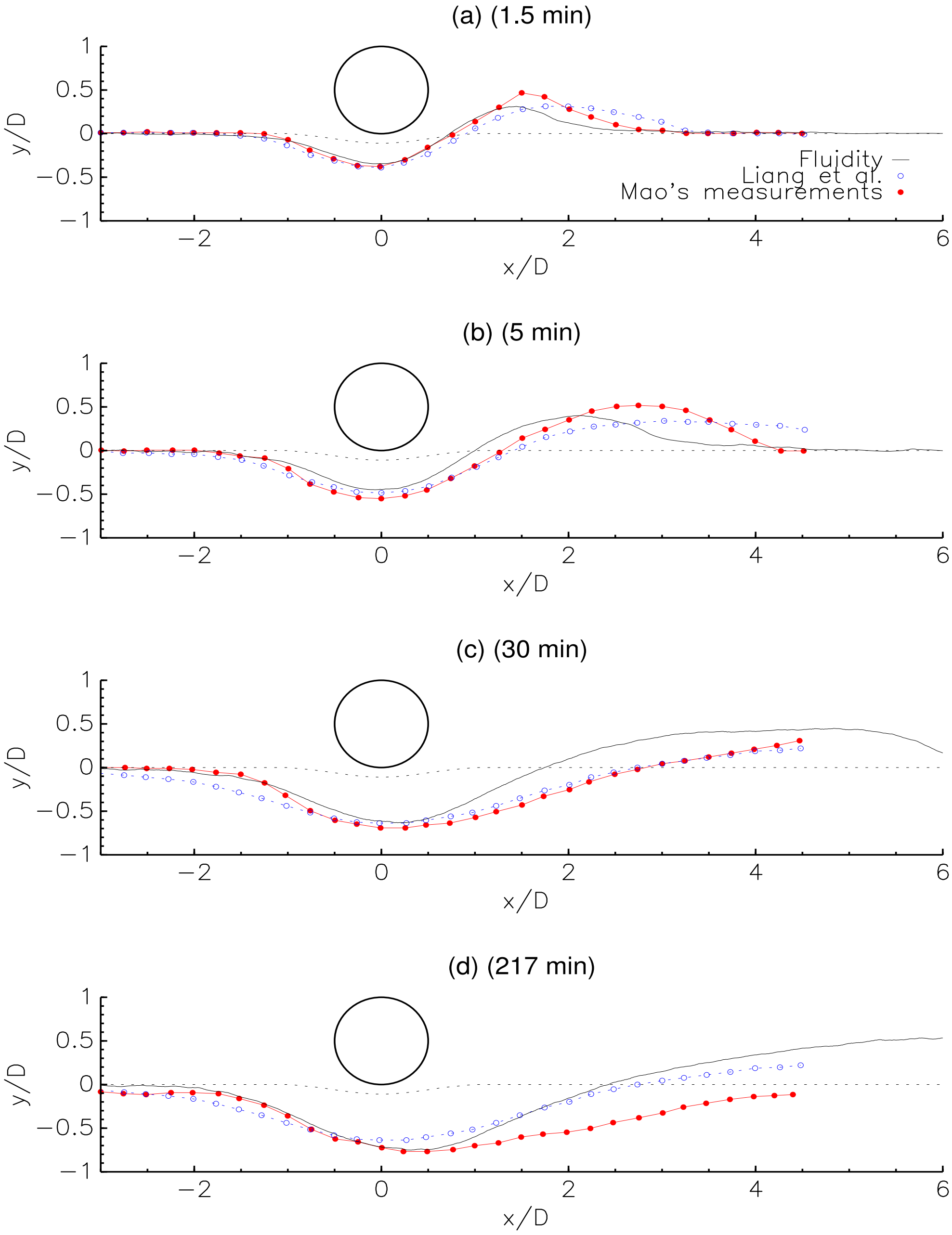
(a) (1.5 min)

(b) (5 min)

(c) (30 min)

(d) (217 min)

Figure 4.6: Bed evolution at different times for the Fluidity model using experimental data from case $\tau^* = 0.098$. Also shown are the corresponding experimental data from Mao [63] and numerical results from Liang et al. [51]. (*a*) Profile I at $t = 1.5$ min, (*b*) Profile II at $t = 5$ min, (*c*) Profile III at $t = 30$ min, (*d*) Profile IV at $t = 217$ min. The dashed line shows the initial bed profile.

tio. As observed in frames (*c*) and (*e*) and (*f*) from figure 4.7, the use of a mesh optimisation approach results in elements that are generally more appropriately shaped and sized. Completely opposite to the mesh movement only result, individual elements are only stretched anisotropically in the direction of flow as would be expected from the mesh optimisation algorithm and the fact that the metric formed is based upon the velocity field; thus, providing an optimal approach for the resolution of boundary/shear layers and fronts. In terms of the quality again, in frame (*a*) from figure 4.8, the majority of elements in the gap are actually close to isotropic; here anisotropic elements are not seeing within the bottom boundary layer as might be expected. This is a result of the fact that the bed is not flat, while using (isoparametric) elements with flat edges. This results in a constraint on the ability of the mesh optimisation operations to strictly achieve what the error metric is requesting of a fully optimised mesh, e.g. it is unable to remove nodes without modifying the representation of the boundary geometry.

Figure 4.10 shows a zoomed in view (in frame (*c*)) of a squashed element from a mesh movement only simulation with a finer refinement than was shown above. A thin sliver element can be seen to have formed due to the extreme bed deformation and the simulation is very close to failing. Although the lineal-torsional smoothing method used here offers very robust performance for external moving boundaries, the addition of a mesh optimisation process clearly helps to avoid both the excessive stretching and inversion of the near boundary elements, which would otherwise compromise mesh quality and thus impact the accuracy and

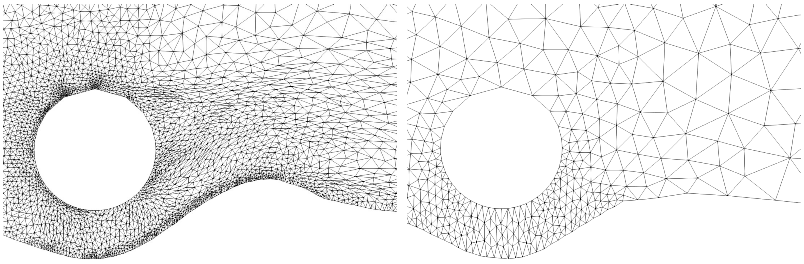

(a) Profile I at $t = 1.5$ min. (b) Coarse at $t = 1.5$ min.

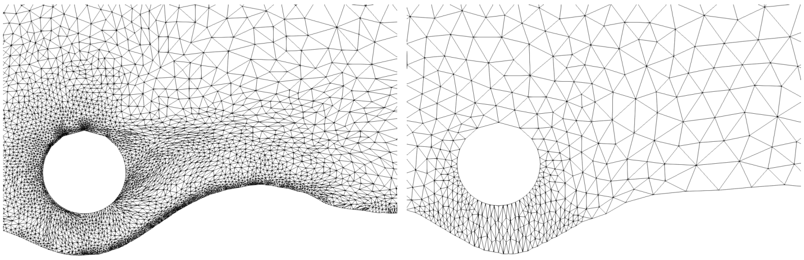

(c) Profile II at $t = 5$ min. (d) Coarse at $t = 5$ min.

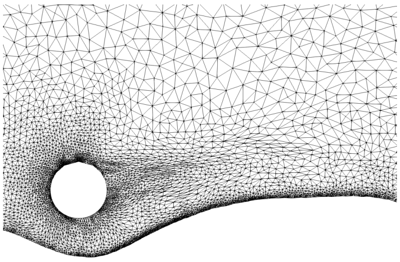

(e) Profile III at $t = 30$ min.

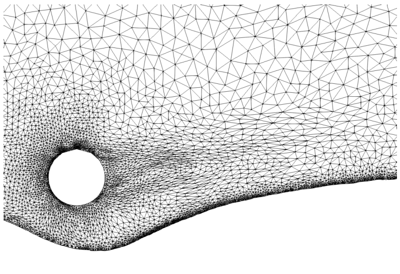

(f) Profile IV at $t = 217$ min.

Figure 4.7: Mesh visualisations of the adaptive mesh simulation (profiles I–IV), including the mesh results of the fixed coarse mesh simulation for the $\tau^* = 0.098$ case.

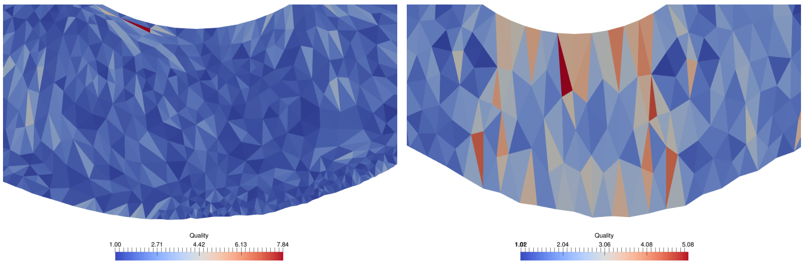

(a) Adapted mesh with mesh optimisation.

(b) Fixed mesh with mesh movement only.

Figure 4.8: Mesh quality visualisations of the adaptive mesh simulation (profile II) for the $\tau^* = 0.098$ case.

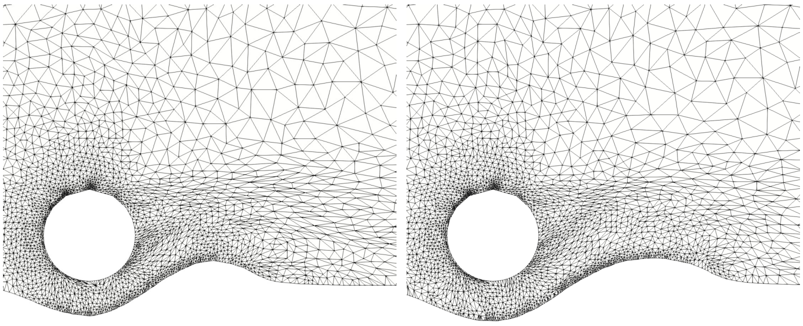

(a) Profile I at $t = 10$ min.

(b) Profile II at $t = 30$ min.

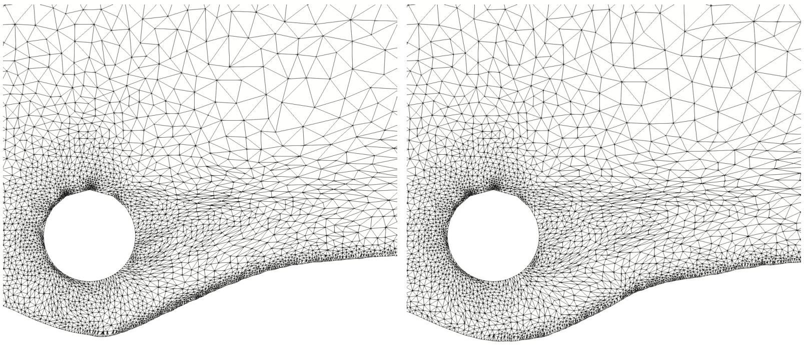

(c) Profile III at $t = 200$ min.

(d) Profile IV at $t = 370$ min.

Figure 4.9: Mesh visualisations of the adaptive mesh simulation (profiles I–IV) for the $\tau^* = 0.048$ case.

robustness of the solver.

Bed slope instabilities were satisfactorily controlled with the avalanche flux (sand-sliding-type) model that prevents the local boundary slopes significantly exceeding the angle of repose or maximum friction angle normally reported for loose sands.

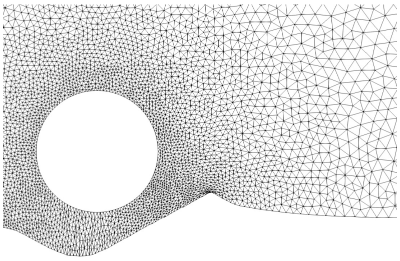

(a) Fine mesh.

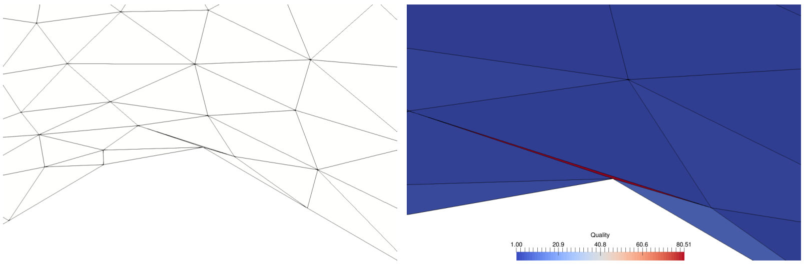

(b) Zoomed fine mesh.

(c) Mesh quality.

Figure 4.10: Mesh visualisations and mesh quality diagnostic for a mesh movement only simulation at $t = 1.5$ min for the $\tau^* = 0.098$ case, demonstrating element collapse and near inversion.

Chapter 5

Local scour around a vertical cylindrical pile

Contents

5.1 Introduction

Local scour near vertical piles and piers, or commonly known in civil engineering research as bridge scour, has been studied mainly through experimental investigation for more than one hundred years [64]. A major feature of the flow structure near the obstacle are vortex systems including principally, horseshoe vortices and wake vortices amongst others, it is the effect of these systems that lead to the scour of sediment from around the base of the vertical structure [66]. In a flow field with an isolated cylinder, the vortex shedding phenomenon is a dominant feature for this flow configuration in which periodic vortices are shed alternately at either side of the cylinder structure depending of the flow regime (i.e. the Reynolds number, Re) and this problem has attracted a lot of theoretical and practical research interest in the practice of computational fluid dynamics (CFD) [75]. For flow near a cylinder mounted on a rigid flat or an erodible bed, the major flow structures present are composed of two basic systems: (i) the horseshoe vortex formed due to the adverse pressure gradient on the upstream face of the vertical cylinder capable of promoting a downward flow of the boundary layer of the incoming flow and (ii) the wake vortex formed at the structure itself with a mechanism similar to the vortex shedding around an isolated circular cylinder. The intensity of the wake vortex depends on the cylinder geometry and the Reynolds number (Re). A circular cross section pier or pile will create a weaker or (for a streamlined shape) virtually no wake, whereas a blunt profile produces a stronger one [65].

The discretised numerical model devised in section 4.2 from chapter 4 in combination with the mesh adaptivity framework described in section 4.3 from the same chapter is applied here to study the three-dimensional flow field and scour formation around an obstacle in the flow, (i.e. around a cylindrical, circular cross section pile) on a live-bed (entire bottom may be mobilised with locally higher stresses) in steady current conditions. In the remainder of this chapter some of the differences with respect to the previous implementation will be pointed out in the next section and finally the performance of the model will be compared with simulation results of a previously validated model for local scour around a single circular cylinder.

5.2 Notes on implementation

5.2.1 Mass-lumping regularisation

In the implemented numerical model, when calculating the bed level change from the Exner equation (2.17) a particular matrix-based regularization technique was applied to the bedload transport contribution to avoid instability caused by the non-linear relationship between the sediment transport rate and bed level change. Despite the computational advantage accrued with this scheme, in three-dimensional configurations slopes of the developing scour holes presented peculiar effects due to the nature of the bed load calculation. Generally, this formula dismisses the influences of the bed slope on the direction of the bed load transport and assumes that the direction of the bed load transport is the same with the direction of the wall shear stress on the bed. In two-dimensional simulations, this formula is applicable without problems. However, in three-dimensional simulations, the effects of the bed slope on the direction of the bed load transport can be included to improve the accuracy of the model. Some modifications to the original (i.e. bedload) formulation have been proposed [90] taking into consideration a force balance on the sediment particles assuming that they move in uniform mean velocity U_b for the cell surface in the bottom boundary. Consequentially, in order to maintain the idea of linking the bed velocity directly with the tangential bed shear stress at the computational boundary, together with reducing the bed slope three-dimensional effects, a numerical filter in time is applied to the bed level elevation change itself. This will act as a sort of averaging operator for the displacement of the surface mesh nodes,

$$\Delta h^n = 0.25(\Delta h^{n-1} + \Delta h^{n+1}) + 0.5\Delta h^n, \tag{5.1}$$

where, n indicates the current surface level and Δh the variation of the bed level elevation.

The proposed numerical filtering may be additionally combined in each time step with a spatial regularisation on the bed evolution profile based in a global mass-lumping technique, resulting in a linear system of equations given by,

$$\sum_{j=1}^{N} M_{ij}\eta_i^* = f_i \qquad \text{for} \qquad i = 1, 2 \ldots N, \tag{5.2}$$

where, η^* are the (unknown) N nodal values of the unsmoothed bed level field $\eta(x, y, t)$ and M_{ij} (the lumped mass matrix) together with f_i (the total bedload and suspended sediment transport contributions) are the global quantities formed by assembling element-wise, Ω_e,

$$M_{ij}^e = \int_{\Omega_e} \Psi_i \Psi_j d\Omega_e \qquad \text{and} \qquad f_i^e = \int_{\Omega_e} f_i \Psi_i d\Omega_e, \tag{5.3}$$

where, Ψ_i is a set of linear piecewise polynomial global basis functions. The nodal values of the smoothed bed level are obtained by the solution of the previous linear system of equations (5.2). This scheme has the benefit of acting as a global smoothing without the need to specify an appropriate smoothing length parameter (as per the previous mass matrix regularisation for the bedload term) and with the use of lumped mass matrix the solution is almost trivial due to the matrix inversion.

The mass lumping scheme is performed at the element level and is based on a row sum method traditionally used for many years [110, 37]. It is obtained by summing across each row of the consistent mass matrix,

$$M_{ii}^e = \sum_j M_{ij}^e = \sum_j \int_{\Omega_e} \Psi_i \Psi_j d\Omega_e = \int_{\Omega_e} \Psi_i d\Omega_e. \tag{5.4}$$

The triviality of the inverse of the mass matrix operation in the linear system $\mathcal{M}\mathbf{x} = \mathbf{b}$,

$$x_i = \frac{b_i}{\int_{\Omega_e} \Psi_i d\Omega_e} = \frac{\int_{\Omega_e} \Psi_i f_i d\Omega_e}{\int_{\Omega_e} \Psi_i d\Omega_e}, \tag{5.5}$$

which suggests a physical interpretation as a weighted nodal averaging that if 4-node rectangular elements were used, this scheme becomes a simple area-weighted average as expressed in the generalised coordinate filter in (5.1).

5.2.2 Lineal elastic mesh movement

The lineal elasticity approach is an alternative methodology to the spring analogy for mesh movement, described in the previous chapter (section 4.3) which has been investigated for the mesh adaptation analysis [99, 15]. It is an equivalent analogy based on the discretisation of the computational domain as the simplest mathematical model (with a elliptical differential equation) of a linear elastic solid body. Hooke's law, relating the stress and strain tensors and assuming an isotropic and homogeneous material, which represents spatially constant elastic properties for the mesh movement, can be expressed as,

$$\boldsymbol{\sigma} = \lambda tr(\boldsymbol{\epsilon})\mathcal{I} + 2\mu\boldsymbol{\epsilon}. \tag{5.6}$$

where, μ and λ are Lamé's elastic coefficients, relating to Youngs modulus of elasticity E and Poisson's ratio ν as,

$$\mu = \frac{E}{2(1+\nu)}, \tag{5.7}$$

and (for plane strain conditions),

$$\lambda = \frac{\nu E}{(1+\nu)(1-2\nu)}. \tag{5.8}$$

The infinitesimal strain tensor $\boldsymbol{\epsilon}$, is related to the displacement gradients by the expression,

$$\boldsymbol{\epsilon} = \frac{1}{2}\left(\nabla\boldsymbol{x} + (\nabla\boldsymbol{x})^T\right). \tag{5.9}$$

The motion of the mesh is then governed by the equilibrium equation in the computational domain Ω,

$$\nabla \cdot \boldsymbol{\sigma}(\boldsymbol{x}) + f = 0 \qquad \text{on} \qquad \Omega, \tag{5.10}$$

$$\boldsymbol{x} = \boldsymbol{x}_D \qquad \text{on} \qquad \Gamma, \tag{5.11}$$

where $\boldsymbol{x}$ denotes the deformed coordinates vector of the current mesh and $\boldsymbol{x}_D$ are Dirichlet boundary conditions completing the system. For cases where the motion of the mesh is driven purely by the displacement of the boundaries (as in this scour model), the body force is zero, i.e. $f = 0$.

A Galerkin-based weak form for linear static elastic can be used in analogy with the previous expression (5.11) prescribing (as adopted in this work) that the Dirichlet boundary conditions are satisfied at the outset (i.e. surface boundary Γ). Also, knowing that the displacement of the mesh coordinates is from a fixed reference vector $\boldsymbol{X}$, the implementation can be performed directly for the grid velocity, $\boldsymbol{V}$. Taking into account the previous conditions, the system can be rewritten as,

$$\int_\Omega \nabla\Psi : \boldsymbol{\sigma}(\boldsymbol{V}) d\Omega = 0, \tag{5.12}$$

where $\nabla\Psi : \boldsymbol{\sigma}(\boldsymbol{V})$ denotes the contraction of the tensors $\nabla\Psi$ and $\boldsymbol{\sigma}(\boldsymbol{V})$, expressed in component form as, $\nabla\Psi_{\alpha\beta}\sigma_{\beta\gamma}$. The preceding bilinear form is symmetric and may be also be expressed in another tensorial quantities related to the stress-strain law,

$$\boldsymbol{\sigma}(\boldsymbol{V}) = \mathcal{K}\boldsymbol{\epsilon} \qquad \text{or} \qquad \sigma_{ij} = \mathcal{K}_{ijkl}\epsilon_{kl}, \tag{5.13}$$

where, $\mathcal{K}$ represents the stiffness or elasticity matrix resulting in a new bilinear form,

$$\int_{\Omega} \boldsymbol{\epsilon}^T(\boldsymbol{\Psi})\mathcal{K}\boldsymbol{\epsilon}(\boldsymbol{V})d\Omega = 0. \tag{5.14}$$

The finite element assembly is performed using standard P1 finite elements and the linear system is solved using an preconditioned restarted conjugate gradient method, using the PETSc library.

This node movement scheme has proven to be much more robust than commonly used spring analogy or velocity diffusion techniques (i.e. Laplacian smoothing), as representing the full stress tensor allows mesh deformations to be propagated farther into the domain, particularly for shearing motions. Also, it has been conveniently tested in solving these elastic equations in parallel on decomposed domains [16].

5.3 Numerical results and discussion

In this test case a current-induced scour simulation around a cylindrical pile was compared against experiments and numerical results from the work of Roulund et al. [90]. Flow around vertical (circular and square cross sections) cylinder mounted on a rigid bed has been extensively investigated by experimental and numerical models, and flow structures such as the horseshoe vortex have been explored and directly correlated as the possible mechanism leading to the scouring around the base of the vertical cylinder [66]. However, the analyses (particularly the numerical studies) of local scour due to hydrodynamic action around a pier are more complex and particular studies ([89, 90]) are still offering more guidance about the principle of this phenomenon.

5.3.1 Simulation configuration

A three-dimensional (3D) calculation domain is selected, as shown in figure 5.1. Different to the calculation of local scour around a horizontal pipeline in chapter 4, a cubical box is specified as the domain for the simulation of local scour around a vertical cylinder mounted on a bed. The experimental set-up (from Roulund et al. [90]) to investigate scour of an erodible bed was conducted in a current flume with a sand bed located in a pit of length $L = 5.65\, m$ and width $W = 3.6\, m$. The water depth was $H = 0.4\, m$ and the circular pile with diameter $D = 0.1\, m$ was placed downstream of the inlet section in the middle of the sand pit channel at a distance of $3.85\, m$ from the point where the incoming flow becomes undisturbed.

The boundary conditions for the flow field are defined with a rigid lid at the top and including only the water region and a slip boundary condition (at the top boundary) for the water surface resulting in free surface effects being neglected (also not considered in the work from Roulund at al. [90]). This is justified since the development of the scour hole around the cylinder does not have an obvious influence on the free surface position [6]. At the inlet, the velocity (in the vertical direction) is set to be

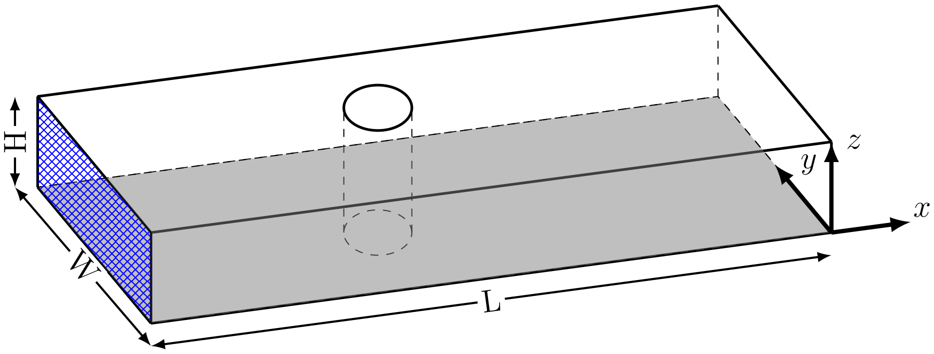

Figure 5.1: Schematic of the three-dimensional domain configuration considered in this chapter. The grey area indicates a region of infinite sediment excluded from volume calculations and the blue hatched region indicates the flow inlet.

uniform (i.e. undisturbed) and fully-developed into a logarithmic profile while the pressure is set to be zero gradient. For the initial turbulent properties, the turbulence intensity at the inlet boundary is set to 5% and the turbulent length scale is estimated as a small percentage of the channel height (i.e. $l = 0.07H$). At the outlet boundary the pressure field is set to a fixed value of zero and the velocity is zero gradient in the normal direction. The lateral boundaries together with the cylinder surface are defined with a *no normal flow* (where the component of flux in the direction normal to the boundary is zero) velocity condition.

The bottom boundary (analogous to the erodible bed) is set to a friction velocity condition (linked to a wall function) and the k and the ϵ fields are specified with its corresponding wall function boundary conditions as described in section 3.2 from chapter 3. The boundary condition for suspended load concentration is set to be zero for all inflow boundaries except for the bottom boundary where is defined using the entrainment rate and deposition rate presented in section 2.2.4 from chapter 2.

5.3.2 Discussion

Figure 5.2 illustrates the way in which the scour develops in front and at the back of the pile for a computational mesh with a number of cells of approximately 705,000 (details about the grid description are showed in table 5.2). In regards to the grid velocity in frame (*a*), the high intensity (red colour) visualisation represents the area where the scour hole is increasing in shape around the structure while the low intensities (blue colour) account for lower grid velocities promoting less scour. From the simulation parameters shown in table 5.1, it is noticed that the particle diameter 85th percentile value is assumed instead of the 90th percentile for the entrainment rate calculation based on the information available from the compared laboratory experimental setup presented in Roulund et al. [90]. As the test is in live-bed conditions, the bed is covered with ripples which can be appreciated with the small fluctuations of the grid velocity (red and blue) field in the bottom (bed) surface. With regards the numerical parameters for mesh adaptivity, the simulations were performed with an unstructured mesh of tetrahedra elements with the parameters as given in table 5.2. All computations were conducted in parallel using 16 processor cores.

A time sequence of frames illustrating the evolution of the scour hole area obtained in the present simulation is shown in figure 5.3 where the flow is approaching the pile from the left to right. It can be observed (via the figures' color map) the increasing magnitude of the bed elevation with time, presented here as the changes in the scour depth to pile diameter ratios $\frac{z}{D}$, where z is the scour depth in the z-direction. Amongst the

Parameter		Experiment live-scour
Geometry and Flow		
Diameter	D	$0.1\,m$
Mean inlet velocity	$\|\mathbf{u}\|$	$0.46\,m/s$
Sediment Transport		
Angle of repose	ϕ	$30°$
Submerged specific gravity	R^*	1.65
Particle median diameter	d_{50}	$260\,\mu m$
Particle diameter 85th percentile	d_{85}	$390\,\mu m$
Unhindered settling velocity	u_{so}	$0.038\,m/s$

Table 5.1: Parameters used for simulations of the live-bed scour around a pile test case. These parameters correspond to those used in Roulund et al. [90].

Adaptivity Method	Options summary
h-adaptivity	The maximum and minimum edge lengths were specified both: (i) radially from the center of the cylinder with values of $0.06m$ to $0.2m$ for the minimum and $0.06\,m$ to $0.3\,m$ for the maximum edge length as the radius increases and (ii) along the vertical elevation with values of $0.08\ m$ to $0.04\ m$ respectively. The number of timesteps between optimisation of the mesh was chosen to be 10 as it was found (through experimentation) as the best compromise between cost and robustness. The weights for the error metric construction (e_{f_i} in section 4.3 from chapter 4), chosen to provide good results in terms of overall mesh quality were: $\epsilon_{u1} = 0.002\ ms^{-1}$, $\epsilon_{u2} = 0.0002\ ms^{-1}$ $\epsilon_{u3} = 0.0002\ ms^{-1}$ where $u1$, $u2$ and $u3$ represent the velocity components.
r-adaptivity	A lineal elastic method was used driven entirely by bed deformation.

Table 5.2: Parameters used for mesh adaptivity in the live-bed scour around a pile test case.

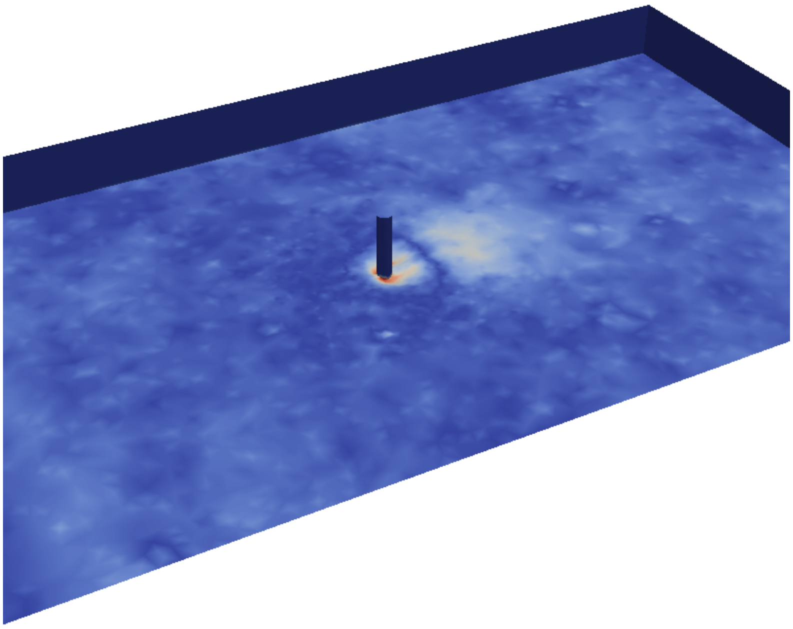

(a) Grid velocity visualization at $t = 5$ min. Higher values in red colour (●) and lower values in blue colour (●).

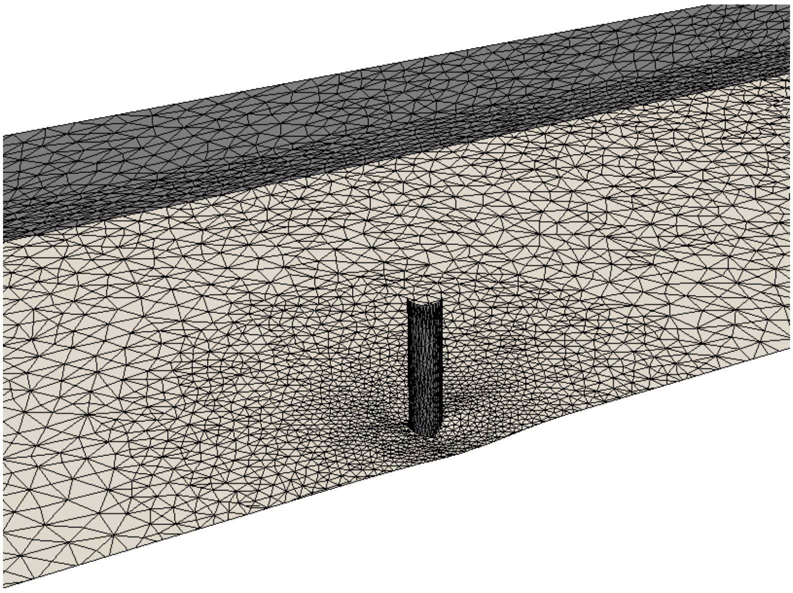

(b) Mesh visualization at $t = 5$ min.

Figure 5.2: Domain visualisation of the adaptive mesh simulation for the three-dimensional scour around a cylindrical pile case.

main features seen, and which compare well with previous laboratory and numerical experiments [6, 90] are: (i) the scour hole starts to form with a semi-circular (in plan view or $x-y$ plane) erosion pattern around the upstream part of the pile which then expands to the downstream side of the pile, (ii) an indication of the onset of downstream dune formation can be seen in two symmetric mounts of deposited sediment migrating in the direction of the flow (evidenced with the yellow colour representing the transition of the scour hole to dune formation) and (iii) the formation of a small ridge downstream of the cylinder noted as a missed part in the scenario (a) at $t = 1$ min. with its height becoming smaller as the scour hole deepens.

Comparing more quantitatively the maximum scour depth ratios from figure 5.3, in the scenario (b) at $t = 2$ min. the $\frac{z}{D} = 0.467$ underpredicts the existing data reported from figure 33 in the benchmark results of Roulund et al. [90] at the same time frame, being $\frac{z}{D} = 0.63$ and the discrepancy is increased by almost 30% in the scenario (d) at $t =$ 5 min and clearly larger differences between the simulated scour depth and the equilibrium scour depth at the downstream side of the cylinder are to be expected. No trivial explanation can be inferred for this lack of similarity in scour depths, nevertheless, some evident reasons (also expressed in previous numerical studies [6, 90]) are attached to the more complex three-dimensional flow field results. The horseshoe vortex causing an increase in shear stress in the bottom erodible bed has a significant influence in the development of the scour hole depth. From the hydrodynamics and possibly the turbulence modelling, the lack of vortex shedding (as part of the horseshoe vortex) causes an underestimation of the maximum bed shear stress amplification and the differences mainly occur in the lee-wake region, this could prevent the model from reproducing correctly the scour depth (particularly on the central plane) in the early stages of the scour.

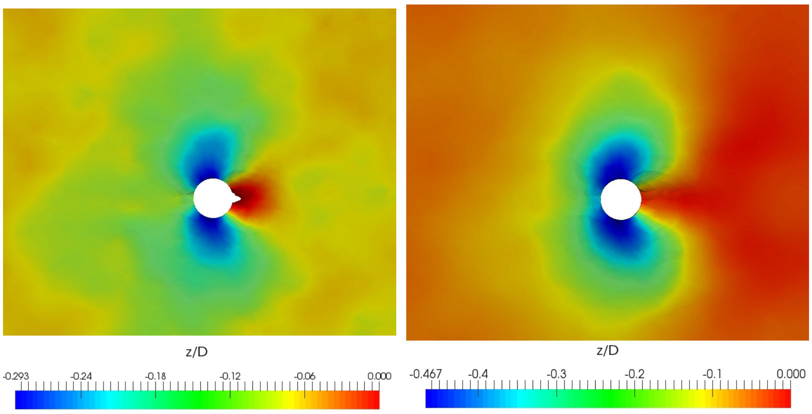

(a) $t = 1$ min. (b) $t = 2$ min.

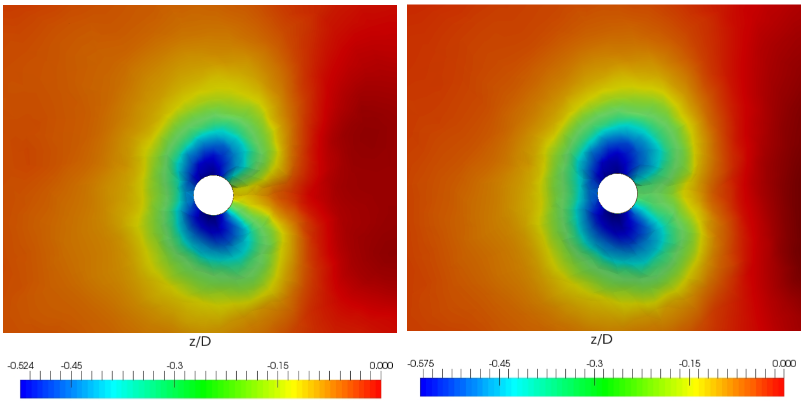

(c) $t = 3$ min. (d) $t = 5$ min.

Figure 5.3: Non-dimensional scour depth, $\frac{z}{D}$ visualisations of the adaptive mesh simulation for the three-dimensional scour around a cylindrical pile case. Red colour (●) indicates no scour depth and blue colour (●) indicates deepest scour depth. Flow from left to right.

From figure 5.4, contrasting with the results of Roulund et al. [90] at early times from the equilibrium stage (after around $t = 60$ min.), the bed

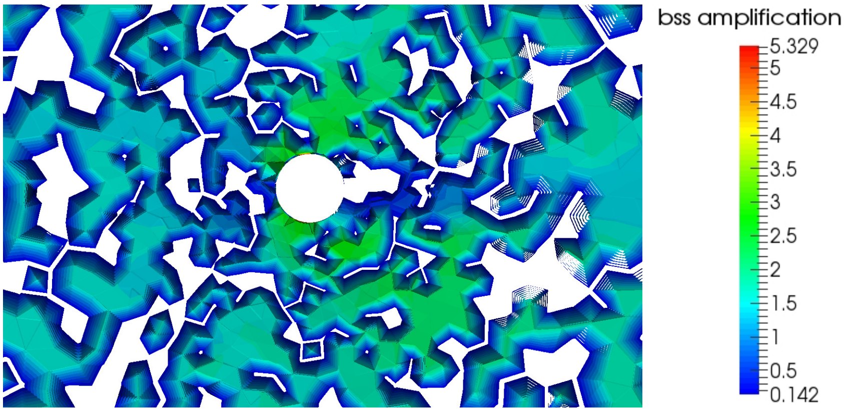

Figure 5.4: Contour map of bed shear stress amplification at $t = 5$ min.

shear stress amplification for the initial plane bed with a maximum value of $\alpha = \frac{\|\boldsymbol{\tau_w}\|}{\boldsymbol{\tau_{w\infty}}} = 6$ (where $\boldsymbol{\tau_{w\infty}}$ is the undisturbed bed shear stress) in figure 36(a) (of Roulund et al. [90]) is comparable with the bed shear stress amplification of $\alpha = 5.329$ (at $t = 5$ min. at still early scour stage) close to the upstream part of the cylindrical pile wall obtained in the current simulation. However, in the wake region close to the cylinder wall area the values of bed shear amplification are around half in magnitude lower than the Roulund et al. [90] results.

Furthermore, looking at the influence of scour on the flow field in figure 5.5, which represents a cut view of the $x - z$ plane at $y = 0$ m which corresponds to the central plane, we observe in frame (c) the velocity component in the z-direction which shows that there is flow circulation across the central plane of the upstream part of the cylinder which seems to have an important influence on the flow field in the simulation, as an initial indication of the down-flow process preceding the generation of horseshoe vortices in the scour hole. The strong vertical velocity on the central plane in the downstream of the cylinder seems to cause an upward deflection of the flow and transport of the sediment (suspended load) such that it gathers behind the cylinder and forms a (previously mentioned) ridge there. Upstream of the cylinder, the slope angle of the scour hole appears approximately equals to the repose angle of the sediment, also justifying the averaging imposed for the regularisation mechanism (described in section 5.2.1) aiding to control the sand-sliding. However, the presence of a gentle slope produced at the downstream side of the cylinder in this simulation suggests an underestimation of scour hole depth possibly due to a lack of bed shear stress amplification mainly in the wake region which could be associated to the limitations in capturing near-wall resolution when using a $k - \epsilon$ model for turbulence modelling.

The main objective of the present scour simulation is to investigate and validate the proposed framework combining the benefits of mesh optimisation and mesh movement techniques. The simulation results from Roulund et al. [90] were performed using a steady-state solver to simulate the flow field with $k - \omega$ turbulence closure and also pointed out that the equilibrium scour depth obtained from this simulation slightly disagrees with the experimental data observed for scour downstream of the pile possibly due the lack of intensity of unsteady effects (i.e. horseshoe vortex and lee-wake vortex flows). Further, it is speculated with this work that mesh distortion and limitation of the mesh resolution around the scour area could also be responsible for the difference between the simulated and measured (experimentally) scour depth in the results from Roulund et al. [90]. In the current simulation presented here, likewise, the vortex

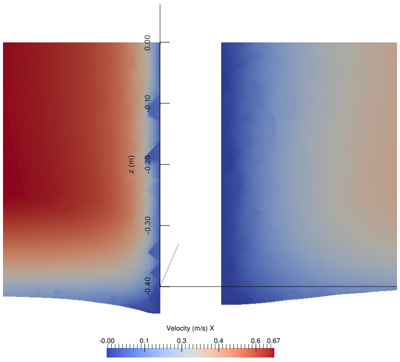

(a) Velocity in the x-direction.

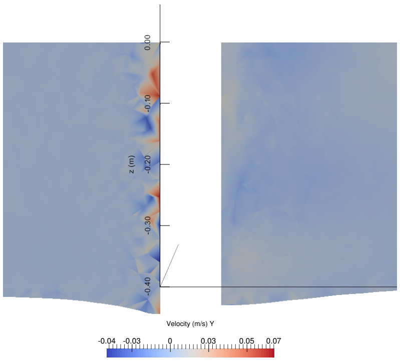

(b) Velocity in the y-direction.

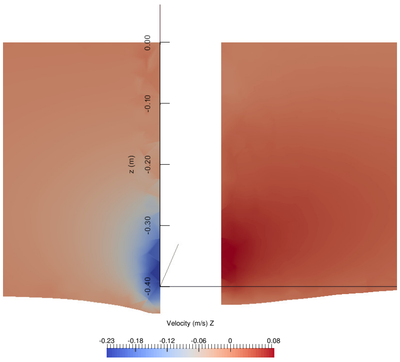

(c) Velocity in the z-direction.

Figure 5.5: Visualisation of the velocity field in the vertical plane passing through the pile at $t = 5$ min.

shedding is not clearly reproduced due to inadequate resolution of the mesh and the simulation gives directly the mean flow field but the overall control of the mesh offered by the combination of optimisation methods with mesh movements is robust. However, the hydrodynamic module requires a further investigation in the sensitivities of wall functions for the near-wall turbulence modelling. A guidance in future research will be given in section 7.2.

Chapter 6

Local scour using smoothed particle hydrodynamics

Contents

6.1 Introduction

Since its inception in the seventies, the use of smoothed particle hydrodynamics (SPH) has been extended into applications in both fluid and solid mechanics and further scientific arenas. However, in some problems concerning soil-water-structure interaction, such as scour and erosion where the essential physics are related to simulate the sediment transport process, the advantages of SPH are still in exploratory phase [93]. In contrast to conventional mesh-based methods, SPH offers a good capability to deal with large deformation and different phases, which makes it useful for simulating the large deformation and displacements of the soil-water interface that are associated with scour around structures. There are different approaches to model geomaterials (e.g. soils) behaviour in the SPH framework and they are discussed in more detail below. This chapter should be read in conjunction with a precedent background on SPH given in section 2.2.5 from chapter 2.

6.2 Approaches to model geomaterials with SPH

There are two main approaches which will be considered in order to model a soil material using the SPH method. In the first approach the soil model considers the granular material to be a fluid with a variable viscosity, where a non-Newtonian-type constitutive model is proposed based on a yield-stress (plastic) criterion and the viscosity is derived from geotechnical parameters (i.e. the cohesion and friction angle) [100].

The other approach is the use of a non-linear material constitutive model in the framework of solid mechanics. In the current study, both of these approaches are discussed and adapted into simulations to evaluate their performance.

6.2.1 Viscoplastic fluid

The main idea consists in approximating the behaviour of the soil as a highly viscous non-Newtonian fluid with yield properties (i.e. viscoplastic material). Viscoplasticity is conceptualised by a yield stress under which no deformation occurs. When the yield stress is exceeded, the material starts to flow. This has been successfully tested in another applications using finite-volume-based commercially available CFD software [23]. As expressed in equation 2.6 (described in the previous section 2.2.1), the shear stress tensor depends on the strain rate tensor of the viscous fluid. This constitutive model relates the deviatoric stress to the shear strain rate (i.e. the deviatoric rate of the deformation tensor), which for a generalised Newtonian viscous fluid results in

$$\boldsymbol{\tau'} = 2\mu_0 \left(\|\dot{\boldsymbol{\gamma}}\|\right) \dot{\boldsymbol{\gamma}}, \tag{6.1}$$

where, $\boldsymbol{\tau'}$ is the deviatoric viscous stress tensor, $\dot{\boldsymbol{\gamma}} = \mathcal{D} - \frac{1}{3}tr(\mathcal{D})\mathcal{I}$, is the deviatoric strain rate tensor, where $\mathcal{D} = \left(\nabla \mathbf{u} + (\nabla \mathbf{u})^T\right)/2$ and μ_0 represents the viscosity as a function of the measure of the strain rate given by $\|\dot{\boldsymbol{\gamma}}\| = \sqrt{2\dot{\gamma}_{ij}\dot{\gamma}^{ij}}$ approximated from the second invariant of the symmetric rate-of-strain tensor.

Amongst the many rheological models which incorporate non linear stress/strain-rate relationships, the Bingham plastic model, considered in this work, can be obtained by selecting the following constitutive equation which in simple shear flow takes the form

$$\boldsymbol{\tau'} = \tau_0 + \mu\dot{\boldsymbol{\gamma}} \qquad \text{for} \qquad \|\boldsymbol{\tau'}\| > \tau_0, \tag{6.2}$$

where, τ_0 is a specified yield stress possibly based on a yield criterion (e.g. Mohr-Coulomb used here) and μ is a constant plastic viscosity which is numerically chosen and has to be large enough (limiting at high strain rate) to guarantee that no significant motion occurs in unyielded regions. Also considered, the Herschel-Bulkley model, which combines the plastic forces along with the power-law model, in simple shear flow takes the form

$$\boldsymbol{\tau'} = \tau_0 + k\dot{\boldsymbol{\gamma}}^n \qquad \text{for} \qquad \|\boldsymbol{\tau'}\| > \tau_0, \tag{6.3}$$

where, k is the consistency index and n is the flow index. These equations (6.2) and (6.3) must be fully invariant constitutive relations in tensorial form applicable in three dimensions and they could be expressed as

$$\boldsymbol{\tau'} = \left(\mu + \frac{\tau_0}{\|\dot{\boldsymbol{\gamma}}\|}\right)\dot{\boldsymbol{\gamma}} \qquad \text{for} \qquad \|\boldsymbol{\tau'}\| > \tau_0, \tag{6.4}$$

and,

$$\boldsymbol{\tau'} = \left(k\|\dot{\boldsymbol{\gamma}}\|^{n-1} + \frac{\tau_0}{\|\dot{\boldsymbol{\gamma}}\|}\right)\dot{\boldsymbol{\gamma}} \qquad \text{for} \qquad \|\boldsymbol{\tau'}\| > \tau_0. \tag{6.5}$$

These constitutive equations (6.4) and (6.5) can be seen as a purely viscous generalised Newtonian fluid with an effective or apparent viscosity μ_{eff}, following the equation 6.1, where the effective viscosity considering a yield stress τ_0 based on a Mohr-Coulomb criterion is given by

$$\mu_{eff} = \begin{cases} \mu + \frac{c + ptan(\theta)}{\|\dot{\gamma}\|} & \text{if} \quad \mu_{eff} < \mu_{max}, \\ \mu_{max} & \text{if} \quad \mu_{eff} \geq \mu_{max}. \end{cases} \tag{6.6}$$

where, c is the cohesion, θ is the internal friction angle (both parameters for the Mohr-Coulomb criterion) and p is the pressure. For the Herschel-Bulkley model the effective viscosity takes the form,

$$\mu_{eff} = \begin{cases} k\|\dot{\gamma}\|^{n-1} + \frac{c + ptan(\theta)}{\|\dot{\gamma}\|} & \text{if} \quad \mu_{eff} < \mu_{max}, \\ \mu_{max} & \text{if} \quad \mu_{eff} \geq \mu_{max}. \end{cases} \tag{6.7}$$

For both of these models we have,

$$\dot{\boldsymbol{\gamma}} = 0 \qquad \text{for} \qquad \|\boldsymbol{\tau'}\| \leq \tau_0, \tag{6.8}$$

which means that strictly speaking the effective viscosity could reach an infinite value when the strain rate vanishes thus the material is always liquid and mimics the ideal model behaviour for all rates of deformation. Therefore, to circumvent this issue numerically, a maximum viscosity with a huge but finite for a given soil μ_{max} is introduced as a cut-off for the limiting value.

Finally, the SPH representation of the momentum equation for a general Newtonian viscous fluid can be expressed as,

$$\frac{D\mathbf{u_a}}{Dt} = \sum_b m_b \left(\frac{\boldsymbol{\sigma}_{\boldsymbol{a}}^{ij}}{\rho_a^2} + \frac{\boldsymbol{\sigma}_{\boldsymbol{b}}^{ij}}{\rho_b^2} \right) \nabla_a W_{ab}, \tag{6.9}$$

considering the total stress tensor $\boldsymbol{\sigma}$,

$$\boldsymbol{\sigma} = -p\mathcal{I} + \boldsymbol{\tau'}. \tag{6.10}$$

It may be needed to add some additional artificial terms to (6.9) such as: i) artificial viscosity term , Π_{ab} discussed in section 2.2.5 and/or ii) artificial stress term discussed in the following section to avoid some numerical issues of the algorithm.

6.2.2 Elastic-plastic solid

In this work, another approach considered for the modelling of the soil in the SPH framework is one based on solid mechanics. The goal is to include lineal terms (elastic deformation) using Hooke's law for the stress tensor and to describe the non-diagonal terms of the stress tensor by a yielding relation (e.g. Drucker-Prager used here), when beyond the elastic limit (i.e. for permanent deformation) [34]. Starting from the equilibrium equation, the partition of the total Cauchy stress tensor (assumed in the context of infinitesimal strain theory) for the soil consists of two parts: i) the isotropic pressure and ii) the deviatoric shear stress,

$$\boldsymbol{\sigma} = -p\mathcal{I} + \boldsymbol{\sigma'}. \tag{6.11}$$

The pressure is normally derived from the equation of state as described in section 2.2.5 and the incremental form of the deviatoric stress–strain relationship in the solid mechanics framework can be represented as the constitutive model given by,

$$\dot{\boldsymbol{\sigma}}' = 2G\dot{\boldsymbol{\gamma}}, \tag{6.12}$$

where, $\dot{\boldsymbol{\sigma}}'$ is the deviatoric stress rate (the '.' on top of the deviatoric shear stress $\boldsymbol{\sigma}'$ denotes the time derivative), G is the shear stress modulus and $\dot{\boldsymbol{\gamma}}$ is the deviatoric strain rate. This strain rate relationship considers the small strain tensor (implying that actually rotations that need to be small, not the strains themselves). But when considering velocities gradients rather that deformation (displacements) gradients it is possible to account for the extra terms directly related to the rate of rotation of an object as the velocity gradient is a calculation over an infinitesimal time step and during this time step, an object's orientation and level of strain only changes by an infinitesimal amount hence, using small time steps increments it is possible to consider for large finite rigid body rotations of the stress. The full velocity gradient can be written as

$$\mathcal{L} = \mathcal{D} + \mathcal{W} = \frac{1}{2}\left(\nabla\mathbf{u} + (\nabla\mathbf{u})^T\right) + \frac{1}{2}\left(\nabla\mathbf{u} - (\nabla\mathbf{u})^T\right), \tag{6.13}$$

where, the second term, $\mathcal{W}$ represents the antisymmetric (velocity gradient) tensor, which is directly related to the rate of rotation of an object, but not its deformation at all. The stress-strain relationship of the Hooke's deviatoric stress rate (6.12), in SPH formulation can be expressed as,

$$\frac{D\boldsymbol{\sigma}'_{\boldsymbol{a}}}{Dt} = 2G\left(\dot{\epsilon^{ij}} - \frac{1}{3}\delta^{ij}\dot{\epsilon^{ij}}\right) - \dot{\Omega^{ik}}\boldsymbol{\sigma}'^{kj}_{\boldsymbol{a}} + \boldsymbol{\sigma}'^{ik}_{\boldsymbol{a}}\dot{\Omega^{jk}}, \tag{6.14}$$

where, δ^{ij} is the Kronecker delta, $\dot{\epsilon}$ and $\dot{\Omega}$ are respectively, the strain and rotation rate tensors. The previous relation for the deviatoric stress rate tensor is derived considering the following,

$$\overset{o}{\boldsymbol{\sigma}} \;=\; \dot{\boldsymbol{\sigma}} - \mathcal{W}\cdot\boldsymbol{\sigma} + \boldsymbol{\sigma}\cdot\mathcal{W} \;=\; 0 \qquad \text{when} \qquad \mathcal{D} = 0 \tag{6.15}$$

where, $\overset{o}{\boldsymbol{\sigma}}$ is the Jaumann derivative of the Cauchy stress, and $\dot{\boldsymbol{\sigma}}$ is its time derivative. This objective stress rate form is needed since the Cauchy stress and rate of deformation tensor behave incompatibly (i.e. constitutive equations should be frame indifferent – objective) in the presence of rigid body rotations.

Also, the strain and rotation rate tensors are defined in terms of the coordinates directions and expressed in SPH formulation as,

$$\begin{aligned}\dot{\epsilon^{ij}} = \mathcal{D} = \frac{1}{2}\left(\frac{\partial\mathbf{u}^i}{\partial x^j} + \frac{\partial\mathbf{u}^j}{\partial x^i}\right) &= \frac{1}{2}\left[\sum_b \frac{m_b}{\rho_b}(\mathbf{u}^i_b - \mathbf{u}^i_a)\nabla_a W_{ab}\right] \\ &+ \left[\sum_b \frac{m_b}{\rho_b}(\mathbf{u}^j_b - \mathbf{u}^j_a)\nabla_a W_{ab}\right], \end{aligned} \tag{6.16}$$

$$\begin{aligned}\dot{\Omega^{ij}} = \mathcal{W} = \frac{1}{2}\left(\frac{\partial\mathbf{u}^i}{\partial x^j} - \frac{\partial\mathbf{u}^j}{\partial x^i}\right) &= \frac{1}{2}\left[\sum_b \frac{m_b}{\rho_b}(\mathbf{u}^i_b - \mathbf{u}^i_a)\nabla_a W_{ab}\right] \\ &- \left[\sum_b \frac{m_b}{\rho_b}(\mathbf{u}^j_b - \mathbf{u}^j_a)\nabla_a W_{ab}\right]. \end{aligned} \tag{6.17}$$

From (6.14) the change of deviatoric stress due to deformation of the solid body can be obtained and the resulting momentum equation for the soil phase becomes,

$$\frac{D\mathbf{u_a}}{Dt} = \sum_b m_b \left(\frac{\boldsymbol{\sigma}_{\boldsymbol{a}}^{ij}}{\rho_a^2} + \frac{\boldsymbol{\sigma}_{\boldsymbol{b}}^{ij}}{\rho_b^2} + R_{ab}^{ij} f_{ab}{}^n \right) \nabla_a W_{ab}, \tag{6.18}$$

where the last term inside the parenthesis represents a stabilisation term optionally utilised to keep the simulation stable in SPH solid mechanics [57]. This artificial stress term acts as a repulsive force between particles which is increased when the separation between particles decreases and is considered to remove a well known spurious phenomenon called the tensile instability,

$$f_{ab} = \frac{W_{ab}}{W(\|\mathbf{r}_0\|)}, \qquad \text{and} \qquad R_{ab}^{ij} = R_a^{ij} + R_b^{ij}. \tag{6.19}$$

f_{ab} represent a scaling function defined by the ratio of the smoothing function values for the actual distance between the pair of particles and their initial spacing and R is defined, for each particle such that

$$R_a^{ij} = \begin{cases} -\epsilon \frac{\boldsymbol{\sigma}_{\boldsymbol{a}}^{ij}}{\rho_a^2} & \text{if} \qquad \boldsymbol{\sigma}_{\boldsymbol{a}}^{ij} > 0, \\ 0 & \text{otherwise}, \end{cases} \tag{6.20}$$

the strength of this force is controlled by the exponent n and the factor ϵ. The values suggested by Monaghan [69] are $\epsilon = 0.2$ and $n = 4$, in which case the force is sufficient to improve the particle spacing without degrading the accuracy of the SPH method.

This previous elastic solid model described in equation 6.14 can be extended and these shear stress components should be restricted to the failure surface when plastic strain takes place. This plastic behaviour can be introduced in the equations using a yielding criterion, such as the Drucker-Prager. Yield will occur at a particle when some combination of the stress components (usually invariants of the principal and/or deviatoric stress which are independent of material orientation) reaches some critical value

$$f_Y\left(I_1, J_2, J_3\right) = m, \tag{6.21}$$

where, m some material property which can be determined experimentally (e.g. yield stress in tension) and f_Y is a yield potential function (e.g. Drucker-Prager condition) that will dictate when plastic deformation will occur computed from,

$$f_Y\left(I_1, J_2\right) = \sqrt{J_2} - A\frac{1}{3}I_1 - B, \tag{6.22}$$

where, $I_1 = tr(\boldsymbol{\sigma})$ is the first invariant of the stress tensor, $\boldsymbol{\sigma}$ and $J_2 = \frac{1}{2}\boldsymbol{\sigma'}_{ij}\boldsymbol{\sigma'}^{ij}$ represents the second invariant of the deviatoric stress tensor, $\boldsymbol{\sigma'}$. The dimensionless constants A and B are determined from experiments and in the case of soil models, they are related to the cohesion, c and the angle on internal friction, θ. The flow rule for plastic strain is represented as

$$\dot{\boldsymbol{\gamma}}_{\boldsymbol{p}} = \dot{\lambda}\frac{\partial g}{\partial \boldsymbol{\sigma}} \qquad \text{if} \qquad \dot{\lambda} > 0, \tag{6.23}$$

where, $\dot{\boldsymbol{\gamma}}_{\boldsymbol{p}}$ is the plastic strain rate tensor, $\dot{\lambda}$ is the rate form of a plastic multiplier (dependent on the state of stress and load history) and g is the plastic potential function that when the yield surface (described before for the Drucker-Prager model in (6.22)) coincides with the plastic potential surface, the yield function can act as the plastic potential function. Accordingly, the plastic deformation will occur only if the following yield criterion is satisfied,

$$f_Y\left(I_1, J_2\right) = g = \sqrt{J_2} - A\frac{1}{3}I_1 - B = 0. \tag{6.24}$$

Note that a plastic multiplier $\dot{\lambda} = 0$ corresponds to elastic or plastic unloading.

The extended – from (6.14) – stress-strain relationship (of the total stress tensor) for the current elastic-plastic soil model, at particle **a**, can be expressed as,

$$\begin{aligned}\frac{D\boldsymbol{\sigma}_{\boldsymbol{a}}}{Dt} &= 2G\left(\dot{\epsilon}^{ij} - \frac{1}{3}\delta^{ij}\dot{\epsilon}^{ij}\right) + K\delta^{ij}\dot{\epsilon}^{kk} \\ &\quad - \dot{\Omega}^{ik}\boldsymbol{\sigma}_{\boldsymbol{a}}^{kj} + \boldsymbol{\sigma}_{\boldsymbol{a}}^{ik}\dot{\Omega}^{jk} - \dot{\lambda}\left[\left(K - \frac{2G}{3}\right)\frac{\partial g}{\partial \boldsymbol{\sigma}_{\boldsymbol{a}}^{mn}}\delta^{mn}\delta^{ij} + 2G\frac{\partial g}{\partial \boldsymbol{\sigma}_{\boldsymbol{a}}^{ij}}\right],\end{aligned} \tag{6.25}$$

where, m, n are dummy indexes and K is the elastic bulk modulus. Once the yield function and the plastic potential function are specified for a particular material of interest (e.g. Drucker-Prager yield criterion) and total strain rate tensor is prescribed, the rate of change of plastic multiplier can be then obtained. In the case of an associated plastic flow rule (i.e. which indicates that the plastic potential function of the Drucker-Prager material has the same form with the yield criterion), the the final stress-strain relationship of the Drucker-Prager elastic-perfectly plastic soil model can be expressed as

$$
\begin{aligned}
\frac{D\boldsymbol{\sigma_a}}{Dt} &= 2G\left(\dot{\epsilon}^{ij} - \frac{1}{3}\delta^{ij}\dot{\epsilon}^{ij}\right) + K\delta^{ij}\dot{\epsilon}^{kk} \\
&\quad - \dot{\Omega}^{ik}\boldsymbol{\sigma_a}^{kj} + \boldsymbol{\sigma_a}^{ik}\dot{\Omega}^{jk} - \dot{\lambda}\left[3AK\delta^{ij} + \frac{G}{\sqrt{J_2}}\boldsymbol{\sigma'_a}^{ij}\right]. \qquad (6.26)
\end{aligned}
$$

Numerical errors in the computation of the plasticity of the soil constitutive model described in this study are also taken into consideration. A correction for a yield surface drift meaning when an elastic-perfectly plastic material experiences plastic deformation, the stress state could lie outside the yield surface during plastic loading. In such cases, a stress-scaling back procedure is adopted to return the stress state to the yield surface. For the Drucker-Prager, the scaling factor is applied past yielding after few iterations and it has the following expression

$$
r^n = \frac{-A\frac{1}{3}{I_1}^n - B}{\sqrt{{J_2}^n}}. \qquad (6.27)
$$

For further details refer to Bui et al. [11].

6.3 Notes on implementation

6.3.1 Time integration

In regards to the numerical implementation of the semi-discrete equations described before in section 2.2.5 together with the soil stress-strain relationships presented in this chapter, an appropriate time integration scheme is required. Standard techniques such as leapfrog, predictor-corrector and runge-kutta (RK) methods can be use to integrate the field variables at every particle [107]. In this thesis, a leapfrog time integration scheme is chosen and frequently used in particle simulation algorithms because of its explicit nature, making it simple to code in the computational sense, also offers a second-order accuracy in time and it is symplectic, which means that it conserves certain properties (i.e. energy conservation) of dynamical systems. Leapfrog integration updates the velocities on half steps and the positions on integer steps. The whole time step is given below,

$$\mathbf{u}^{n+\frac{1}{2}} = \mathbf{u}^{n-\frac{1}{2}} + \frac{D\mathbf{u}}{Dt}^{n}\Delta t, \tag{6.28}$$

$$\mathbf{r}^{n+1} = \mathbf{r}^{n} + \mathbf{u}^{n+\frac{1}{2}}\Delta t. \tag{6.29}$$

An alternative form used where variable time stepping is required,

$$\mathbf{u}^{n+\frac{1}{2}} = \mathbf{u}^{n} + \frac{D\mathbf{u}}{Dt}^{n}\frac{\Delta t}{2}, \tag{6.30}$$

$$\mathbf{r}^{n+1} = \mathbf{r}^{n} + \mathbf{u}^{n+\frac{1}{2}}\Delta t, \tag{6.31}$$

$$\mathbf{u}^{n+1} = \mathbf{u}^{n+\frac{1}{2}} + \frac{D\mathbf{u}}{Dt}^{n+1}\frac{\Delta t}{2}. \tag{6.32}$$

In this scheme the field variables and positions of particle are updated at half a time step $(n+\frac{1}{2})$ by using the following equations,

$$\begin{cases} \rho_a^{n+\frac{1}{2}} = \rho_a^{n-\frac{1}{2}} + \Delta t(\frac{D\rho_a}{Dt})^n, \\ \mathbf{u_a}^{n+\frac{1}{2}} = \mathbf{u_a}^{n-\frac{1}{2}} + \Delta t(\frac{D\mathbf{u_a}}{Dt})^n, \\ \boldsymbol{\sigma_a}^{n+\frac{1}{2}} = \boldsymbol{\sigma_a}^{n-\frac{1}{2}} + \Delta t(\frac{D\boldsymbol{\sigma_a}}{Dt})^n, \\ \mathbf{r_a}^{n+1} = \mathbf{r_a}^{n} + \Delta t\hat{\mathbf{u_a}}^{n+\frac{1}{2}}, \end{cases} \tag{6.33}$$

where, $\hat{\mathbf{u_a}} = \frac{D\mathbf{r_a}}{Dt}$ represents the average velocity of the particle.

The pressure p is linked to the density via the equation of state (EOS) (2.31). Note that the density of a particle also could be calculated from the mass of neighbouring particles with equation (2.29) but then a particle near the free surface would miss the contribution of particles above the free surface and the density would become too low. The calculation via the integration of the time derivative of the density is preferable as it does not lead to densities that are too low at the free surface [68].

In the above expressions n indicates the current time t; and $(n+1)$ indicates the advanced time $(t+\Delta t)$. The time step Δt needs to be limited for stability purposes. The time step is taken as a variable time step controlled by the Courant-Friedrichs-Levy (CFL) condition,

$$\Delta t_{max} = C_{CFL}\min(\Delta t_{CFL}, \Delta t_F), \tag{6.34}$$

where, C_{CFL} is an specified CFL coefficient value, usually 0.2,

$$\Delta t_{CFL} = \min_i \left\{ \frac{h}{c} \right\}, \tag{6.35}$$

represents a time step based on the sound speed of the media c and,

$$\Delta t_F = \min_i \left\{ \sqrt{\frac{h}{\|\frac{D\mathbf{u}_i}{Dt}\|}} \right\}, \tag{6.36}$$

which connects the time step with the particle acceleration and is useful to prevent overshoot of particles in a single time step between decomposed domains (as will be explained in the parallelisation section below) [4]. More time step criteria can be considered depending of the physics of the problem to be explored.

6.3.2 Link list

A key component of any Lagrangian method is the neighbour search algorithm. To calculate a smoothed value of a property of a particle in SPH form, information from its neighboring particles is needed. In the worst case, if each particle has to interact with all others N particles, the computational time scales as $\mathcal{O}(N^2)$ and this would decrease the practicality of SPH simulations. The reason why finite compact support is introduced in the definition of the smoothing kernel (see 2.2.5) is to constrain the radius/sphere of action that each particle can affect their neighbours particles, $N_{neighbour}$. In this way, the number of calculation per time step and computational time would diminish considerably to approximately $\mathcal{O}(N \cdot N_{neighbour})$, assuming that the number of neighbours is the same for every particle in the domain. In practice, to perform this sweeping of particles around a neighbourhood, a procedure known as the linked-cell grid method is utilised. At every time step all the particles are binned into cells of side length equal to the radius of the kernel function, so that all neighbouring particles are binned in the surrounding cells. The domain is divided into cells with side length of radius of kernel function $2h$, therefore only need to search the current cell and neighbouring cells [72]. When searching the neighbouring particles, only the surrounding cells need to be checked, with considerable saving in computation time. To avoid double counting (i.e. while checking a's neighbours we see b and while checking b's neighbours we see a) only certain neighbouring cells are checked following a topological stencil structure in 2D and 3D [4].

6.3.3 Initial and boundary conditions

Many types of initial and boundary conditions implementations exist in the literature for SPH [108]. In terms of (fluid) particles that come close to contact with a closed boundary, for example a wall, its properties (like density) should not change and they are called closed boundaries. Traditionally, the boundary particles with repulsive forces have been used for particles which approach the wall boundary [91]. Lennard-Jones-type potential are often used which are analogous to the repulsive force between two molecules. An expression of the boundary force based on the distance (i.e. along the centreline of the fluid and boundary particle) between particles was presented by Monaghan [67],

$$f(\mathbf{r}_{ab}) = \begin{cases} D\left(\left(\frac{\|\mathbf{r}_0\|}{\|\mathbf{r}_{ab}\|}^{12}\right) - \frac{\|\mathbf{r}_0\|}{\|\mathbf{r}_{ab}\|}^{4}\right)\frac{\mathbf{r}_{ab}}{\|\mathbf{r}_{ab}\|^2} & \text{if} \quad \|\mathbf{r}_{ab}\| \leq \|\mathbf{r}_0\|, \\ 0 & \text{if} \quad \|\mathbf{r}_{ab}\| > \|\mathbf{r}_0\|, \end{cases} \tag{6.37}$$

where D, is a problem parameter chosen considering the physical configuration, e.g. problems involving dams, bores, weirs. The distance $\|\mathbf{r}_0\|$, represents a cut-off usually selected to be approximately equal to the initial particle spacing. The Lennard-Jones potential formulation for repulsive forces avoids particle penetration into the boundary, ensuring that the velocity component normal to the boundaries vanishes. However, this (i.e forces acting normal to the wall) can be a drawback since the particles moving parallel to the boundary are subjected to a non-uniform normal force leading to ripples in the flow near the wall which also make it difficult to capture shear stresses due to velocity gradients near the wall. Because of this, some work [71] has been done to actually calculate a boundary force approach in which the forces from neighbouring boundary particles should give rise to a force normal to the boundary and in this way the boundary experience a constant repulsive boundary force. Unfortunately, another problem arises in regards of the complicated calculation of the outward normal to a surface and particularity in corner particles situations where ambiguity may be present. Latest work [70], has been proposed to adopt repulsive boundary forces with radial direction which removes the need of computing the outward unit normals to the boundaries.

Another alternative in regards to the repulsive forces on fluid particles, which is the preferred choice for this work, is that instead of using a real line of boundary particles that exerts forces on the fluid, an imaginary set of particles (i.e. ghost particles) outside of boundary symmetric to the inside fluid particles is used. The main idea behind these ghost particles are that when a fluid particle is coming within the influence domain, e.g. $2h$ of a closed boundary, an identical ghost particle is mirrored at the other side of the boundary. These particles are a reflection of the real (fluid) particle in the sense that they have the same density and pressure as the corresponding fluid particles, but an opposite velocity $-\mathbf{u}$, ensuring that the smoothed velocity field, $\mathbf{u}$ goes to zero at the domain boundaries (i.e no-slip condition) [52]. Additionally, the reflected particles can also be given the same tangential velocity with the mirrored particle but opposite normal velocity thereby producing free slip boundary conditions. This approach has the advantages to restore the SPH consistency (it can require larger time steps to ensure stability) near the boundaries and to prevent non-physical penetration through the solid boundary, has a better ability to capture shear stresses and surface tension if needed, but it requires extra computational effort in regards to the generation of these virtual particles [4].

In terms of the inlet and outlet initial or boundary conditions, referred as an open boundary where the fluid can flow in or out the model. Open boundaries are normally implemented using periodic boundary conditions in which particles near an open boundary interact with the particles near the complementary open boundary on the other side of the domain

[101]. In this way the kernel support/area of influence extends beyond the open boundary and continued through the opposite open boundary so that particles interaction is sustained. A periodic boundary is a good way to model an open boundary without disturbing the fluid, but unfortunately it can only be applied to a limited number of cases. Generally, at an open boundary only one parameter can be fixed, either the velocity, or the pressure but to put particles in the system in the correct way, one needs both position and velocity of each particle. Some ideas to solve these demands are to impose the inflow/outflow velocity conditions driven by true Dirichlet boundary conditions of the projected pressure field [40, 45].

6.3.4 Load balancing and parallelisation

The computation of SPH model can be benefit from parallelisation. The message-passing interface (MPI) parallel programming model is used in this SPH implementation where each processor has its own private memory and smaller sub-regions are assigned to separate processors, which complete the task independently. In parallel code, the whole computational domain is decomposed into sub-domains or blocks and assigned to each processor. Every processor deal with its own block. After domain decomposition, each cell of the linked-cell grid needs to check for its neighbouring cells so the exterior or outermost cells of that block for each process should be able to communicate and exchange information at each time step between neighbouring processes, so for that reason buffer arrays in overlapping regions are created to transfer data between these edge cells. The sizes of the blocks are determined via load balancing in order to ensure that each processor has roughly the same number of particles. The shape of the blocks is periodically resized based generically on a ratio of the total number of particle in every block to the total number of processors.

6.4 Numerical results and discussion

6.4.1 Simulation configuration

In this section, the test case from section 4.4 in chapter 4 for a current-induced scour simulation around a two-dimensional (2D) circular cylinder (horizontal pipeline) which was validated against experiments and numerical results from [51] is recycled for the purposes of testing the SPH multiphase (water-sediment) framework.

6.4.2 Discussion

The work shown in this chapter while is work-in-progress it continues to explore the possibilities of SPH as a tool for modelling in geotechnical engineering particularly local scour around hydraulic structures.

In figure 6.1 a representative example is used to illustrate the capabilities of SPH modelling of scour around a structure using a viscoplastic model consisting of two fluid phases (i.e. water and soil). It is observed that although the flow (phase) direction is disturbed by the presence of the structure (circular cylinder), there is an initial difference between these results and those reported in the previous methodologies (refer to chapter 4). These current analyses showed higher soil (phase) deformations and it is speculated that the difference is due to the assumptions in the treatment of the soil particles as a non-Newtonian viscous fluid. Regarding in the context of sediment transport modelling, the viscoplastic approach is generally well adapted for highly dynamic responses but may exhibit severe limitations regarding small strain-rates and deformations [7], meaning that regions with low stresses may underestimate the bed profile during the scour process as noticed in areas close to the circular cylinder gap where an abrupt change of the scour hole is observed in frames (*c*) and (*e*), instead of a gentle downslope featured in the upstream region. Although this approach is suitable to simulate scour of soil, the material non-linear behaviour of soil may not be accurately modelled compared to an approach using a material (i.e. soil) constitutive model in a solid mechanics framework. The significant issues observed with the overestimation of the soil deformations are partially related to the interaction model of the particles which reside in the interface water-sediment layer. This can be achieved in the simplest way by a balancing of strain-rate gradient across the interface with an weighted arithmetic mean between the different effective viscosities in the phases but other techniques consider modelling the interface between water and soil introducing fictitious suspension layers depending on the concentration of soil [100]. Further studies are required to calibrate this approach and study the post-yield strain-rate dependence of the soil. Additionally, it is noted that the Herschel-Bulkley model, which combines the Bingham plastic model for modelling the plastic forces along with the power-law mode shows a better compactness of the soil at the formation of the downstream bedforms evidenced in the lesser particle splatter in the cusp of the deposited sediment mount.

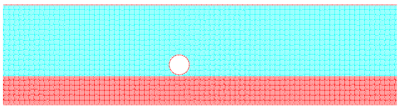

(a) SPH simulation, fluid phase (blue) and soil phase (red) at $t = 0$ sec.

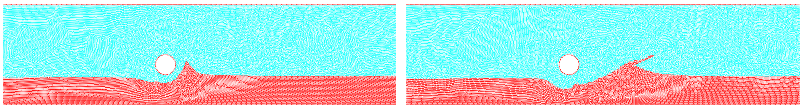

(b) Bingham soil phase (red) $t = 5$ sec.

(c) Bingham soil phase (red) $t = 10$ sec.

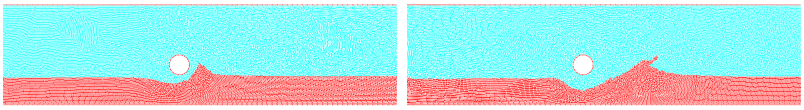

(d) Herschel-Bulkley soil phase (red) at $t = 5$ sec.

(e) Herschel-Bulkley soil phase (red) at $t = 10$ sec.

Figure 6.1: SPH visualisations for the non-Newtonian soil material simulation.

In the present work the description of the existing implementation of the elastic-plastic solid SPH model (see section 6.2.2) was presented and an initial numerical test was performed to analyse its applicability in a current-induced local scour around a structure with a circular cross-section and particularly the interaction in the water-sediment interface. In figure 6.2, preliminary results showed compatibility issues between the liquid and the solid mechanics models producing interpenetration between phases (solid and liquid). These are managed via the viscous force interactions on the liquid state and repulsion forces based on the distance apart similar to the boundary condition treatment with solid boundaries. The solid state requires a balance in the repulsion which can be difficult to achieve but managed finding a small enough Courant number. In contrast with the previous viscoplastic simulations, each phase (the liquid/water and the non-Newtonian liquid/soil) can handle a viscosity parameter which makes more manageable the control of the numerical stability at the interface boundary.

(a) Particle colours: fluid phase (●) and soil phase (●) at $t = 10$ sec.

Figure 6.2: SPH visualisations for the elastoplastic soil material simulation.

The Drucker-Prager model was selected as the yield criterion in the elastic-plastic approach because of its suitability for materials such as rock or soils. It is a smoothed version of the Mohr-Coulomb yield surface, whereby the hydrostatic-dependent first invariant I_1 is introduced to the Von Mises criteria which is independent of hydrostatic pressure and more suitable for the modelling of plasticity in metals. The Drucker-Prager's yield criterion is thus a pressure-dependent model and the failure occurs when the shear stress second invariant square root $\sqrt{J_2}$ reaches the following yield stress,

$$\tau_0 = \frac{2\sqrt{3}sin\theta}{(3 - sin\theta)} p_{eff}, \tag{6.38}$$

where the effective pressure p_{eff} is defined as:

$$p_{eff} = p - p_{pw}, \tag{6.39}$$

with p_{pw} being the pore water pressure. This pore pressure affects the effective stress behaviour effect on the yield criterion. According to Terzaghi's principle, the pore water pressure exerts stresses isotropically, and decomposing the Cauchy stress tensor in,

$$\boldsymbol{\sigma} = \boldsymbol{\sigma}_{eff} - p_{pw}\mathcal{I}, \tag{6.40}$$

allows the effective stress to be written in matrix form as,

$$\boldsymbol{\sigma}_{eff} = \begin{pmatrix} \boldsymbol{\sigma}_1 + p_{pw} & 0 & 0 \\ 0 & \boldsymbol{\sigma}_2 + p_{pw} & 0 \\ 0 & 0 & \boldsymbol{\sigma}_3 + p_{pw} \end{pmatrix}.$$

As a consequence, the effect of the effective pressure needs to be properly evaluated in the case of a saturated and submerged material by subtracting the pore pressure (assumed to be hydrostatic for simplicity) in the

Drucker-Prager model as otherwise, the water pressure above the submerged soil might always stop the yielding. This translates into including a term of pore water pressure to the general momentum equation in SPH method for saturated soil problems such as soil-water coupling. The pore water pressure for soil is calculated from solving the SPH discretization of the gradient of the pore-water pressure for the soil model [10]. In the future work section 7.2 a comment about this next implementation detail will be addressed.

Chapter 7

Conclusions and future work

Contents

7.1 Summary of the present study

Based on the published literature for single-phase, mesh-based approaches to model local sediment scour, the use of mesh deformation methods (i.e. r-adaptive moving meshes) for updating the mesh in response to boundary movement (representing morphology changes) can often result in excessive mesh distortion. This invariably leads to deterioration of numerical solution quality and even to blow up. This present work sought to address this issue with and to the best of the author's knowledge, the first demonstrated approach combining robust mesh movement methods within an arbitrary Lagrangian-Eulerian (ALE) framework along with anisotropic adaptive mesh refinement. This new hr-adaptive approach was described in detail in chapter 4, robustly demonstrated on a geometrically challenging two-dimensional problem involving significant local scour of well-graded loose sands around a horizontal pipe and further tested in a more complex three-dimensional problem in chapter 5. From the range of techniques available for introducing mesh adaptivity, h-adaptive or mesh optimisation methods were applied, in which the shape and size of mesh elements are improved through a series of topological operations dictated by an error metric.

The sediment transport rate, $\mathbf{q_t} = \mathbf{q_b} + \mathbf{q_s}$, includes not only the transport of bed load $\mathbf{q_b}$, but also of suspended load $\mathbf{q_s}$. Although the aspect of bed load transport is relatively well understood with the ideas of excess bed shear stress-based empirical formulae, there are debates about how to express the shear velocity at the bottom of the channel given that the local fluid velocities are difficult to measure directly, and averaged flow speeds are often used instead. Most (commercial) codes developed for the numerical modelling of sediment transport with dynamic bathymetry are based on a mathematical model consisting of the depth-averaged (two-dimensional) shallow water equations (SWE) coupled with the bed morphology model (i.e. Exner equation). This work presented a more accurate strategy by coupling the full Navier-Stokes model with a morphological module in a manner which links the friction velocity to the tangential wall shear stress at the boundary of the computational domain using near-wall modelling for turbulent flows with the help of a conceptually different wall function implementation as described in chapter 3.

The limitations of using a $k - \epsilon$ model for turbulent modelling represented a challenge in the capture of near-field unsteady flow features in the scouring simulations, as evidenced especially in the three-dimensional results from chapter 5, resulting in possible underestimation of the bed shear stress amplification factors.

In the context of multi-phase modelling with SPH, the idea of simulating soil as a viscous (strain-rate dependent) fluid where a Bingham type constitutive model is proposed based on Mohr-Coulomb yield-stress criterion, and the viscosity is derived from the cohesion and friction angle as presented in chapter 6, has been demonstrated here with preliminary results that are applicable to the scour problem. A second approach where the soil phase is modelled as an elastic-plastic material with deformation with constitutive equations based upon Hooke's law of linear elasticity and Drucker-Prager yield criterion is also a feasible and probably more accurate method, but some modifications (i.e. hydrostatic pore-water pressure) needed to be included in the current implementation presented in this work in order to robustly apply it to industrial (e.g. scour) problems. In future numerical studies, SPH models could be used to deliver full scale models so that the scour and erosion around more complex hydraulic structures can be investigated under realistic conditions.

7.2 Recommendations for future research

- In both chapters 3 and 5, difficulties in handling swirling flows were emphasised, for example the (three-dimensional) horseshoe vortex with turbulence parametrisation using a two-equation model (i.e. $k - \epsilon$) due to rapid changes of flow (particularly high-Re) not being able to be captured. Although the conventional wall functions can be used with fine near-wall meshes, some might not be able to account for the low-Reynolds-number effects in the laminar/viscous sublayer. Future work could consider different strategies that could be used as alternatives such as Reynolds Stress-based model (RSM) or Large eddy simulation (LES) to handle anisotropic turbulence that an eddy-viscosity model will not take into account.

- A key limitation in this work that would be seen in the real world, which has been not considered is the externally-generated turbulence on the sediment transport classic formulations. This effect consists in investigate the influence of turbulence-driven external flow features (i.e. horseshoe vortex and/or other lee-wake flow processes formed around the hydraulic structure) on the bedload and suspended-load sediment transport, therefore the sediment transport descriptions need to be modified to account for this additional externally-generated turbulence effect. Studies with this consideration have shown in their results (particularly in 3D) that the scour depth increases and time scale decreases when the effect of externally-generated turbulence is incorporated in the calculations [20].

- As discussed in chapter 6, the SPH solid model based on elastic-plastic constitutive model for soil was initially implemented and tentatively tested but presented some immediate issues that need to be addressed in the current implementation available in `https://github.com/ImperialCollegeLondon/sph` (supervised by Prof. Stephen Neethling), in regards to the error if the gradient of pore water pressure is not included using the standard SPH formulation.

Amongst further topics to explore in the modelling of sediment transport through granular flow in SPH, there is the consideration that generally the elastoplastic constitutive model for soil with Drucker-Prager yield function is mainly developed for cohesionless soils. However, most soils show cohesion to some extent and this brings the challenge of solving the fluid flow through the porous medium. In this previous approach, water flow (i.e. seepage) through the porous medium is also neglected but the interactions between solid soil particles and water calculated by means of the seepage force, could be integrated via introducing them into the momentum equation as an external force.

Also, granular flow (i.e. soil phase) by itself is a multi-phase problem and ideally considers the fluid-solid interactions as well as the collisions and deformation processes which can be accurately modelled directly using the discrete element method (DEM). With the continuum assumption made in the approaches discussed in chapter 6, the forces between the grains nor their individual displacement are neither considered, but the stress field and the strain field within the continuous material [94]. Such a model is beyond the scope of this thesis but it is a interesting project for future research.

Bibliography

[1] Applied Modelling and Computational Group. *Fluidity Manual Version 4.1.12.* Department of Earth Science and Engineering, Imperial College London, 2015.

[2] D. D. Apsley and P. K. Stansby. Bed-Load Sediment Transport on Large Slopes: Model Formulation and Implementation within a RANS Solver. *J. Hydraulic Eng.*, 10:1440–1451, 2008.

[3] M. Bakroon, R. Daryaei, D. Aubram, and F. Rackwitz. Multi-material arbitrary lagrangian-eulerian and coupled eulerian-lagrangian methods for large deformation geotechnical problems. *Proceedings of the 9th European Conference on Numerical Methods in Geotechnical Engineering (NUMGE 2018)*, 07 2018.

[4] D. J. Barker. *The application of smoothed particle hydrodynamics to the simulation of multiphase flows through packed beds.* PhD thesis, Imperial College London, London, UK, 2014.

[5] F. Bassi and S. Rebay. A high-order accurate discontinuous finite element method for the numerical solution of the compressible

Navier-Stokes equations. *J. Comput. Phys.*, 131:267–279, 1997.

[6] C. Baykal, B.M. Sumer, D.R. Fuhrman, N.G. Jacobsen, and J. Fredsøe. Numerical investigation of flow and scour around a vertical circular cylinder. *Philos. Trans. A Math. Phys. Eng. Sci.*, 28, 2015.

[7] C. R. Beverly and R. I. Tanner. Numerical analysis of three-dimensional bingham plastic flow. *J. of non-newtonian fluid mechanics*, 41:85–115, 01 1992.

[8] B. Brørs. Numerical modeling of flow and scour at pipelines. *J. Hydraulic Eng.*, 125(5):511–523, 1999.

[9] C. J. Budd, W. Huang, and R. D. Russell. Adaptivity with moving grids. *Acta Numerica.*, 18:111–241, 2009.

[10] H. Bui and R. Fukagawa. An improved sph method for saturated soils and its application to investigate the mechanisms of embankment failure: Case of hydrostatic pore-water pressure. *International Journal for Numerical and Analytical Methods in Geomechanics*, 37:31–50, 01 2011.

[11] H. H. Bui, R. Fukagawa, K. Sako, and S. Ohno. Lagrangian meshfree particles method (SPH) for large deformation and failure flows of geomaterial using elastic-plastic soil constitutive model. *International Journal for Numerical and Analytical Methods in Geomechanics*, 32(12):1537–1570, 08 2008.

[12] G. C. Buscaglia and E. A. Dari. Anisotropic mesh optimization and its application in adaptivity. *International Journal for Numerical Methods in Engineering*, 40(22):4119–4136, 1997.

[13] C-CORE. Design options for offshore pipelines in the US Beaufort and Chukchi seas. Technical report, 2008.

[14] M. J. Castro-Diaz, F. Hecht, B. Mohammadi, and O. Pironneau. Anisotropic unstructured mesh adaption for flow simulations. *International Journal for Numerical Methods in Fluids*, 25(4):475–491, 1997.

[15] P. A. Cavallo, A. Hosangadi, R. A. Lee, and S. M. Dash. Dynamic unstructured grid methodology with application to aero/propulsive flow fields. *AIAA Fluid Dynamics and co-located Conferences, 15th Applied Aerodynamics Conference*, 1997.

[16] P. A. Cavallo and S. Neeraj. Parallel unstructured mesh adaptation for transient moving body and aeropropulsive applications. *AIAA Paper Fluid Dynamics and co-located Conferences*, 2004.

[17] K. Y. Chien. Predictions of channel and boundary-layer flows with a low-reynolds number turbulence model. *American Institute of Aeronautics and Astronautics*, 20:33–38, 1982.

[18] B. Cockburn, G. E. Karniadakis, and C. W. Shu. *Discontinuous Galerkin Methods: Theory, Computation and Applications*. Springer Publishing Company, Incorporated, 1st edition, 2011.

[19] C. J. Cotter, D. A. Ham, and C. C. Pain. A mixed discontinuous/continuous finite element pair for shallow-water ocean modelling. *Ocean Model.*, 26(1–2):86–90, 2009.

[20] M. Dixen, B. Sumer, and J. Fredsøe. Numerical and experimental investigation of flow and scour around a half-buried sphere. *J. Coastal Engineering*, 73:84–105, 03 2013.

[21] J. Donea, A. Huerta, and J. P Ponthot. Arbitrary Lagrangian Eulerian methods. In *Encyclopedia of Computational Mechanics*, chapter 14. Wiley & Sons, 2004.

[22] F. Engelund and J. Fredsøe. A sediment transport model for straight alluvial channels. *Nordic Hydrology.*, 125(5):293–306, 1976.

[23] H. Fadaifard and J. L. Tassoulas. Numerical modeling of coupled seabed scour and pipe interaction. *International Journal of Solids and Structures*, 51(19):3449 – 3460, 2014.

[24] C. Farhat, C. Degand, B. Koobus, and M. Lesoinne. Torsional springs for two-dimensional dynamic unstructured fluid meshes. *Computer Methods in Applied Mechanics and Engineering.*, 163(1-4):231–245, 1998.

[25] P. E. Farrell and J. R. Maddison. Conservative interpolation between volume meshes by local Galerkin projection. *Comput. Methods Appl. Mech. and Eng.*, 200:89 – 100, 2011.

[26] P. E. Farrell, M. D. Piggott, C. C. Pain, G. J. Gorman, and C. R.

Wilson. Conservative interpolation between unstructured meshes via supermesh construction. *Computer Methods in Applied Mechanics and Engineering.*, 198(33):2632 – 2642, 2009.

[27] J. Fredsøe. On the development of dunes in erodible channels. *J. Fluid Mechanics.*, 64:1–16, 1974.

[28] P J Frey and F Alauzet. Anisotropic mesh adaptation for CFD computations. *Computer Methods in Applied Mechanics and Engineering*, 194(48-49):5068–5082, 2005.

[29] M. Garcia. ASCE manual of practice 110, sedimentation engineering: processes, measurements, modeling, and practice, in examining the confluence of environmental and water concerns. *Proceedings of the World Environmental and Water Resource Congress.*, page 94, 2006.

[30] M. Garcia and G. Parker. Entrainment of bed sediment into suspension. *J. Hydraulic Eng.*, 117:414–435, 1991.

[31] R. A. Gingold and J. J. Monaghan. Smoothed Particle hydrodynamic: theory and application to non-spherical stars. *Monthly Notices of the Royal Astronomical Society*, 181:375–389, 1977.

[32] G. J. Gorman, C. C. Pain, M. D. Piggott, A. P. Umpleby, P. E. Farrell, and J. R. Maddison. Interleaved parallel tetrahedral mesh optimisation and load-balancing. In Ph. Bouillard and P. Diez, editors, *Adaptive Modeling and Simulation (ADMOS) 2009*, pages 101–104, 2009.

[33] W. Graf. *Fluvial Hydraulics: Flow and Transport Processes in Channels of Simple Geometry.* McGraw-Hill., 1998.

[34] J. P. Gray, J. J. Monaghan, and R. P. Swift. SPH elastic dynamics. *Computer Methods in Applied Mechanics and Engineering*, 190(49-50):6641–6662, 2001.

[35] C. Greenshields. *OpenFOAM - User's Guide.* OpenFOAM Foundation Ltd., 3.0.0 edition, 11 2015.

[36] P. M. Gresho and S. T. Chan. Solving the incompressible Navier-Stokes equations using consistent mass and a pressure Poisson equation. *ASME Symposium on recent development in CFD, Chicago 95.*, pages 51–73, 1988.

[37] P. M. Gresho and R. Sani. *Incompressible Flow and The Finite Element Method*, volume 2. 12 1998.

[38] F. H. Harlow and J. E. Welsh. Numerical calculation of time-dependent viscous incompressible flow with a free surface. *J. Physics of Fluids.*, 8:2182–2189, 1965.

[39] J. M. Hervouet and R. Ata. Telemac-3d user manual. Report, EDF-R&D, www.opentelemac.org, 2017. V7P2.

[40] M. Hirschler, P. Kunz, M. Huber, F. Hahn, and U. Nieken. Open boundary conditions for ISPH and their application to micro-flow. *Journal of Computational Physics*, 307:614–633, 2016.

[41] C. W. Hirt and B. D. Nichols. Volume of fluid (vof) method for

dynamics of free boundaries. *J. Comput. Phys.*, 39:201–221, 1981.

[42] R. Issa. Solution of the implicit discretized fluid flow equations by operator splitting. *Journal of Computational Physics*, 62:40–65, 01 1986.

[43] B. L. Jensen, B. M. Summer, H. R. Jensen, and J. Fredsøe. Flow around and forces on a pipeline near a scoured bed in steady current. *Offshore Mechanics and Arctic Engineering (OMAE).*, 112:206–213, 1990.

[44] H. K. Johnson and J. A. Zyserman. Controlling spatial oscillations in bed level update schemes. *J. Coastal Engineering.*, 46:109–126, 2002.

[45] P. Kunz, M. Hirschler, M. Huber, and U. Nieken. Inflow/outflow with Dirichlet boundary conditions for pressure in ISPH. *Journal of Computational Physics*, 326:171–187, December 2016.

[46] D. Kuzmin. A vertex-based hierarchical slope limiter for p-adaptive discontinuous Galerkin methods. *J. Comp. and App. Math.*, 233(12):3077–3085, 2010.

[47] D. Kuzmin and O. Mierka. On the implementation of the k - ϵ turbulence model in incompressible flow solvers based on a finite element discretization. *Int. J. of Computing Science and Mathematics.*, 1(2-4):193–206, 2007.

[48] B. E. Larsen, D. R. Fuhrman, and B. M. Sumer. Simulation of

wave-plus-current scour beneath submarine pipelines. *J. Waterw. Port Coast. Ocean Eng.*, 5:1–14, 2016.

[49] F. Li and L. Cheng. Numerical model for local scour under offshore pipelines. *Journal of Hydraulic Engineering*, 125(4):400–406, 1999.

[50] D. Liang, L. Cheng, and F. Li. Numerical modeling of flow and scour below a pipeline in currents Part I: Flow simulation. *J. Coastal Engineering.*, 52:25 – 42, 2005.

[51] D. Liang, L. Cheng, and F. Li. Numerical modeling of flow and scour below a pipeline in currents Part II: Scour simulation. *J. Coastal Engineering.*, 52:43–62, 2005.

[52] L. D. Libersky, A. G. Petschek, T. C. Carney, J. R. Hipp, and F. A. Allahdadi. High strain Lagrangian hydrodynamics: a three-dimensional SPH code for dynamic material response. *J. Comput. Phys.*, 109(1):67–75, November 1993.

[53] F. Liu. A Thorough Description if How Wall Functions are Implemented In OpenFOAM. Research report, Proceedings of CFD with OpenSource Software, 2016.

[54] G. R. Liu and M. B. Liu. *Smoothed particle hydrodynamics: a meshfree particle method.* World Scientific Publishing, 2003.

[55] X. Liu and M. H. Garcia. Three-dimensional numerical model with free water surface and mesh deformation for local sediment scour. *J. Waterway, Port, Coastal, Ocean Eng.*, 134:203–217, 2008.

[56] E. Y. M. Lo and S. Shao. Simulation of near-shore solitary wave mechanics by an incompressible SPH method. *Applied Ocean Research*, 24:275–286, 2002.

[57] L. Lobovský and P. H. L. Groenenboom. Remarks on FSI simulations using SPH. pages 378–383, May 2009.

[58] A. Loseille and F. Alauzet. Continuous Mesh Model and Well-Posed Continuous Interpolation Error Estimation. Research Report RR-6846, INRIA, 2009.

[59] A. Loseille and F. Alauzet. Optimal 3d highly anisotropic mesh adaptation based on the continuous mesh framework. In Brett W. Clark, editor, *Proceedings of the 18th International Meshing Roundtable*, pages 575–594, Berlin, Heidelberg, 2009. Springer Berlin Heidelberg.

[60] A. Loseille and F. Alauzet. Continuous mesh framework part i: Well-posed continuous interpolation error. *SIAM Journal on Numerical Analysis*, 49(1):38–60, 2011.

[61] L. B. Lucy. A Numerical Approach to Testing the Fission Hypothesis. *The Astronomical Journal*, 82(12):1013–1924, 1977.

[62] H. U. Mair. Review: Hydrocodes for structural response to underwater explosions. *Shock and Vibration*, 6(2):81–96, 1999.

[63] Y. Mao. *The interaction between a pipeline and an erodible bed.* PhD thesis, Technical University of Denmark, Lyngby, Denmark,

1986.

[64] B. W. Melville. The physics of local scour at bridge piers. *Fourth International Conference on Scour and Erosion. 5-7th, Nov., Tokyo Japan*, pages 28–38, 01 2008.

[65] B. W. Melville and S. E. Coleman. *Bridge Scour*. Water Resources Publication, 2000.

[66] B. W. Melville and A. J. Raudkivi. Flow characteristics in local scour at bridge piers. *Journal of Hydraulic Research*, 15(4):373–380, 1977.

[67] J. J. Monaghan. Smoothed Particle Hydrodynamics. *Annual review of Astronomy and Astrophysics*, 30:543–574, 1992.

[68] J. J. Monaghan. Simulating free surface flows with SPH. *Journal of Computational Physics*, 110:399–406, 1994.

[69] J. J. Monaghan. SPH without a tensile instability. *Journal of Computational Physics*, 159:290–311, 2000.

[70] J. J. Monaghan and J. B. Kajtar. SPH particle boundary forces for arbitrary boundaries. *Computer Physics Communications*, 180(10):1811–1820, 2009.

[71] J. J. Monaghan, A. Kos, and N. Issa. Fluid motion generated by impact. *Journal of waterway, port, coastal and ocean engineering*, 129:250–259, 2003.

[72] J. J Monaghan and C. J. Lattanzio. A refined method for astrophysical problems. *Astronomy and Astrophysics*, 149:135–143, 07 1985.

[73] A. Mourits. Delft3d-flow user manual. Report, Deltares, oss.deltares.nl, 2015.

[74] P. Nielsen. *Coastal Bottom Boundary Layers and Sediment Transport*. World Scientific, 1992.

[75] H. J. Niemann and N. Holscher. A review of recent experiments on the flow past circular cylinders. *Journal of Wind Engineering and Industrial Aerodynamics*, 33:197–209, 1990.

[76] S. L. Niemann, J. Fredsøe, and N. G. Jacobsen. Sand dunes in steady flow at low Froude numbers. *J. Hydraulic Eng.*, 137:5–14, 2011.

[77] J. M. Nunez Rattia, J. R Percival, S. J. Neethling, and M. D. Piggott. Modelling local scour near structures with combined mesh movement and mesh optimisation. *J. Comput. Phys.*, 375:1220 – 1237, 2018.

[78] J. M. Nunez Rattia, J. R Percival, B. Yeager, S. J. Neethling, and M. D. Piggott. Numerical simulation of scour below pipelines using flexible mesh methods. *Proceedings Eight International Conference on Scour and Erosion (ICSE2016).*, pages 101–108, 2016.

[79] C.C. Pain, A.P. Umpleby, C.R.E. de Oliveira, and A.J.H. Goddard.

Tetrahedral mesh optimisation and adaptivity for steady-state and transient finite element calculations. *Computer Methods in Applied Mechanics and Engineering*, 190(29):3771 – 3796, 2001.

[80] C. Paola and V. R. Voller. A generalized Exner equation for sediment mass balance. *J. Geophys. Res.*, 110(F04014), 2005.

[81] S. D. Parkinson, J. Hill, M. D. Piggott, and P. A. Allison. Direct numerical simulations of particle-laden density currents with adaptive, discontinuous finite elements. *J. Geosci. Model. Dev.*, 7:1945–1960, 2014.

[82] V. C. Patel, W. Rodi, and G. Scheuerer. Turbulence models for near-wall and low reynolds number flows: A review. *American Institute of Aeronautics and Astronautics*, 23:1308–1319, 1985.

[83] M. D. Piggott, P. E. Farrell, C. R. Wilson, G. J. Gorman, and C. C. Pain. Anisotropic mesh adaptivity for multi-scale ocean modelling. *Philosophical Transactions of the Royal Society of London A: Mathematical, Physical and Engineering Sciences*, 367(1907):4591–4611, 2009.

[84] M. D. Piggott, G. J. Gorman, C. C. Pain, P. A. Allison, A. S. Candy, B. T. Martin, and M. R. Wells. A new computational framework for multi-scale ocean modelling based on adapting unstructured meshes. *Int. J. for Numerical Methods in Fluids.*, 56:1003–1015, 2008.

[85] M. D. Piggott, C. C. Pain, G. J. Gorman, D. P. Marshall, and

P. D. Killworth. Unstructured adaptive meshes for ocean modeling. In H. Hasumi and M. W. Hecht, editors, *Ocean Modeling in an Eddying Regime*, pages 383–408. AGU, 2008.

[86] M. D. Piggott, C. C. Pain, G. J. Gorman, P. W. Power, and A. J. H. Goddard. *h*, *r*, and *hr* adaptivity with applications in numerical ocean modelling. *Ocean Model.*, 10:95–113, 2005.

[87] E. Reimnitz, C. A. Rodeick, and S. C. Wolf. Strudel scour: A unique arctic marine geological phenomenon. *J. Sedimentary Petrology.*, 44:409–420, 1974.

[88] J. F. Richardson and W. N. Zaki. Sedimentation and fluidisation Part 1. *Trans. Inst. Chem. Eng.*, 32:35–53, 1954.

[89] A. Roulund, B. M. Sumer, and J. Fredsøe. 3d mathematical modeling of scour around a circular pile in current. *Seventh International Symposium on River Sedimentation*, pages 131–138, 1999.

[90] A. Roulund, B. M. Sumer, J. Fredsøe, and J. Michelsen. Numerical and experimental investigation of flow and scour around a circular pile. *J. Fluid Mechanics.*, 534:351–401, 2005.

[91] Z. N. Shang Guan, Q. W. Ma, and D. F. Han. Comparisons of two repulsive models for boundary treatment in SPH. *Chuan Bo Li Xue/Journal of Ship Mechanics*, 18(1-2):37–44, 2014.

[92] R. Soulsby. *Dynamics of Marine Sands*. Thomas Telford, 1997.

[93] B. Stefanova and J. Grabe. Numerical modelling of the flow and

seabed erosion around a pipeline using smoothed particle hydrodynamics (sph). *Proceedings Seven International Conference on Scour and Erosion (ICSE2014)*, 7:725–732, 2014.

[94] O. D. L Strack and P. A Cundall. The distinct element method as a tool for research in granular media. Technical report, Department of Civil and Mineral Engineering, University of Minnesota, 1978.

[95] B. M. Sumer. Coastal and offshore scour/erosion issues – Recent advances. *Proceedings Fourth International Conference on Scour and Erosion (ICSE2008).*, K6:85–94, 2008.

[96] B. M. Sumer and J. Fredsøe. *The Mechanics of Scour in the Marine Environment.* World Scientific, 2002.

[97] P. K. Sweby. High-resolution schemes using flux limiters for hyperbolic conservation-laws. *SIAM J. on Numerical Analysis.*, 21:995–1011, 1984.

[98] T. Tang. Moving mesh methods for computational fluid dynamics. *Contemp. Math.*, 383:141–173, 01 2005.

[99] T. E. Tezduyar, M. Behr, and J Liou. A new strategy for finite element computations involving moving boundaries and interfaces the deforming-spatial-domain/space-time procedure: I. the concept and the preliminary numerical tests. *Computer Methods in Applied Mechanics and Engineering*, 94(3):339 – 351, 1992.

[100] C. Ulrich, N. Koliha, and T. Rung. Sph modelling of water/soil-

flows using a variable-resolution scheme. *Proceeding of the 6th SPHERIC SPH workshop, Hamburg, Germany*, pages 101–109, 2011.

[101] R. Vacondio, B. D. Rogers, P. K. Stansby, and P. Mignosa. SPH Modeling of Shallow Flow with Open Boundaries for Practical Flood Simulation. *Journal of Hydraulic Engineering*, 2011.

[102] L. C. van Rijn. Sediment transport, Part II: Suspended load transport. *J. Hydraulic Eng.*, 110:1613–1641, 1984.

[103] L. C. van Rijn, J. S. Ribberink, J. van Der Werf, and D. J. R. Walstra. Coastal sediment dynamics: recent advances and future research needs. *Journal of Hydraulic Research*, 51(5):475–493, 2013.

[104] Y. Vassilevski and K. Lipnikov. An adaptive algorithm for quasioptimal mesh generation. *Comp. Math. Math. Phys*, 39:1468–1486, 01 1999.

[105] H. K. Versteeg. *An introduction to Computational Fluid Dynamics - The Finite Volume Method*. Longman Group Ltd., 1995.

[106] D. Violeau. *Fluid Mechanics and the SPH Method*. Oxford University Press, 2012.

[107] D. Violeau and A. Leroy. On the maximum time step in weakly compressible SPH. *Journal of Computational Physics*, September 2013.

[108] D. Violeau and B. D. Rogers. Smoothed particle hydrodynamics

(SPH) for free-surface flows: Past, present and future. *Journal of Hydraulic Research*, 54(1):1–26, 2016.

[109] R. Whitehouse. *Scour at marine structures.* Thomas Telford Publishing, 1998.

[110] E. L. Wilson and R. E. Nickell. Application of the finite element method to heat conduction analysis. *Nuclear Engineering and Design*, 4(3):276 – 286, 1966.

[111] L. Zhao, B. Guo, X. Bai, W. Zhang, T. Li, and J. J. R. Williams. Finite element modelling of local scour below a pipeline under steady currents. *Int. J. Computational Fluid Dynamics.*, 30:1–6, 2016.

[112] Z. Zhao and H. J. S. Fernando. Numerical simulation of scour around pipelines using an eulereuler coupled two-phase model. *Environmental Fluid Mechanics*, 7(2):121–142, 2007.